

Tuning coupled electronic and nuclear dynamics in the nanoscale

DISSERTATION

zur Erlangung des akademischen Grades

Doctor rerum naturalium
(Dr. rer. nat.)

vorgelegt

der Fakultät Mathematik und Naturwissenschaften
der Technischen Universität Dresden

von

Alan Celestino

geboren am 24.05.1989 in Joinville

Eingereicht am 18. Juli 2017

Eingereicht am 18. Juli 2017

1. Gutachter: Prof. Dr. Jan-Michael Rost
2. Gutachter: Prof. Dr. Gianauelio Cuniberti

Contents

1	Introduction	1
2	Tuning molecular nonradiative lifetimes via intermolecular interaction	5
2.1	The Hamiltonian of the molecular dimer	7
2.2	The monomer and its decay dynamics	7
2.2.1	Model of the monomer	8
2.2.2	The single harmonic coordinate case	12
2.3	Interacting molecules	16
2.3.1	The model of the dimer	16
2.3.2	Single harmonic coordinate in the monomeric units	17
2.3.3	Consequences to the fluorescence quantum yield	23
2.4	Conclusions and outlook	24
3	Switching between electromechanical regimes in a nanoscale rotor	27
3.1	The dynamics of the mean-field and stochastic equations of motion . .	31
3.1.1	The dynamics of the mean-field equations revisited	31
3.1.2	Basins of attraction in the case of a symmetric rotor	37
3.1.3	A new dynamical regime	39
3.1.4	Stochastic equations of motion	40
3.1.5	Conclusions	43
3.2	A model of the nanoelectromechanical rotor based on the “orthodox” theory of single-electron tunneling	43
3.2.1	Orthodox theory of single-electron tunneling for a single island .	44
3.2.2	Mechanical equations	53
3.2.3	Deriving the stochastic equations of motion from Sec. 3.1.4 . . .	54
3.2.4	Deriving the mean-field equations of motion from Sec. 3.1.1 . . .	54
3.2.5	Conclusions	58
3.3	Experimental realization	59
3.3.1	Single-electron limit: stochastic equations of motion	60
3.3.2	Continuous-charging limit: mean-field equations of motion . . .	62
3.3.3	Dimensionless parameters from the stochastic and mean-field models	63
3.3.4	Discussion of some model approximations performed in Sec. 3.2	68
3.3.5	Conclusions	70
3.4	Nanoelectromechanical motor: rotational directionality	71
3.4.1	Equations of motion	72
3.4.2	Experimental realization	73
3.4.3	Rotational directionality in the continuous-charging limit	75
3.4.4	Rotational directionality in the single-electron limit	78
3.4.5	Concluding remarks	80

4	Summary and outlook	83
4.1	The molecular dimer	83
4.1.1	Summary	83
4.1.2	Outlook	84
4.2	The nanoelectromechanical rotor	85
4.2.1	Summary	86
4.2.2	Outlook	88
A	Damping due to light emission	91
B	Mean-field charge dynamics for the case with the gate electrode	93
C	Mean-field mechanical dynamics for the case with the gate electrode	97
	References	101

Chapter 1

Introduction

Nanotechnology can be defined as science, engineering, and technology conducted at the nanoscale. This constitutes a huge area of research overlapping with many other science fields, such as chemistry, biology, physics, material science, and engineering. It is in general concerned with objects having at least one dimension in the nanoscale regime, such as most of molecules, some molecular aggregates, buckyballs, carbon nanotubes, carbon nanosheets, metallic nanoparticles, and quantum dots. These objects often possess unique electronic and mechanical properties which allow for new functionalities. For instance, small metallic nanoparticles and quantum dots can exhibit the phenomenon of Coulomb blockade, where the tunnel current through an electrode is halted due to the charge on that electrode. This phenomenon led e.g. to the development of the single-electron transistor^{1,2}. Another example is given by multi-walled carbon nanotubes, whose mechanical properties are being used to devise a new generation of practically friction-, wear- and fatigue-free bearings³⁻⁵.

In many nanoscale systems, both man-made or existent in nature, electronic and nuclear degrees of freedom are strongly coupled. This coupling can lead to very complex dynamics, as in the case of nonradiative decay of an electronic excitation in molecules⁶⁻¹⁰ and chaos in nanoelectromechanical systems (NEMS)¹¹⁻¹⁴ * . It can also be fundamental to a certain functionality, e.g. in molecular motors and switches^{10,15-26}, to the isomerization of retinal in the processes leading to vision^{6,7,27,28}, and in some NEMS like the electron shuttle²⁹⁻³⁴ and charge-tunneling-driven nanorotors³⁵⁻³⁸.

Typically, the behavior of a system showing complex dynamics is nontrivially dependent on its parameters^{31,34,36,37}. Therefore, a certain functionality or phenomenon is existent in a specific region of the parameter space, and e.g. in a man-made device one would like to perform the nontrivial task of tuning the parameters into this region. In this thesis, we are interested in this kind of nanoscale complex systems, and how to tune into regions of their parameter space leading to desired dynamics (see Fig. 1.1 for examples regarded in this thesis).

We focus on the following two systems which are, in many aspects, “complementary”.

The molecular dimer

Molecules are some of the building blocks of nanotechnology, and we study the simplest assembly constructible out of these blocks: a molecular dimer consisting of identical molecules. This aggregate is a minimal example from supramolecular chemistry, and is

*In NEMS, a “mechanical” degree of freedom typically involves a “relevant” nuclear degree of freedom and many other degrees of freedom which are negligible in the dynamics of interest.

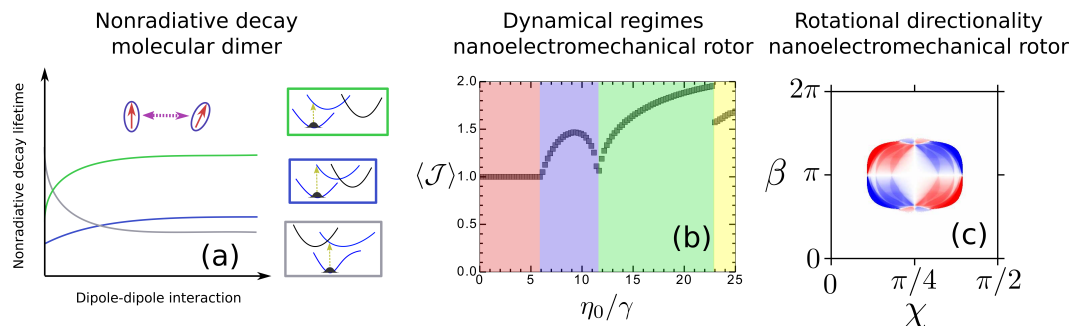


Figure 1.1: Dependence of various phenomena and functionalities upon the parameters from the systems studied in this thesis. (a) Schematic representation of the nonradiative decay (NRD) lifetime of an electronic excitation as a function of the intermolecular-interaction strength in a dimer. In the figure, the *monomeric* excited state potential energy surface (blue curve, insets) is coupled to a dark electronic state (black curve) in a well-localized crossing region, the NRD channel. Different curves stand for different positions of this channel in the nuclear space. (b) Time-averaged current across the system as a function of the driving strength* in the nanoelectromechanical rotor identifying its dynamical regimes. The standstill, oscillatory, rotatory, and chaotic-like regimes are shadowed respectively in red, blue, green, and yellow. (c) Directionality measure (color) as a function of the parameters β and χ^\dagger . Within the regions in red (blue) the preferred sense of rotation is clockwise (counterclockwise). Regions in white do not lead to a preferred sense of rotation.

commonly found in nature (e.g. in systems involved in photosynthesis^{39,40}). Molecular aggregates often show intrinsically quantum behavior, e.g. quantum beating^{41,42}.

The molecular dimer is considered in the context of nonradiative decay (NRD) dynamics of an electronic excitation. Electronic NRD is critical in a variety of molecular systems. In nature, it is essential e.g. in the isomerization of retinal (vision process)^{6,7,27,28}, nonphotochemical quenching in photosynthesis^{8,43,44}, and DNA photo-protection^{9,45–47}. NRD processes have also been exploited in technological applications, enabling e.g. transfer to long-lived triplet states which are useful in OLEDs⁴⁸, light-driven molecular rotary motors⁴⁹, and light-driven molecular switches^{10,25,26}.

We consider the Born-Oppenheimer approximation not to be valid already in the *monomer*: the electronic states are coupled through a well-localized region in the nuclear space, which we call the “NRD channel”. In this region, the electronic de-excitation occurs. The aggregated monomers interact via transition dipole-dipole interaction, which further couples electronic and nuclear degrees of freedom in the dimeric level. Due to this interaction, the dimer shows distorted and nontrivially coupled PESs conferring complex decay dynamics on it. We show how this interaction influences the NRD lifetime.

The influence of the intermolecular interaction upon the NRD lifetime depends strongly on the system parameters. In Fig. 1.1 (a) we illustrate this dependence upon the position of the NRD channel. Depending on the position of the NRD channel, the NRD lifetime can exhibit a completely different dependence on the intermolecular-interaction strength. In this context, it is important to mention that aggregates can be formed from various molecules, in a variety of environments (e.g. ultracold, suprafluid He-nanodroplets^{50–52}), and their geometry can be tuned by many different means

(e.g. by adding specific side groups⁵³). This great flexibility also implies a great variety of system parameters and ranges of tunability.

The nanoelectromechanical rotor

We also study a synthetic nanomachine: a nanorotor driven by charge tunneling. It favors assembly integrating (typically) larger, bulk-like systems such as nanoparticles and carbon nanotubes. These systems are often “more classical” than molecular dimers: for example, charge tunneling between nanosized electrodes is often described using rate equations^{1,2}, and wall rotation in a multi-walled carbon nanotube is often described via Langevin equations³.

The most intuitive application of the rotor we study in this thesis is yielding work, as a nanomotor. However, we will see that other applications like as a nanoscale switch and as a current rectifier are also achievable. These functionalities are fundamental to the development of nanomachinery and nanocircuits^{54,55}.

The rotor consists of electronic islands linked to a bearing via insulating arms. The islands can exchange electrons via tunneling with flanking electronic leads. An uniform electrostatic field brings about the coupling between electronic and mechanical degrees of freedom. This coupling also leads to varied dynamics, ranging from regular oscillations and rotations to chaotic-like intermittent dynamics mixing oscillations and rotations.

The type of steady-state dynamics depends on the parameters of the system. This dependence is exemplified in Fig. 1.1 (b) where four dynamical regimes can be identified by plotting the time-averaged current across the system as a function of the driving strength η , and (c) where geometries of the rotor (identified by the parameters β and χ [†]) for which it features a preferred sense of rotation are represented in red and blue. The system parameters depend on the type of components used to assemble it, and often they are highly tunable. For example, multi-walled carbon nanotubes can constitute rotational bearings in the nanoscale³⁻⁵. In this case, friction can be tuned by varying the temperature and interlayer spacing³. The electronic islands can be realized e.g. using gold nanoparticles, which can be site-selectively attached to carbon nanotubes using dip-pen nanolithography^{56,57}. The capacitance of the islands is dependent on the nanoparticle’s size, and this can be further engineered using gate electrodes^{1,2}. Also electrostatic fields can be spatially controlled in the nanoscale with the present-day technology⁵⁸.

Sectioning of this thesis

This thesis is organized as follows.

*The driving strength is defined as $\eta_0 = Q_{\text{var}} E \ell / I \Gamma^2$, where Q_{var} is the maximal charge variation on the islands, E is the magnitude of the electrostatic field, ℓ is the distance between the islands’ center of mass and the axis of rotation, I is the rotor’s moment of inertia, and Γ^{-1} gives the timescale of tunneling.

†To introduce a preferred direction of rotation (Sec. 3.4) in the rotor we need to tune the parameters β and χ appropriately. β is the angle between the arms of the rotor. To tune χ we make Q_{var} , E , ℓ , and Γ arm-dependent, thereby driving the arms independently. As a consequence, we have two driving strengths η_A and η_B , respectively for the arms bearing the islands A and B. χ is then defined by $\tan \chi = \eta_A / \eta_B$.

The Chap. 2 is about the influence of aggregation upon the NRD lifetime in a molecular dimer. In that chapter we introduce the models of the monomer and of the dimer. We discuss their NRD dynamics using an example where the *monomers* have harmonic PESs along a single nuclear coordinate. The other coordinates, together with external degrees of freedom, are regarded as a thermal bath using a multilevel Redfield equation. The decay dynamics of the monomer are trivial due to its harmonic PESs and simple NRD channel. This allows us to obtain an analytic expression for the NRD lifetime in the monomer, which serves as a reference for the dimer case. The dimer shows distorted and nontrivially coupled PESs conferring rather complex decay dynamics on it. The NRD lifetime in the dimer case is then determined numerically. We show that the intermolecular interaction can have a strong influence on the NRD lifetime. Depending on the position of the NRD channel, we find that the NRD lifetime can exhibit a completely different dependence on the intermolecular-interaction strength (as one can see in Fig. 1.1 (a)). The extension to larger aggregates and the implications to the quantum yield of molecular systems are also discussed. Our findings suggest design principles for molecular systems where a specific fluorescence quantum yield is desired.

The nanoelectromechanical rotor is considered in Chap. 3. In the literature one can identify two generic models of this type of rotor^{36–38}, which we refer to as “mean-field” and “stochastic” models in this thesis. In the mean-field model the system is described by a set of deterministic differential equations involving the average charge on the electronic islands, and therefore charge fluctuations are not taken into account. In the stochastic model the rotor is described by Fokker–Planck equations which fully take into account the charge fluctuations. We start by showing and comparing the dynamics of these models. The models show interesting phenomenology and predict useful functionality to the rotor. However, it is often unclear which assumptions are made upon the system when using these models. To clarify this matter we derive the models using the “orthodox” theory of single electron tunneling⁵⁹. Next, we propose experimental devices which can be described by these models. The parameter ranges accessible using these devices are estimated. The interaction between the charge on the islands and the image charge on the leads poses a hindrance to the experimental realization proposed in this thesis. Possible workarounds like replacing superconducting electrodes for the conducting leads are discussed. Turning our attention to motor functionality, we show that to introduce a preferred direction of rotation one needs to bend the rotor’s arms and make them uneven (see Fig. 1.1 (c)).

Finally, in Chap. 4 present our conclusions and suggest some new directions stemming from this work. We also briefly discuss how to recast the system as a current rectifier and show some preliminary results.

Chapter 2

Tuning molecular nonradiative lifetimes via intermolecular interaction

The lifetime of a molecular system's electronically excited state (EES) is determined by radiative and nonradiative transitions⁶⁰⁻⁶³. The radiative transitions stem from the coupling to the electromagnetic field, are characterized by light emission, and their typical timescale in individual molecules is several nanoseconds. This timescale can be changed upon aggregation. A particularly interesting example is given by molecular aggregates consisting of transition-dipole-dipole-interacting molecules, which have attracted interest for decades (see e.g. Refs.⁶⁴⁻⁶⁶ and references therein). These molecular aggregates can feature superradiant emission bringing radiative lifetimes down to e.g. the picosecond scale⁶⁷⁻⁶⁹. The origin of this phenomenon is the formation of exciton states coherently delocalized over several molecules.

Nonradiative electronic transitions, i.e. electronic transitions without the emission of light, can occur in different situations and involve totally different processes. The timescale of these transitions differs from case to case, but they can occur within pico- or even femtoseconds. Thus, nonradiative transitions can determine the EES lifetime in molecular systems. Often these fast nonradiative decay (NRD) processes are useful. For example, in nature they are involved in the switching between retinal isomers^{6,7,27,28}, a relevant step of the process leading to vision; nonphotochemical quenching in photosynthesis^{8,43,44}; and DNA photoprotection^{9,45-47}. NRD processes have also been exploited in technological applications, enabling e.g. transfer to long-lived triplet states which are useful in OLEDs⁴⁸, light-driven molecular rotary motors⁴⁹, and light-driven molecular switches^{10,25,26}. NRD processes can also be involved in singlet fission, a process featured by organic semiconductors whose mechanism remains uncertain^{70,71}. However, sometimes these NRD processes are unwanted, e.g. in light harvesting applications⁷² or where large quantum yields are desirable^{73,74}.

Of particular concern to this thesis are the NRD processes occurring in individual molecules, and how they are modified upon aggregation. In certain molecules, coupling between electronic and nuclear degrees of freedom are important, leading to a violation of the Born-Oppenheimer approximation, and thereby enabling nonradiative transitions between electronic states. This coupling in the single-molecule level can carry through upon aggregation, but it is not clear how the intermolecular interaction can change the nonradiative-transition dynamics. As represented in Fig. 2.1, in this chapter we show that molecular aggregation can strongly influence the timescale of NRD processes (NRD lifetime) in molecular systems. As in the case of the radiative lifetime, this influence arises from excitonic delocalization.

Since molecular aggregates can be formed from a variety of molecules, they can feature various *monomeric* potential energy surfaces (PESs). Moreover, the number of

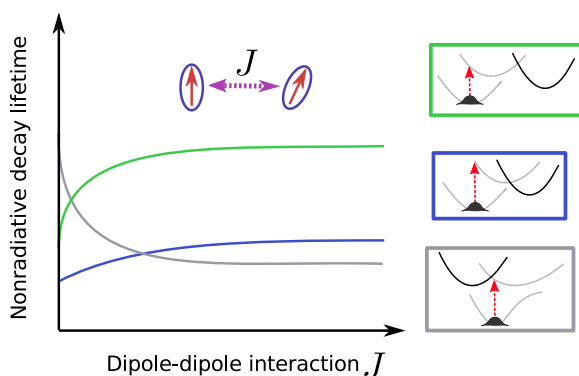


Figure 2.1: Schematic representation of the nonradiative lifetime of an electronic excitation as a function of the intermolecular-interaction strength in a dimer. The excitation is created by a Franck-Condon transition via e.g. a short laser pulse. In the figure, the *monomeric* excited state potential energy surface (upper gray curve, see insets) is coupled to a dark electronic state (black curve) in a well-localized crossing region, the nonradiative decay channel. This leads to nonradiative decay to the dark state potential energy surface. Notice that this channel occurs at the *monomer* level. Different curves stand for different positions of this channel in the nuclear space (see the insets).

molecules is practically arbitrary. For these reasons we concentrate on understanding the simplest case possible: a molecular homodimer* whose monomers possess harmonic PESs. In this way, our work additionally fits naturally in the literature as a follow-up to many of the previous studies^{75–80}. Moreover, molecular dimers are believed to be importantly involved in many processes of interest. For example, considering dimers and trimers is enough to explain the main features of the absorption spectrum of PTCDA molecules in He nanodroplets⁵¹. Molecular dimers are also believed to play an important role in photosynthesis. For instance, the B820 subunit of the purple bacterial core antenna LH1 is a dimer of bacteriochlorophyll (BChl)³⁹, and the structure of the light harvesting complex two (LHCII) of green plants suggests that several pairs of chlorophyll molecules (Chl-a and Chl-b) are close together⁴⁰.

We will see that the influence of aggregation upon the NRD lifetime depends strongly on the system parameters (e.g. transition dipole-dipole interaction, vibrational relaxation, location of the nonadiabatic coupling region, etc.). In this context, it is important to mention that aggregates can be formed in a variety of environments, and their geometry can be tuned by many different means. Traditionally, aggregates are created via self-assembly in aqueous solution⁶⁴, where their geometry can be tuned e.g. by adding specific side groups⁵³ or using DNA as a template⁸¹. In recent years, aggregates have also been created in ultracold, suprafluid He-nanodroplets^{50–52} and on surfaces, and the latter can be used as templates to obtain various molecular arrangements^{82–84}. This great flexibility in the choice of the molecule, environment, and molecular arrangement also implies a great variety of system parameters. Our approach will therefore be to extract underlying trends in the parameter space instead of focusing on a specific

*A dimer constituted by identical molecules.

situation (and the corresponding parameter set).

This chapter is organized as follows: in Sec. 2.2 we briefly describe the Hamiltonian of the dimer and introduce the model of its monomeric unit. We also show exemplary calculations on the monomeric NRD dynamics, focusing on the dependence on the position of the NRD channel. These calculations will serve as a reference in Sec. 2.3, where we discuss the dimer. In Sec. 2.3 we introduce the model of the dimer in detail and show calculations on its NRD dynamics. It will turn out that the intermolecular interaction can have a strong influence on the NRD lifetime. This influence will be shown to depend on the position of the NRD channel in the monomeric unit. The extension to larger aggregates and the implications to the quantum yield of molecular systems will be discussed. Finally, we wrap this chapter up in Sec. 2.4, where we also point out some possible new research directions stemming from this work. The work presented in this chapter was submitted for publication. The respective manuscript can be found in Ref. [85].

2.1 The Hamiltonian of the molecular dimer

In this chapter we study the decay of an electronic excitation in a molecular homodimer. The monomeric units interact via their transition dipoles, and the geometry is fixed: both the distance and the relative orientation of the transition dipoles of the monomers are held fixed. In the following, we leave aside the electronic spin. Moreover, we consider that the molecules do not bind covalently, and that they keep their chemical structure. If this is fulfilled, the Hamiltonian of the dimer can be written as

$$H_{\text{dim}} = H_{\text{mon1}}(\vec{Q}_1, \vec{Q}_1^e) + H_{\text{mon2}}(\vec{Q}_2, \vec{Q}_2^e) + H_{\text{dip}}(\vec{Q}_1, \vec{Q}_2, \vec{Q}_1^e, \vec{Q}_2^e), \quad (2.1)$$

where H_{mon1} and H_{mon2} are the Hamiltonians of the monomers (unaltered by the intermolecular interaction), and they depend respectively on (\vec{Q}_1, \vec{Q}_1^e) and on (\vec{Q}_2, \vec{Q}_2^e) , where $\vec{Q}_{1(2)}$ are the nuclear and $\vec{Q}_{1(2)}^e$ the electronic coordinates of monomer 1 (2). The transition dipole-dipole interaction is noted by H_{dip} . The Hamiltonian H_{dim} contains the kinetic energy of, and the pair Coulomb interaction between all electrons and nuclei composing the monomeric units. The general form of these terms can be easily found in textbooks (see e.g. pages 11 and 12 of⁶³). In a real situation, the dimer also interacts with external degrees of freedom, e.g. from a solvent. We account for these degrees of freedom using a standard quantum open system approach which will be described in Sec. 2.2.2.1.

2.2 The monomer and its decay dynamics

In this section we will introduce the model of the monomer and define the electronic de-excitation process we are considering. We will also make a series of assumptions, notably (i) that just two electronic states are relevant for the de-excitation processes studied here and (ii) that the Born-Oppenheimer approximation is violated in a very limited region of the nuclear space. Then, we focus on an example where the de-excitation process occurs along a single harmonic nuclear coordinate, which we call “reaction

coordinate”. For example, a single nuclear coordinate is used in Ref. [10] to describe the nonradiative electronic decay in indanylidene-pyrroline, in the context of molecular switches. The remaining coordinates, together with external degrees of freedom, will be considered to effectively damp the dynamics along the reaction coordinate. This example will serve as a reference for the dimer in Sec. 2.3.

2.2.1 Model of the monomer

Because the ratio of the electronic mass to the nuclear mass in a molecule is $m_{\text{el}}/M < 10^{-3}$, electrons are expected to move much faster than nuclei on average⁶³. This typically means that the electronic and nuclear dynamics can be treated separately in “some” sense. The Born-Oppenheimer approximation assumes the extreme case where different electronic states are completely uncoupled; we will make the weaker assumption that different electronic states couple only in a limited region of the nuclear space. In both cases, it is useful to start with the Born-Oppenheimer separation of electronic and nuclear motion. In this separation we do not perform any further assumption: we just write the molecular Hamiltonian and wavefunction in a basis suited to the approximations which will come later on.

2.2.1.1 Born-Oppenheimer separation in the diabatic basis

We start by writing the Hamiltonian of the monomer in the form

$$H_{\text{mon}}(\vec{Q}, \vec{Q}^e) = H_e(\vec{Q}^e; \vec{Q}) + K_n + V_{n-n}(\vec{Q}), \quad (2.2)$$

where K_n is the kinetic energy of the nuclei and V_{n-n} is the potential energy stemming from interactions between the nuclei. The electronic Hamiltonian $H_e(\vec{Q}^e; \vec{Q})$ depends parametrically on the nuclear coordinates \vec{Q} , and it is given by

$$H_e(\vec{Q}^e; \vec{Q}) = K_e + V_{e-e}(\vec{Q}^e) + V_{e-n}(\vec{Q}^e; \vec{Q}), \quad (2.3)$$

where K_e is the kinetic energy of the electrons and V_{e-e} is the potential energy coming from interaction between the electrons. The (parametric) dependence on the nuclear coordinates comes about through the potential energy V_{e-n} , which is the sum of all possible pair Coulomb interactions involving an electron and a nucleus.

The solutions of the time-independent Schrödinger equation describing the state of the electrons in the electrostatic field of the stationary nuclei, $\phi_a(\vec{Q}^e; \vec{Q})$, fulfil

$$H_e(\vec{Q}^e; \vec{Q}) \phi_a(\vec{Q}^e; \vec{Q}) = E_a(\vec{Q}) \phi_a(\vec{Q}^e; \vec{Q}), \quad (2.4)$$

where E_a is the eigenenergy of the electronic state a . Note the parametric dependence of the solutions and of the eigenenergies on \vec{Q} . These solutions form the so-called “adiabatic basis” of the molecular wavefunction (see e.g.⁶³ pp. 13-15). Because of the parametric dependence on the nuclear coordinates, this basis is not very practical if one is interested in performing numerical simulations. Therefore, we use a “diabatic basis” (also known as “crude adiabatic basis”⁶³)

$$\{\phi_b(\vec{Q}^e; \vec{Q} = \vec{Q}_0^b)\}, \quad (2.5)$$

where \vec{Q}_0^b is an equilibrium nuclear configuration at the electronic state b , to write the molecular wavefunction ψ , i.e.

$$\psi(\vec{Q}^e, \vec{Q}) = \sum_b X_b(\vec{Q}) \phi_b(\vec{Q}^e; \vec{Q}_0^b). \quad (2.6)$$

Note that the elements of this diabatic basis are eigenfunctions of $H_e(\vec{Q}^e; \vec{Q})$ just at $\vec{Q} = \vec{Q}_0^b$. It will be useful in the following to have the definition

$$\Delta V_b(\vec{Q}^e; \vec{Q}) = H_e(\vec{Q}^e; \vec{Q}) - H_e(\vec{Q}^e; \vec{Q}_0^b). \quad (2.7)$$

We want to write the Hamiltonian of the monomer H_{mon} in the basis (2.5). To do that, we write the time-independent Schrödinger equation of the monomer

$$H_{\text{mon}}(\vec{Q}, \vec{Q}^e) \psi(\vec{Q}^e, \vec{Q}) = \mathcal{E} \psi(\vec{Q}^e, \vec{Q}) \quad (2.8)$$

using the expression of the molecular wavefunction from Eq. (2.6) (\mathcal{E} is the correspondent eigenenergy) and the definition of H_{mon} from Eq. (2.2)

$$\left[H_e(\vec{Q}^e; \vec{Q}) + K_n + V_{n-n}(\vec{Q}) \right] \sum_b X_b(\vec{Q}) \phi_b(\vec{Q}^e; \vec{Q}_0^b) = \mathcal{E} \sum_b X_b(\vec{Q}) \phi_b(\vec{Q}^e; \vec{Q}_0^b). \quad (2.9)$$

Inserting the definition from Eq. (2.7) into Eq. (2.9) yields

$$\begin{aligned} & \sum_b \left[H_e(\vec{Q}^e; \vec{Q}_0^b) + \Delta V_b(\vec{Q}^e; \vec{Q}) + K_n + V_{n-n}(\vec{Q}) \right] X_b(\vec{Q}) \phi_b(\vec{Q}^e; \vec{Q}_0^b) = \\ & \mathcal{E} \sum_b X_b(\vec{Q}) \phi_b(\vec{Q}^e; \vec{Q}_0^b). \end{aligned} \quad (2.10)$$

Now we multiply Eq. (2.10) by $\phi_{b'}^*(\vec{Q}^e; \vec{Q}_0^{b'})$ from the left and integrate over all electronic coordinates, obtaining

$$\begin{aligned} & \int d\vec{Q}^e \phi_{b'}^*(\vec{Q}^e; \vec{Q}_0^{b'}) H_{\text{mon}}(\vec{Q}, \vec{Q}^e) \psi(\vec{Q}^e, \vec{Q}) = \\ & \left[V_{b'}(\vec{Q}) + K_n \right] X_{b'}(\vec{Q}) + \sum_{b|b \neq b'} O_{b',b}(\vec{Q}) X_b(\vec{Q}) \end{aligned} \quad (2.11)$$

where the PES of the electronic state b' is given by

$$V_{b'}(\vec{Q}) = E_b(\vec{Q}_0^{b'}) + V_{n-n}(\vec{Q}) + O_{b',b'}(\vec{Q}) - \mathcal{E}, \quad (2.12)$$

and the coupling between the states b and b' is given by

$$O_{b',b}(\vec{Q}) = \int d\vec{Q}^e \phi_{b'}^*(\vec{Q}^e; \vec{Q}_0^{b'}) \Delta V_b(\vec{Q}^e; \vec{Q}) \phi_b(\vec{Q}^e; \vec{Q}_0^b). \quad (2.13)$$

Defining

$$\phi_b(\vec{Q}^e; \vec{Q}_0^b) = \langle \vec{Q}^e | b \rangle, \quad (2.14)$$

where $\{ |\vec{Q}^e\rangle \}$ is the basis of the electronic coordinates, we can write the Hamiltonian of the monomer as

$$H_{\text{mon}} = \sum_b \left[V_b(\vec{Q}) + K_n \right] |b\rangle \langle b| + \sum_{b,b'|b \neq b'} O_{b',b}(\vec{Q}) |b'\rangle \langle b|. \quad (2.15)$$

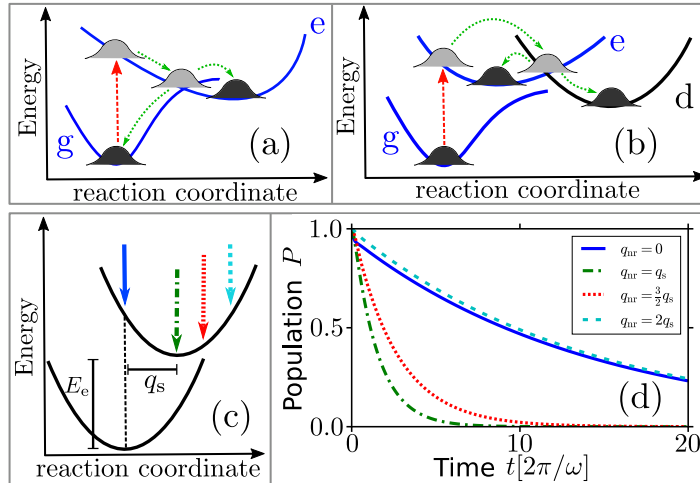


Figure 2.2: Potential energy surfaces (PESs) and nonradiative decay (NRD) dynamics of a single molecule. The top row shows sketches of the electronic excitation and relaxation processes along the PESs. After a vertical Franck-Condon transition, the electronic relaxation can occur in two different ways: (a) direct relaxation from the electronically excited state e to the electronic ground state g; (b) relaxation from the optically bright state e to the electronic dark state d. The black wave packets stand for the nuclear wavefunction after vibrational relaxation. (c) Ground and first optically excited state harmonic PESs (case considered in the numerics). q_s is the shift between PESs. (d) Time-resolved population decay for different positions of the NRD channel. The q_{nr} values are illustrated as arrows in (c) according to the colors and linestyles of the curves in (d).

2.2.1.2 Electronic states and excitation process

The basic features of a monomer are sketched in Fig. 2.2 (a) and (b), where the relevant PESs are shown as a function of a single nuclear “reaction” coordinate q . Initially the molecule is in its electronic ground state $|g\rangle$, in thermal equilibrium with respect to the ground state PES. After a vertical Franck-Condon transition (e.g. through a short laser pulse) to an EES $|e\rangle$, which leaves the nuclear wavefunction unchanged⁶², the nuclear dynamics and the NRD set in. Vibrational relaxation due to coupling to environmental degrees of freedom accompanies the coherent motion on the PESs (we describe how we model vibrational relaxation in Sec. 2.2.2.1).

As depicted respectively in Fig. 2.2 (a) and (b), we consider two different situations: (a) the NRD is to the ground state and (b) the NRD is to a dark state $|d\rangle$. In the situation (a), the Hamiltonian of the monomer is given by

$$H_{\text{mon}} = \sum_{b=g,e} [V_b(\vec{Q}) + K_n] |b\rangle \langle b| + \sum_{b,b'=g,e | b \neq b'} O_{b',b}(\vec{Q}) |b'\rangle \langle b|, \quad (2.16)$$

and in (b)

$$H_{\text{mon}} = \sum_{b=g,e,d} [V_b(\vec{Q}) + K_n] |b\rangle \langle b| + \sum_{b,b'=g,e,d | b \neq b'} O_{b',b}(\vec{Q}) |b'\rangle \langle b|, \quad (2.17)$$

where in the last case just $O_{e,d}$, $O_{d,e}$, and the diagonal elements of the coupling operator from Eq. (2.13) do not vanish. The terms $O_{g,e/e,g}$ ($O_{g,d/d,g}$) vanish because the PESs

g and e (g and d) are well separated in energy in the region accessible to the nuclear dynamics.

2.2.1.3 NRD channel

Typically, nonradiative transitions between molecular electronic states involve nuclear degrees of freedom and occur at points where the respective PESs are close or cross^{60,86}. In our model, these nonradiative transitions stem from the couplings defined by Eq. (2.13) (note the dependence on the nuclear degrees of freedom). We assume that these couplings are just non-vanishing in a localized region in nuclear space. In this region, which we call “the NRD channel”, the electronic excitation can efficiently leave the electronic state $|e\rangle$ (to either $|g\rangle$ or $|d\rangle$). Since we do not focus on a particular molecule and we are mainly interested in qualitative results, we model the NRD channel as an imaginary potential added to the excited PES. This PES is then given by

$$\tilde{V}_e(\vec{Q}) = V_e(\vec{Q}) - i\Gamma(\vec{Q}), \quad (2.18)$$

where we denote $\Gamma(\vec{Q})$ as the “decay-function”. This way of modeling the NRD implies irreversibility of the de-excitation process, it that once the excitation leaves $|e\rangle$ it cannot return.

We emphasize that this NRD channel can occur in any region of the PES, and that the corresponding decay can occur to the ground state and to dark states. For instance, in β -Apo-8'-carotenal a NRD channel to a dark state is believed to occur at the vertical Franck-Condon region⁸⁷. In Ref. [88], a nearly barrierless decay pathway from the Franck-Condon region of cytosine to the ground state is described.

The imaginary potential $-i\Gamma(\vec{Q})$ implies that H_{mon} is now non-Hermitian. Therefore, the norm of the state evolving with H_{mon} decays in time with a rate which depends on the nuclear dynamics. Since in the beginning all the population is in $|e\rangle$, we interpret the norm as the population in that state. Due to this modeling of the de-excitation process, we do not need to include the state where the electronic excitation decays to ($|g\rangle$ or $|d\rangle$) in H_{mon} . In the dimer case (which we will consider later on), the transition dipole-dipole interaction can promote excitation from $|g\rangle$ back to $|e\rangle$ and therefore one needs to keep $|g\rangle$ in H_{dim} . Since our final objective is to model the dimer, we also keep $|g\rangle$ in the Hamiltonian of the monomer:

$$H_{\text{mon}} = \sum_{b=g,e} [\tilde{V}_b(\vec{Q}) + K_n] |b\rangle \langle b|, \quad (2.19)$$

where

$$\tilde{V}_g(\vec{Q}) = V_g(\vec{Q}). \quad (2.20)$$

2.2.2 The single harmonic coordinate case

As a concrete example, we consider harmonic PESs, i.e.

$$V_g(\vec{Q}) = \sum_n \frac{(\omega_n^g)^2 (Q_n - \tilde{Q}_n^g)^2}{2M_n}, \quad (2.21)$$

$$V_e(\vec{Q}) = \sum_n \frac{(\omega_n^e)^2 (Q_n - \tilde{Q}_n^e)^2}{2M_n}, \quad (2.22)$$

where Q_n and M_n are respectively the position (element of the vector \vec{Q}) and the mass of the nucleus n , and $\tilde{Q}_n^{g(e)}$ and $\omega_n^{g(e)}$ are respectively the minimum's position and the frequency of $V_{g(e)}$ along Q_n . We define a set of normal mode coordinates $\{q_k\}$ through the transformation

$$Q_n - \tilde{Q}_n^g = \sum_k M_n^{-1/2} Z_{n,k} q_k \quad (2.23)$$

(note that the normal mode coordinates are mass-weighted), where the transformation coefficients $Z_{n,k}$ are real. With this set we can rewrite the PESs as

$$V_g(\vec{Q}) = \sum_k (\tilde{\omega}_k^g)^2 q_k^2, \quad (2.24)$$

$$V_e(\vec{Q}) = \sum_k (\tilde{\omega}_k^e)^2 (q_k - q_k^s)^2, \quad (2.25)$$

where we have used the new frequencies $\tilde{\omega}_k^{g(e)}$ and minimum's position coordinates q_k^s .

Furthermore, we consider that the decay dynamics occur along a single normal mode coordinate, which we call "reaction coordinate" and denote by q . All other coordinates q_k , together with external degrees of freedom (e.g. from a solvent), are regarded as forming a bath that brings about vibrational relaxation. Our formal treatment of the degrees of freedom forming this bath is exposed in Sec. 2.2.2.1.

The PESs $V_g(q)$ and $V_e(q)$ are now functions of a single coordinate q . We assume them to have identical frequencies ω , but to be shifted with respect to each other in position by q_s and in energy by E_e (see Fig. 2.2 (c)). More precisely, they are given by

$$V_g(q) = \frac{1}{2} \omega^2 q^2, \quad (2.26)$$

$$V_e(q) = E_e + \frac{1}{2} \omega^2 (q - q_s)^2. \quad (2.27)$$

Here, E_e is the electronic transition energy.

For simplicity, we take the decay-function to be a delta function $\Gamma(q) = \lambda \delta(q - q_{nr})$ centered at the position q_{nr} , where λ is the NRD strength. The results in this thesis do not change qualitatively for a different well-localized decay-function (e.g. a Gaussian function). The resulting non-Hermitian Hamiltonian of the monomer is

$$H_{\text{mon}}(p, q) = H_g(p, q) |g\rangle \langle g| + (H_e(p, q) - i\Gamma(p, q)) |e\rangle \langle e|, \quad (2.28)$$

where p is the kinetic energy operator (the commutator $[q, p] = i\hbar$). Introducing the bosonic creation operator for the ground and excited state potential energy surfaces,

respectively $a_g^\dagger = \sqrt{\omega/2\hbar}(q - ip/\omega)$ and $a_e = a_g - q_s\sqrt{\omega/2\hbar}$ ⁸⁹, the nuclear Hamiltonians H_g and H_e are

$$H_g(a_g, a_g^\dagger) = \hbar\omega a_g^\dagger a_g, \quad (2.29)$$

$$H_e(a_e, a_e^\dagger) = E_e + \hbar\omega a_e^\dagger a_e. \quad (2.30)$$

We write here H_{mon} in the second quantization because it will be useful in Sec. 2.2.2.1, where we describe how we model the vibrational relaxation in the monomer.

2.2.2.1 Vibrational relaxation in the monomer

The monomer we consider here is a molecule interacting with an environment. This environment, which can be e.g. a solvent or neighboring molecules, possesses degrees of freedom coupled to those of the monomer. Using the framework of open quantum systems, we write the total Hamiltonian, including not just the degrees of freedom of the molecule but also of the environment, as

$$H_{\text{tot}}^{(m)} = H_{\text{sys}}^{(m)} + H_{\text{bath}}^{(m)} + H_{\text{int}}^{(m)}, \quad (2.31)$$

i.e. a sum of the “system” part $H_{\text{sys}}^{(m)}$, the “bath” $H_{\text{bath}}^{(m)}$, and the interaction between system and bath $H_{\text{int}}^{(m)}$. The superscript (m) stands for “monomer” and was introduced to differentiate these symbols from their “dimer” counterparts, which will appear in Sec. 2.3.2.1.

We include only the reaction coordinate q in the system degrees of freedom. All the other normal mode coordinates q_k , together with the environmental degrees of freedom, are considered to compose the bath. The (non-Hermitian) system Hamiltonian is given by

$$H_{\text{sys}}^{(m)}(p, q) = H_{\text{mon}}(p, q). \quad (2.32)$$

This model, in which a limited number of intra-molecular harmonic modes are implicitly incorporated in the system part, is often used in the literature (see e.g.^{89–92}) and was found to be reasonable in many cases (see e.g.^{51,93}).

The bath is a set of harmonic normal modes with frequencies ω_λ and creation (annihilation) operators b_λ^\dagger (b_λ). This leads to the bath Hamiltonian

$$H_{\text{bath}}^{(m)}(\{b_\lambda\}) = \sum_\lambda \hbar\omega_\lambda b_\lambda^\dagger b_\lambda. \quad (2.33)$$

We consider that the bath is linearly coupled to the system degrees of freedom^{63,90,94}. As for the system coupling operator (to the bath) we use a model *analogous* to the one described in Ref. [89],

$$L_{\text{sys}}^{(m)} = (a_g^\dagger + a_g) |g\rangle \langle g| + (a_e^\dagger + a_e) |e\rangle \langle e|. \quad (2.34)$$

Note that we couple the system to the bath through the dimensionless reaction coordinate $\sqrt{2\omega/\hbar}q = (a_g^\dagger + a_g)$ in the electronic ground state and to the shifted dimensionless reaction coordinate $\sqrt{2\omega/\hbar}(q - q_s) = (a_e^\dagger + a_e)$ in the electronically excited state. Later on, when we consider a quantum master equation for the system part, this system

coupling operator will lead to vibrational relaxation towards the ground state of (i) $V_g(q)$ in $|g\rangle$ and (ii) $V_e(q)$ in $|e\rangle$. Our bath coupling operator is the sum of all bath normal mode coordinates⁶³. The system-bath interaction Hamiltonian is given by

$$H_{\text{int}}^{(m)} = \left(a_g + a_g^\dagger - \sqrt{\frac{2\omega}{\hbar}} q_s |e\rangle \langle e| \right) \sum_{\lambda} \kappa_{\lambda} (b_{\lambda} + b_{\lambda}^\dagger). \quad (2.35)$$

The weight of the bath coupling to a specific frequency $\tilde{\omega}$ is encoded in the bath spectral density $j(\tilde{\omega}) = \sum_{\lambda} \kappa_{\lambda}^2 \delta(\tilde{\omega} - \omega_{\lambda})$. We have chosen an Ohmic spectral density

$$j(\tilde{\omega}) = \frac{\hbar^2}{\pi} \Theta(\tilde{\omega}) \gamma \tilde{\omega} e^{-\tilde{\omega}/\omega_0}, \quad (2.36)$$

where γ and ω_0 are real parameters, and the step function $\Theta(\tilde{\omega})$ guarantees that we just consider positive frequencies.

Now we aim at obtaining an approximate equation of motion for the ‘‘system’’ alone, which includes only the degrees of freedom of $H_{\text{sys}}^{(m)}$. Our procedure follows Ref. [63]. We start from the equation of motion for the density operator of the complete system, formed by the system and bath degrees of freedom,

$$\frac{\partial \rho_{\text{tot}}^{(m)}(t)}{\partial t} = -\frac{i}{\hbar} \left[H_{\text{tot}}^{(m)} \rho_{\text{tot}}^{(m)}(t) - \rho_{\text{tot}}^{(m)}(t) \left(H_{\text{tot}}^{(m)} \right)^\dagger \right]. \quad (2.37)$$

Next, we trace out the bath degrees of freedom, i.e. those which are included in $H_{\text{bath}}^{(m)}$. This yields the reduced density operator (system density operator)

$$\rho_{\text{sys}}^{(m)} = \text{Tr}_{\text{bath}} \left\{ \rho_{\text{tot}}^{(m)} \right\} = \sum_{\lambda} \sum_{n_{\lambda}} \langle n_{\lambda} | \rho_{\text{tot}}^{(m)} | n_{\lambda} \rangle, \quad (2.38)$$

in which we used the bath eigenbasis $\{|n_{\lambda}\rangle\}$ to represent the trace over bath degrees of freedom. Then we perform the Born and Markov approximations, obtaining a multilevel Redfield equation of motion in the energy representation. For simplicity, we perform the secular approximation and neglect pure dephasing⁶³, obtaining the following equation of motion:

$$\frac{\partial \rho_{\text{sys}}^{(m)}}{\partial t} = -\frac{i}{\hbar} \left[H_{\text{sys}}^{(m)} \rho_{\text{sys}}^{(m)} - \rho_{\text{sys}}^{(m)} \left(H_{\text{sys}}^{(m)} \right)^\dagger \right] + \mathcal{L} \left[\rho_{\text{sys}}^{(m)} \right]. \quad (2.39)$$

\mathcal{L} is a dissipator, which can be written in the following Lindblad form

$$\mathcal{L} \left[\rho_{\text{sys}}^{(m)} \right] = \sum_{a,b} \left[A_{a,b} \rho_{\text{sys}}^{(m)} A_{a,b}^\dagger - \frac{1}{2} \left(A_{a,b}^\dagger A_{a,b} \rho_{\text{sys}}^{(m)} + \rho_{\text{sys}}^{(m)} A_{a,b}^\dagger A_{a,b} \right) \right], \quad (2.40)$$

where we have introduced the eigenbasis $\{|a\rangle\}$ of the Hermitian part of $H_{\text{sys}}^{(m)}$,

$$\frac{1}{2} \left[H_{\text{sys}}^{(m)} + \left(H_{\text{sys}}^{(m)} \right)^\dagger \right] |a\rangle = \epsilon_a^{(m)} |a\rangle, \quad (2.41)$$

with the correspondent eigenspectrum $\{\epsilon_a^{(m)}\}$, and the double sum in Eq. (2.40) runs over all eigenstates. The Lindblad operators $A_{a,b}$ are given by $A_{a,b} = \sqrt{k_{a \rightarrow b}} |b\rangle \langle a|$, with the transition rates

$$k_{a \rightarrow b} = C(\omega_{ab}) \left| \langle a | L_{\text{sys}}^{(m)} | b \rangle \right|^2, \quad (2.42)$$

where $\omega_{ab} = (\epsilon_a^{(m)} - \epsilon_b^{(m)})/\hbar$ and

$$C(\omega_{ab}) = \frac{2\pi}{\hbar^2} (1 + n(\omega_{ab})) (j(\omega_{ab}) - j(-\omega_{ab})), \quad (2.43)$$

where

$$n(\omega_{ab}) = \frac{1}{e^{\hbar\omega_{ab}/k_B T} - 1} \quad (2.44)$$

is the Bose-Einstein distribution. We set $T = 0$, and therefore $n(\omega_{ab}) = 0$ for $\omega_{ab} > 0$. Using the relation $1 + n(\omega_{ab}) = -n(-\omega_{ab})$ and Eq. (2.36) one can rewrite $C(\omega_{ab})$ as

$$C(\omega_{ab}) = \frac{2\pi}{\hbar^2} \gamma \omega_{ab} e^{-\omega_{ab}/\omega_0}, \quad \omega_{ab} > 0, \quad (2.45)$$

$$C(\omega_{ab}) = 0, \quad \omega_{ab} < 0. \quad (2.46)$$

Note that setting pure dephasing to zero implies $C(0) = 0$ ⁶³.

2.2.2.2 The decay dynamics of the monomer

We simulate the decay dynamics of the monomer solving the multilevel Redfield equation defined by Eq. (2.39). All numerical results shown here are obtained for the parameter values $q_s = 1.5\sqrt{\hbar/\omega}$, $\gamma = 1$, $\omega_0 = 10\omega/\pi$, NRD strength $\lambda = 0.1\hbar^{3/2}\omega^{1/2}$, and temperature $T = 0$ (because we are not interested in thermal effects). These values of γ , ω_0 , and λ guarantee fast vibrational relaxation compared to the timescales of the NRD and nuclear oscillations. This case applies to many molecules, as vibrational relaxation typically takes place within a picosecond⁶².

As a reference for the dimer case later on, we now consider the dependence of the NRD on q_{nr} for a single molecule. We focus on different locations q_{nr} of the NRD channel leading to qualitatively different behaviors. These locations are $q_{nr} = 0$ (at the vertical Franck-Condon region), $q_{nr} = q_s$ (minimum of the excited-state PES of the monomer), and $q_{nr} = 2q_s$ (classical turning point to the right of this minimum). Note that $q_{nr} = 0$ and $q_{nr} = 2q_s$ enclose the classically accessible region in the nuclear space.

The numerically calculated population in the monomer EES $P(t)$ is shown in Fig. 2.2 (d). Different NRD channel positions q_{nr} are indicated by arrows in Fig. 2.2 (c) according to the colors and linestyles in Fig. 2.2 (d). $P(t)$ depends sensitively on q_{nr} , and decays approximately as a monoexponential $P(t) \approx \exp(-t/\tau_{nr}^{(mon)})$ because vibrational relaxation is fast compared to NRD dynamics.

We estimate the monomeric NRD lifetime assuming that the nuclear wavefunction is in the ground state of $V_e(q)$ at all times ($|\psi_{\text{ground}}\rangle$), but with a time-dependent norm $P_{\text{est}}(t)$:

$$|\psi(t)\rangle = \sqrt{P_{\text{est}}(t)} |\psi_{\text{ground}}\rangle. \quad (2.47)$$

The Schrödinger equation for this state (using H_{mon}) is

$$\frac{d}{dt} \sqrt{P_{\text{est}}(t)} |\psi_{\text{ground}}\rangle = -\frac{i}{\hbar} H_{\text{mon}} \sqrt{P_{\text{est}}(t)} |\psi_{\text{ground}}\rangle, \quad (2.48)$$

and we can use it to obtain an equation for the time evolution of the norm,

$$\frac{d}{dt} P_{\text{est}}(t) = \frac{d}{dt} (\langle \psi(t) | \psi(t) \rangle) = -\frac{2\lambda}{\hbar} P_{\text{est}}(t) \langle \psi_{\text{ground}} | \delta(q - q_{nr}) | e \rangle \langle e | \psi_{\text{ground}} \rangle. \quad (2.49)$$

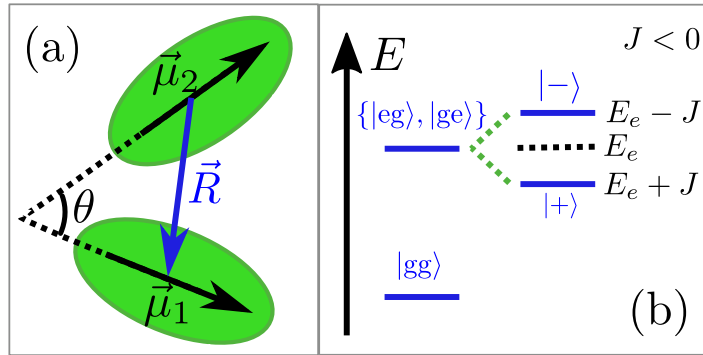


Figure 2.3: Sketch of the geometry (a) and energy levels (b) (vibronic levels suppressed) of the dimer. (a) The dimer’s geometry is defined by the relative orientation of the transition dipoles $\vec{\mu}_1$ and $\vec{\mu}_2$ (θ), and the relative position \vec{R} . (b) The eigenenergies of the ground state $|gg\rangle$, single excitation manifold $\{|eg\rangle, |ge\rangle\}$ for vanishing J (E_e), and dimer singly excited states $|+\rangle$ and $|-\rangle$ (respectively $E_e + J$ and $E_e - J$) for $J < 0$.

Substituting the vibrational ground state of $V_e(q)$ times $|e\rangle$ for $|\psi_{\text{ground}}\rangle$ in Eq. (2.49) yields

$$\frac{d}{dt}P_{\text{est}}(t) = -\frac{1}{\tau_{\text{est}}^{(\text{mon})}(q_{\text{nr}})}P_{\text{est}}(t), \quad (2.50)$$

where

$$\tau_{\text{est}}^{(\text{mon})}(q_{\text{nr}}) = \tau_{\text{est}}^{(\text{mon})}(q_s) \exp\left[\frac{\omega(q_{\text{nr}} - q_s)^2}{\hbar}\right], \quad (2.51)$$

$$\tau_{\text{est}}^{(\text{mon})}(q_s) = \frac{\sqrt{\pi}\hbar^{3/2}}{2\lambda\omega^{1/2}}. \quad (2.52)$$

We find that $\tau_{\text{nr}}^{(\text{mon})}(q_{\text{nr}}) \approx \tau_{\text{est}}^{(\text{mon})}(q_{\text{nr}})$ in the numerical results from Fig. 2.2 (d). Notice in particular that the closer the NRD channel is to the minimum of the excited-state PES, the faster the NRD takes place.

2.3 Interacting molecules

To furnish a clear example on how the transition dipole-dipole interaction influences the NRD lifetime, we treat in this thesis the case of a molecular dimer^{51,75–78,80} in detail (see Fig. 2.3).

2.3.1 The model of the dimer

The two monomers are assumed to be sufficiently far apart to neglect overlap between electronic wavefunctions. However, they interact via long-range Coulomb interaction. The Coulomb interaction depends on the dimer’s geometry, which is considered fixed (see Fig. 2.3 (a)). In the point-dipole approximation, which is often appropriate, the interaction strength can be written as

$$J \propto \frac{1}{R^3} \left(\vec{\mu}_1 \cdot \vec{\mu}_2 - 3 \frac{(\vec{R} \cdot \vec{\mu}_1)(\vec{R} \cdot \vec{\mu}_2)}{R^2} \right). \quad (2.53)$$

Here, \vec{R} is the distance vector between the centers of the two monomers and we consider $\vec{\mu}_1$ and $\vec{\mu}_2$ to be the transition dipoles of monomer 1 and 2, respectively. We stress that the specific form of this interaction is not relevant in the following.

The electronic subspace is spanned by the states $|gg\rangle = |g\rangle \otimes |g\rangle$, $|eg\rangle = |e\rangle \otimes |g\rangle$, $|ge\rangle = |g\rangle \otimes |e\rangle$, and $|ee\rangle = |e\rangle \otimes |e\rangle$ (see Fig. 2.3 (b)). For both monomers in the electronic ground state, the corresponding nuclear Hamiltonian is $H_{\text{gg}}(\vec{Q}_1, \vec{Q}_2) = H_{\text{g}}(\vec{Q}_1) + H_{\text{g}}(\vec{Q}_2)$, where $H_{\text{g}}(\vec{Q}_j) = K_j + V_{\text{g}}(\vec{Q}_j)$, and K_j is the nuclear kinetic energy for the monomer j . Consequently, the initial state (before the Franck-Condon vertical transition) is the same as the thermal equilibrium of two uncoupled monomers. Because of large detuning in energy, the doubly excited state $|ee\rangle$ is not populated and we will not discuss it further.

In the single excitation manifold, i.e. in the subspace spanned by the degenerate electronic states $|eg\rangle$ and $|ge\rangle$, the transition dipole-dipole interaction leads to a coupling of the form $H_{\text{dip}} = J(|eg\rangle\langle ge| + |ge\rangle\langle eg|)$. The dimer Hamiltonian from Eq. (2.1), in the single excitation manifold, is then given by

$$\begin{aligned} H_{\text{ex}}(\vec{Q}_1, \vec{Q}_2) = & K_{\text{nuc}} + \left(\tilde{V}_{\text{e}}(\vec{Q}_1) + V_{\text{g}}(\vec{Q}_2) \right) |eg\rangle\langle eg| \\ & + \left(\tilde{V}_{\text{e}}(\vec{Q}_2) + V_{\text{g}}(\vec{Q}_1) \right) |ge\rangle\langle ge| \\ & + J(|eg\rangle\langle ge| + |ge\rangle\langle eg|), \end{aligned} \quad (2.54)$$

where $K_{\text{nuc}} = K_1 + K_2$, and we note that H_{ex} is non-Hermitian due to the complex absorbing potential $-i\Gamma(\vec{Q}_{1(2)})$ contained in $\tilde{V}_{\text{e}}(\vec{Q}_{1(2)})$. This absorbing potential makes the dimer state's norm decay in time. Since after the Franck-Condon transition the dimer is in the single excitation manifold, we interpret this norm as the population within that manifold. Moreover, for the decay process we are considering, the dynamics within $|gg\rangle$ is not relevant.

2.3.2 Single harmonic coordinate in the monomeric units

As a concrete example, we consider the monomeric units to have the same PESs and NRD channels as the single molecule considered in Sec. 2.2.2. A single harmonic coordinate (the reaction coordinate) is considered per monomer, which we denote $q_{1(2)}$ for monomer 1 (2). This model directly relates to previous studies of dimers, where NRD has not been taken into account (see e.g. Refs. ^{51,75-78,80}). The resulting Hamiltonian is given by

$$\begin{aligned} H_{\text{ex}}(q_1, q_2) = & K_{\text{nuc}} + \left(\tilde{V}_{\text{e}}(q_1) + V_{\text{g}}(q_2) \right) |eg\rangle\langle eg| \\ & + \left(\tilde{V}_{\text{e}}(q_2) + V_{\text{g}}(q_1) \right) |ge\rangle\langle ge| \\ & + J(|eg\rangle\langle ge| + |ge\rangle\langle eg|), \end{aligned} \quad (2.55)$$

where

$$V_{\text{g}}(q_i) = \frac{1}{2}\omega^2 q_i^2, \quad (2.56)$$

$$\tilde{V}_{\text{e}}(q_i) = E_{\text{e}} + \frac{1}{2}\omega^2 (q_i - q_{\text{s}})^2 - i\lambda\delta (q_i - q_{\text{nr}}), \quad (2.57)$$

where $i = 1, 2$ indicate the monomer.

The way we treat the other nuclear coordinates of each monomeric unit, and the external degrees of freedom, is analogous to the model exposed in Sec. 2.2.2.1, and will be explained in detail in the following.

2.3.2.1 Vibration relaxation in the dimer

In Sec. 2.2.2.1 we have described the open quantum system approach used to take into account the other nuclear coordinates (apart from the reaction coordinate) and the environmental degrees of freedom in the monomer case. In the dimer case, we assume the same model for its monomeric units: same separation of “system” and “bath” degrees of freedom; same “system” and “bath” Hamiltonians; and the same interaction between the “system” and the “bath”. We further assume that the monomers and their respective environments are formed by disjoint sets of degrees of freedom. The bath spectral densities are the same for the both baths (see Sec. 2.2.2.1). The resulting total Hamiltonian is given by

$$H_{\text{tot}}^{(d)} = H_{\text{tot}}^{(m1)} + H_{\text{tot}}^{(m2)} + J (|\pi_1\rangle \langle \pi_2| + |\pi_2\rangle \langle \pi_1|), \quad (2.58)$$

where we have used the notation $|\pi_1\rangle = |e\rangle \otimes |g\rangle$ and $|\pi_2\rangle = |g\rangle \otimes |e\rangle$, and “m1” refers to “monomer 1” while “m2” refers to “monomer 2”. Note that the electronic states $|g\rangle$ and $|e\rangle$ do not couple to the single excitation manifold $\{|\pi_1\rangle, |\pi_2\rangle\}$ and therefore we no longer take these electronic states into account.

Using the framework of open quantum systems, we can separate the total Hamiltonian $H_{\text{tot}}^{(d)}$ into a system part $H_{\text{sys}}^{(d)}$, a bath part $H_{\text{bath}}^{(d)}$ and a system-bath interaction $H_{\text{int}}^{(d)}$. The system Hamiltonian is

$$H_{\text{sys}}^{(d)} = H_{\text{sys}}^{(m1)} + H_{\text{sys}}^{(m2)} + J (|\pi_1\rangle \langle \pi_2| + |\pi_2\rangle \langle \pi_1|) = H_{\text{ex}}, \quad (2.59)$$

where H_{ex} is given by Eq. (2.55). The dimer bath Hamiltonian is given by $H_{\text{bath}}^{(d)} = H_{\text{bath}}^{(m1)} + H_{\text{bath}}^{(m2)}$ while the dimer system-bath interaction is given by $H_{\text{int}}^{(d)} = H_{\text{int}}^{(m1)} + H_{\text{int}}^{(m2)}$ (all given in Sec. 2.2.2.1).

As in Sec. 2.2.2.1, we aim at obtaining an approximate equation of motion for the dimer’s system part alone, which includes only the degrees of freedom of H_{ex} . We follow the same procedure as described in Sec. 2.2.2.1, obtaining the following multilevel Redfield equation for the dimer’s system density operator $\rho_{\text{sys}}^{(d)}$:

$$\frac{\partial \rho_{\text{sys}}^{(d)}}{\partial t} = -\frac{i}{\hbar} \left[H_{\text{sys}}^{(d)} \rho_{\text{sys}}^{(d)} - \rho_{\text{sys}}^{(d)} \left(H_{\text{sys}}^{(d)} \right)^\dagger \right] + \mathcal{L}_1 \left[\rho_{\text{sys}}^{(d)} \right] + \mathcal{L}_2 \left[\rho_{\text{sys}}^{(d)} \right], \quad (2.60)$$

with

$$\mathcal{L}_j \left[\rho_{\text{sys}}^{(d)} \right] = \sum_{\alpha, \beta} \left\{ A_{\alpha, \beta}^{(mj)} \rho_{\text{sys}}^{(d)} \left(A_{\alpha, \beta}^{(mj)} \right)^\dagger - \frac{1}{2} \left[\left(A_{\alpha, \beta}^{(mj)} \right)^\dagger A_{\alpha, \beta}^{(mj)} \rho_{\text{sys}}^{(d)} + \rho_{\text{sys}}^{(d)} \left(A_{\alpha, \beta}^{(mj)} \right)^\dagger A_{\alpha, \beta}^{(mj)} \right] \right\}. \quad (2.61)$$

In Eq. (2.61) we have introduced the eigenbasis $\{|\alpha\rangle\}$ of the Hermitian part of $H_{\text{sys}}^{(d)}$,

$$\frac{1}{2} \left[H_{\text{sys}}^{(d)} + \left(H_{\text{sys}}^{(d)} \right)^\dagger \right] |\alpha\rangle = \epsilon_\alpha^{(d)} |\alpha\rangle, \quad (2.62)$$

with the correspondent eigenspectrum $\{\epsilon_\alpha^{(d)}\}$, and the double sum in Eq. (2.61) runs over all eigenstates. The Lindblad operator $A_{\alpha,\beta}^{(mj)} = \sqrt{k_{\alpha\rightarrow\beta}^{(mj)}} |\beta\rangle \langle\alpha|$ and the transition rates are given by

$$k_{\alpha\rightarrow\beta}^{(mj)} = C(\omega_{\alpha\beta}) \left| \langle\alpha| L_{\text{sys}}^{(mj)} |\beta\rangle \right|^2, \quad (2.63)$$

where $\omega_{\alpha\beta} = (\epsilon_\alpha^{(d)} - \epsilon_\beta^{(d)})/\hbar$ and $C(\omega_{\alpha\beta})$ was already defined in Eqs. (2.43), (2.45), and (2.46), where one needs to replace ω_{ab} by $\omega_{\alpha\beta}$.

2.3.2.2 The decay dynamics of the dimer

In order to simulate the electronic decay dynamics we solve Eq. (2.60) numerically. As our initial state, we consider the result of a Franck-Condon transition to the first excited adiabatic electronic state. For $J < 0$, the case we show here, this corresponds to $|+\rangle = (|eg\rangle + |ge\rangle)/\sqrt{2}$ (for $J > 0$ it corresponds to $|-\rangle = (|eg\rangle - |ge\rangle)/\sqrt{2}$). These two electronic states are the eigenstates of the system if nuclear degrees of freedom are neglected (see Fig. 2.3 (b)). The results we discuss here are not fundamentally changed by choosing a different initial condition within the single excitation manifold, nor by considering $J > 0$.

We use the same values of q_s , γ , ω_0 , λ , and T , as in the monomer case discussed in Sec. 2.2.2.2. To get a feeling for the values of the transition dipole-dipole interaction strength used below, let us take the vibrational relaxation to occur within some hundreds of femtoseconds in our model. Then, the largest value of the interaction strength that we consider in the following, $J = -10$, corresponds to roughly -1000 cm^{-1} , which is in the order of magnitude achievable in experiments.

The numerical results for the dimer are shown in Fig. 2.4. From the top to the bottom row, $q_{\text{nr}} = 0$, $q_{\text{nr}} = q_s$, and $q_{\text{nr}} = 2q_s$ are shown, respectively. In the left column, the population in the single excitation manifold $P(t)$ is shown for different values of J . As in the monomer case, $P(t)$ approximately follows a monoexponential decay (see Fig. 2.4 (a)-(c)) and can therefore be written as $P(t) \approx \exp(-t/\tau_{\text{nr}}^{(\text{dim})})$. The numerically fitted NRD lifetime $\tau_{\text{nr}}^{(\text{dim})}$ is plotted as a function of J as continuous blue lines in the right column (Fig. 2.4 (d)-(f)). As one can see from Fig. 2.4 (d)-(f), $P(t)$ depends on J , and this dependence is different for different values of q_{nr} . For all q_{nr} , the NRD lifetime $\tau_{\text{nr}}^{(\text{dim})}$ varies monotonically with J and it saturates for small J ($J < 0$) at the value $\tau_{\text{nr}}^{(\text{sat})}$, which depends on the specific choice of q_{nr} , q_s and λ . This saturation value can be analytically determined to be

$$\tau_{\text{nr}}^{(\text{sat})}(q_{\text{nr}}) \approx \tau_{\text{nr}}^{(\text{sat})}(q_s/2) \exp \left[\frac{\omega (q_{\text{nr}} - q_s/2)^2}{\hbar} \right], \quad (2.64)$$

$$\tau_{\text{nr}}^{(\text{sat})}(q_s/2) \approx \frac{\pi^{1/2} \hbar^{3/2}}{2} \lambda \omega^{1/2}, \quad (2.65)$$

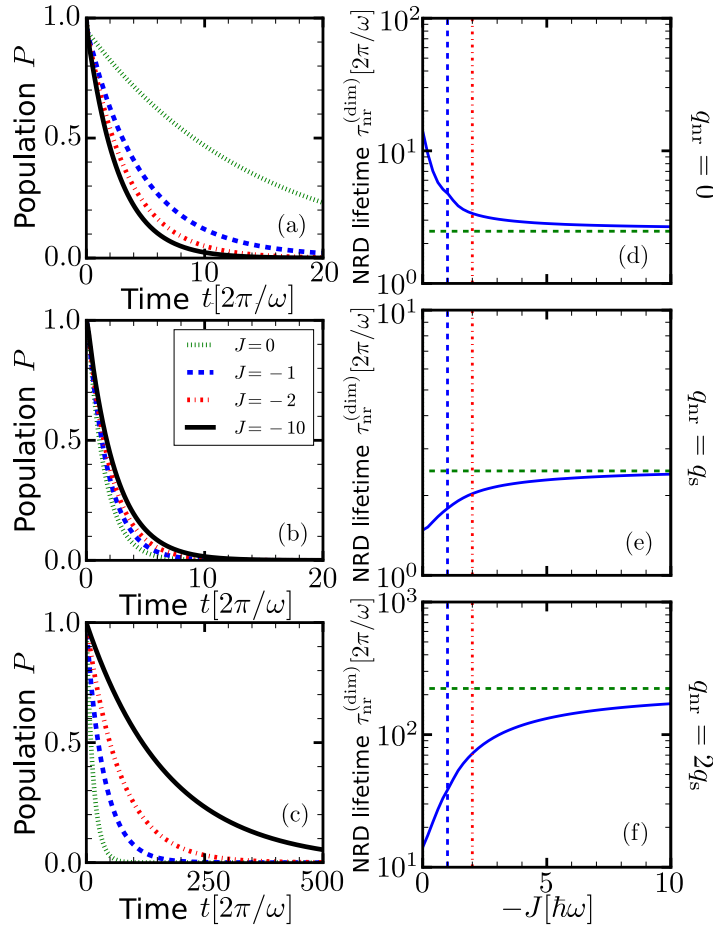


Figure 2.4: Nonradiative decay dynamics for different J and q_{nr} values. (a), (b), and (c): Population in the single excitation manifold $P(t)$ as a function of time (notice the different x-axis range in (c)). (d), (e), and (f): NRD lifetime $\tau_{\text{nr}}^{(\text{dim})}(J)$ as a function of J (continuous blue line). The green dashed horizontal line is the NRD lifetime saturation value $\tau_{\text{nr}}^{(\text{sat})}$. For clarity, the values $J = -1$ and $J = -2$ for which we plotted $P(t)$ in (a), (b), and (c) are indicated by vertical lines matching the colors and linestyles in (a), (b), and (c).

(see discussion about the adiabatic limit in Sec. 2.3.2.3) and is plotted as a dashed green line in Fig. 2.4 (d)-(f). The value of q_{nr} determines whether $\tau_{\text{nr}}^{(\text{dim})}$ increases or decreases with J . For $q_{\text{nr}} > 3q_s/4$ ($q_{\text{nr}} < 3q_s/4$), $\tau_{\text{nr}}^{(\text{dim})}$ increases (decreases) with $|J|$.

The transition dipole-dipole interaction can suppress (trigger) fluorescence of (non-)fluorescent molecules when they form dimers or larger aggregates. Although in the examples shown in Fig. 2.4 (d)-(f) the NRD lifetime maximally varied over approximately one order of magnitude (Fig. 2.4 (f)), this is not limited on the range of NRD lifetime variation. The range of variation of $\tau_{\text{nr}}^{(\text{dim})}$ with J is at least the ratio

$$\frac{\tau_{\text{nr}}^{(\text{mon})}}{\tau_{\text{nr}}^{(\text{sat})}} \approx \frac{\tau_{\text{est}}^{(\text{mon})}(q_{\text{nr}})}{\tau_{\text{nr}}^{(\text{sat})}} \approx \exp\left[\frac{\omega(3q_s^2/4 - q_{\text{nr}}q_s)}{\hbar}\right], \quad (2.66)$$

where $\tau_{\text{est}}^{(\text{mon})}(q_{\text{nr}})$ is the NRD lifetime of the monomer estimated in Sec. 2.2.2.2. Since it depends exponentially on the shift between the monomer PESs q_s , the range of tunability becomes exponentially larger for larger q_s .

2.3.2.3 The adiabatic limit

We stress that the full quantum nonadiabatic dynamics is considered in our numerical simulations, i.e. the correct dimer PESs, nonadiabatic couplings and excitonic relaxation is naturally included in the numerics. The analytic expression of $\tau_{\text{nr}}^{(\text{sat})}$ we used in the discussion of our numerical results was derived in the adiabatic limit. In this limit, namely when

$$|J| \gg \frac{\hbar^{1/2} \omega^{3/2} q_s}{\sqrt{2}}, \quad (2.67)$$

we can consider the nuclear dynamics to be confined within the adiabatic PES associated with the electronic state $|+\rangle$ ($|-\rangle$) for $J < 0$ ($J > 0$). The corresponding (complex) PESs are given by

$$\tilde{V}_{\pm}(\vec{Q}_1, \vec{Q}_2) = \sum_{j=1}^2 \frac{1}{2} \left(\tilde{V}_e(\vec{Q}_j) + V_g(\vec{Q}_j) \right) \pm J, \quad (2.68)$$

and non-adiabatic couplings between these PESs are negligible. Notice from Eq. (2.68) that the coordinates \vec{Q}_1 and \vec{Q}_2 are not coupled. Thus, for each coordinate the NRD channel (which appears via $\tilde{V}_e(\vec{Q}_j)$) is the same as for the uncoupled monomers. However, the potential on which the nuclear wavepacket moves has a different shape (and in particular a different minimum) from the monomer's excited-state PES.

Considering the PESs from our numerics, we obtain for $V_{\pm}(q_1, q_2)$ (the Hermitian part of $\tilde{V}_{\pm}(q_1, q_2)$) a well known result^{79,80,95}:

$$V_{\pm}(q_1, q_2) = \pm J + \sum_j \frac{\omega^2 (q_j - q_s/2)^2}{2} + \frac{\omega^2 q_s^2}{4}. \quad (2.69)$$

The adiabatic PESs are thus shifted by $q_s/2$ in each coordinate with respect to the ground-state PES of the monomer. Using these PESs we can obtain the analytic formula for the saturated NRD lifetime $\tau_{\text{nr}}^{(\text{sat})}$ (given by Eqs. (2.64) and (2.65)). We consider fast vibrational relaxation compared to the NRD and nuclear oscillations timescale. As a consequence, most of the NRD occurs after the nuclear wavefunction has already relaxed to the ground state of $V_+(q_1, q_2)$. Assuming that the wavefunction is *always* at the ground state, we obtain the saturated NRD lifetime $\tau_{\text{nr}}^{(\text{sat})}$. Comparing the analytic formulas for $\tau_{\text{nr}}^{(\text{sat})}$ with $\tau_{\text{est}}^{(\text{mon})}(q_{\text{nr}})$, one observes that their formulas only differ by the shift in the nuclear coordinate, q_s for the monomer and $q_s/2$ for the saturated dimer. This is because the minimum of $V_+(q_1, q_2)$ is at $(q_1 = q_s/2, q_2 = q_s/2)$, while the minimum from the excited-state PES of the monomer j lies at $q_j = q_s$.

2.3.2.4 Extension to longer aggregates

An extension of the NRD lifetime analysis to longer aggregates can also be performed^{96,97}. The adiabatic PESs of an N -mer (when the electronic wavefunction is delocalized over N monomers) can be estimated in the adiabatic limit using perturbation theory. Let us consider a molecular ring. The Hamiltonian of the aggregate within the single excitation manifold is given by

$$H_{\text{agg}} = H_{\text{nuc}} + \hat{J}, \quad (2.70)$$

where \hat{J} is the transition dipole-dipole interaction

$$\hat{J} = \sum_{n=1}^N J (|\pi_n\rangle \langle \pi_{n+1}| + |\pi_{n+1}\rangle \langle \pi_n|) \quad (2.71)$$

(we consider $n \bmod N$ in the definition of \hat{J}^*), and we have used the notation $|\pi_n\rangle$ to indicate that the monomer n is electronically excited while the others are in the electronic ground state. H_{nuc} is given by

$$H_{\text{nuc}} = \sum_{n=1}^N H_n |\pi_n\rangle \langle \pi_n|, \quad (2.72)$$

$$H_n = K_n + \tilde{V}_e^{(n)}(\vec{Q}_n) + \sum_{m \neq n}^N (K_m + V_g^{(m)}(\vec{Q}_m)), \quad (2.73)$$

where K_n is the kinetic energy of monomer n ; $V_g^{(n)}(\vec{Q}_n)$ and $\tilde{V}_e^{(n)}(\vec{Q}_n)$ are respectively the ground and excited state PESs of monomer n , whose nuclear coordinates are denoted by \vec{Q}_n . We stress that the excited state PES $\tilde{V}_e^{(n)}(\vec{Q}_n)$ contains a NRD channel $-i\Gamma(\vec{Q}_n)$ and is, therefore, a complex potential. In the adiabatic approximation, the kinetic energy can be neglected:

$$H_n = \tilde{V}_e^{(n)}(\vec{Q}_n) + \sum_{m \neq n}^N (V_g^{(m)}(\vec{Q}_m)). \quad (2.74)$$

Now we fix a certain nuclear configuration $\{\vec{Q}_n\} = \{\vec{Q}_n^0\}$ and use perturbation theory regarding the Hamiltonian of the aggregate. We consider \hat{J} as the “unperturbed Hamiltonian” and H_{nuc} (after adiabatic approximation) as the “perturbation”. The eigenstates of \hat{J} are (⁶³ pp. 64-66)

$$|\varphi_k\rangle = \sum_{n=1}^N c_k(n) |\pi_n\rangle, \quad (2.75)$$

where k starts from 0 and

$$c_k(n) = \frac{1}{\sqrt{N}} \exp\left(\frac{2\pi i k}{N} n\right). \quad (2.76)$$

The corresponding eigenvalues are

$$\epsilon_k = 2J \cos\left(\frac{2\pi k}{N}\right). \quad (2.77)$$

The state of lowest eigenenergy in the case $J < 0$ is the non-degenerate $k = 0$, whose eigenenergy is $\epsilon_0 = 2J^\dagger$. Transformation of H_{nuc} in the eigenbasis of \hat{J} yields

$$\sum_k |\varphi_k\rangle \langle \varphi_k| H_{\text{nuc}} \sum_{k'} |\varphi_{k'}\rangle \langle \varphi_{k'}| = \sum_n H_n \left(\sum_{k,k'} c_k^*(n) c_{k'}(n) |\varphi_k\rangle \langle \varphi_{k'}| \right). \quad (2.78)$$

*This is necessary because we are considering a molecular ring.

†Notice that the lowest ϵ_k is not the same as in the dimer because the dimer is not an instance of a molecular ring: while in the ring each molecule has 2 neighbors, in the dimer it has just one neighbor.

We are interested in the PES $\tilde{V}_{k=0}(\{\vec{Q}_m\})$ of the (non-degenerate) state of lowest energy. Therefore, we can use the first order correction to the eigenenergy $\epsilon_0 = 2J$

$$\begin{aligned}\tilde{V}_{k=0}(\{\vec{Q}_m\}) &= \epsilon_0 + \langle \varphi_0 | H_{\text{nuc}} | \varphi_0 \rangle = 2J + \frac{1}{N} \sum_n H_n, \\ \tilde{V}_{k=0}(\{\vec{Q}_m\}) &= 2J + \sum_n \left(\frac{1}{N} \tilde{V}_e(\vec{Q}_n) + \frac{N-1}{N} V_g(\vec{Q}_n) \right).\end{aligned}\quad (2.79)$$

For identical monomers of a single harmonic nuclear coordinate q_n , the adiabatic PESs are harmonic and shifted in all reaction coordinates by q_s/N (they are also shifted in energy):

$$\tilde{V}_{k=0}(\{q_n\}) = 2J + \omega^2 \sum_n \left[\frac{(q_n - q_s/N)^2}{2} + \frac{q_s^2}{2N} \left(1 - \frac{1}{N} \right) \right]. \quad (2.80)$$

Using the same procedure as in Sec. 2.3.2.3, the saturated N -meric NRD lifetime can be calculated. The ratio between monomeric and saturated N -meric NRD lifetimes behave as

$$\frac{\tau_{\text{nr}}^{(\text{mon})}}{\tau_{\text{nr}}^{(\text{sat},N)}} \approx \frac{\tau_{\text{est}}^{(\text{mon})}(q_{\text{nr}})}{\tau_{\text{nr}}^{(\text{sat},N)}} \sim \exp \left[- \frac{\omega q_s (q_{\text{nr}}(2N-2)/N - q_s(N^2-1)/N^2)}{\hbar} \right]. \quad (2.81)$$

2.3.3 Consequences to the fluorescence quantum yield

Let us finally discuss the consequences of our results for the fluorescence quantum yield Y_{fl} of an aggregate, which we express as

$$Y_{\text{fl}} = \frac{\tau_{\text{nr}}}{\tau_{\text{fl}} + \tau_{\text{nr}}}, \quad (2.82)$$

where τ_{fl} and τ_{nr} are the fluorescence and the nonradiative lifetime of the aggregate, respectively. As discussed above, the nonradiative lifetime can change strongly upon aggregation, compared to the monomeric value. Also the fluorescence lifetime τ_{fl} changes upon aggregation⁹⁸. There are two important cases: (i) J-aggregates: here bright states located at the bottom of the exciton band provide the dominant contribution to the fluorescence lifetime. These states possess an oscillator strength that can be considerably enhanced compared to that of a monomer. This enhancement depends essentially on the number of monomers over which the aggregate wavefunction is coherently delocalized and on the geometrical arrangement of the monomers^{69,83,99,100}. In the extreme case the fluorescence lifetime can become N times shorter than that of the monomer, $\tau_{\text{fl}} = \tau_{\text{fl}}^{(\text{mon})}/N$, where N is the number of monomers. This means that for constant τ_{nr} the quantum yield increases. The mechanism described in Chap. 2 can either increase Y_{fl} further (as exemplified in Fig. 2.4 (e) and (f)) or it can reduce the Y_{fl} (as exemplified in Fig. 2.4 (d)). As we have shown, our mechanism can change τ_{nr} by several orders of magnitude and therefore considerably alter the the fluorescence quantum yield.

(ii) H-aggregates. Here the bright states are located at the top of the exciton band. At typical temperatures only dark states at the bottom of the band are occupied. Here, no emission occurs, and one does not expect that the change in the nonradiative lifetime will strongly alter this result.

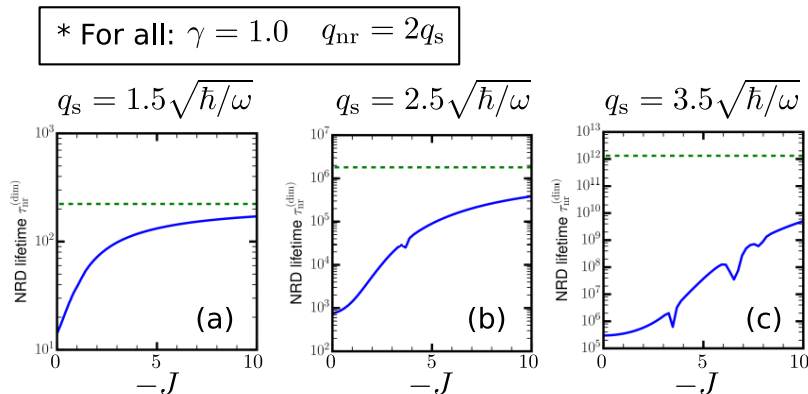


Figure 2.5: NRD lifetime $\tau_{\text{nr}}^{(\text{dim})}(J)$ as a function of J (continuous blue line) for different values of q_{s} . The green dashed horizontal line is the NRD lifetime saturation value $\tau_{\text{nr}}^{(\text{sat})}$. In Fig. 2.4 we have presented the case depicted in (a). Notice that in (b) and (c) the NRD lifetime features dips (and peaks).

Beside the pure J- and H-aggregates, there exist many cases where the optical selection rules are not so strict as for ideal J- and H-aggregates (see e.g.¹⁰¹). Here one expects that the mechanism discussed in Chap. 2 will play an important role.

2.4 Conclusions and outlook

In conclusion, we have shown that molecular aggregation can modify the NRD lifetime. As a proof of concept, we have considered in detail the simplest molecular aggregate featuring this phenomenon: a transition-dipole-dipole-interacting dimer with harmonic monomer PESs. We have shown that the relationship between the NRD lifetime and the intermolecular-interaction strength depends sensitively on the NRD channel position. In particular the NRD lifetime can increase with, decrease with, or be practically insensitive to the intermolecular-interaction strength. This indicates that quantum yield measurements can, e.g., be exploited for the detection of molecular aggregation; pinpointing of NRD channel locations in molecules; or to infer the geometry of molecular aggregates.

We have so far not considered different values of q_{s} and γ . If q_{s} is larger than in Fig. 2.4, e.g. $q_{\text{s}} = 3.5\sqrt{\hbar/\omega}$, $\tau_{\text{nr}}^{(\text{dim})}$ can feature dips (and peaks) at certain J values — apart from spanning many (e.g. 4 for $q_{\text{nr}} = 2q_{\text{s}}$) orders of magnitude upon varying J . This can be seen in Fig. 2.5. The reason behind these resonance regions is unclear, and they appear to get more and more important as q_{s} gets larger. Unfortunately it is not trivial to perform simulations for values much larger than $q_{\text{s}} = 3.5\sqrt{\hbar/\omega}$ because the size of the integration basis grows with q_{s}^4 . Therefore, it is desirable to obtain a simplified description of these resonances in order to reach an understanding of the NRD dynamics at large q_{s} . For γ much smaller than the one used in Fig. 2.4, $P(t)$ shows oscillations reflecting the underdamped nuclear dynamics, as one can see in Fig. 2.6. However, the main trends observed in Fig. 2.4 are preserved.

For arbitrary (non-harmonic) monomer PESs, the transition dipole-dipole interaction can impose more severe modifications to the NRD dynamics. This is because the shape

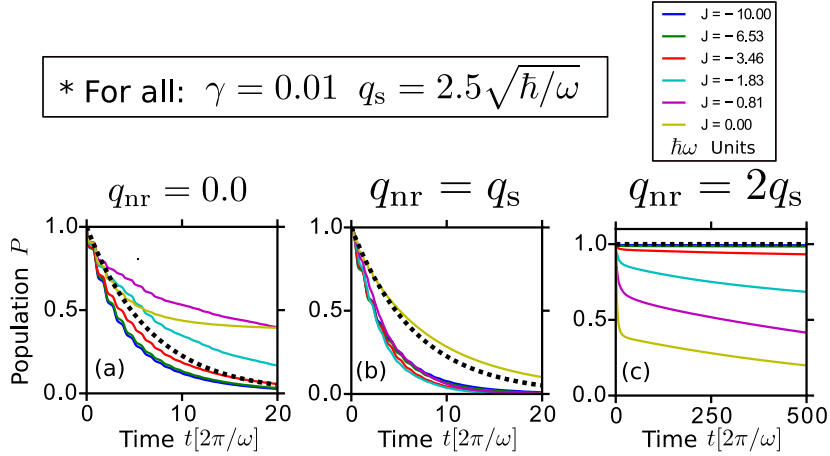


Figure 2.6: Population in the single excitation manifold $P(t)$ as a function of time for different J and q_{nr} values (notice the different x-axis range in (c)). Note that here $\gamma = 0.01$ while in Fig. 2.4 $\gamma = 1$. For comparison, we plot the time-dependent population obtained through the the estimated NRD lifetime saturation value $\tau_{\text{nr}}^{(\text{sat})}$ (black dashed line).

of the dimer PESs from Eq. (2.68) can differ from the monomer excited-state PES's shape. For instance, the dimer's PESs may present a minimum even if the excited-state PES of the monomer does not. This can lead to a fundamental change of the nuclear dynamics in the diabatic case, e.g. stabilizing a photodissociation. Monomer PESs of different shapes will thus give rise to different changes in the NRD dynamics upon aggregation.

Finally, let us mention that besides the mechanism discussed in the Chap. 2, the nonradiative lifetime can also be affected by other means upon aggregation, e.g. steric hindrance of torsional motion in the monomer. However, we want to emphasize that the mechanism discussed here should anyway be considered, since it can strongly change the nonradiative lifetime (and thus the fluorescence quantum yield) despite other coexistent mechanisms.

Chapter 3

Switching between electromechanical regimes in a nanoscale rotor

Nanoelectromechanical systems (NEMS) are a class of nanoscale devices integrating electrical and mechanical functionality, and may thereby surpass the capabilities of conventional nanoscale devices^{102,103}. Typically in NEMS transistor-like nanoelectronic subsystems are coupled to mechanical actuators, pumps, or motors. By that means, NEMS may form physical, biological, and chemical sensors: e.g., NEMS have been shown to be excellent mass^{104–109}, force and pressure^{104,110–113}, and position Ref. [111,114] sensors. Besides sensing, NEMS have also been applied to quantum ground-state preparation and readout in mesoscopic systems^{114,115}, and they hold promise as building blocks of a new generation of mechanical computers^{116,117}.

New effects inherent to the nanoscale can be used to one's advantage when designing novel devices and functionalities. For instance, one can exploit tunneling to strongly correlate current and position. The Coulomb blockade of current, i.e. the suppression of tunnel current above a certain charge threshold, can be used to devise transistor-like circuitry or to attain precise control over the charge in a low capacitance electrode. In 1998, Gorelik, Isacsson, Voinova, Kasemo, Shekhter, and Jonson proposed a NEMS which combines these effects and thereby enables precise control over current^{29,30}. Their NEMS, whose basic operation is sketched in Fig. 3.1, consists of a reciprocating metallic grain shuttling electrons between two flanking leads via tunneling in the Coulomb blockade regime^{*}. A bias voltage across the device serves both the purpose of giving directionality to the current and forcing the charged grain. The grain also experiences a mechanical restoring force pulling it towards the midpoint between the electrodes, and the motion is damped via coupling to external degrees of freedom. The interplay between strongly position-dependent charge tunneling[†], electrostatic and mechanical forcing, and dissipation leads to a steady-state shuttling regime with the following interesting properties: the current that flows through the device is a multiple of a well-defined mechanical frequency, and the current fluctuations are very small¹¹⁹. These features have prompted experimentalists to pursue a realization of the shuttle for more than a decade^{31–33}. Nevertheless, no experiment to date was able to irrefutably demonstrate

^{*}The Coulomb blockade in the system of Gorelik et al. is the suppression of the lead-grain tunneling current when the charge in the grain is above a certain threshold. This implies that the grain can be charged up to $\pm ne$, where n is an integer and e is the elementary charge. n is determined by the grain capacitance C , since the conditions for the Coulomb blockade are that the single-electron charging energy $E_{\text{el}} = e^2/C$ is much larger than both quantum and thermal fluctuations, i.e. $E_{\text{el}} \gg \hbar/RC$ and $E_{\text{el}} \gg k_{\text{B}}T$, where R is the smallest tunnel resistance in the system¹¹⁸, k_{B} is the Boltzmann constant and T is the temperature.

[†]The situation is similar to a tunneling through a potential barrier, where for large enough barrier widths the tunneling probability decays exponentially.

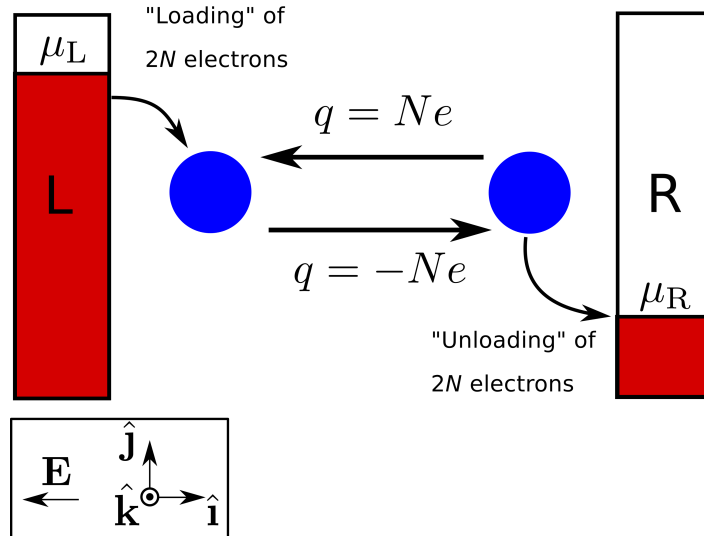


Figure 3.1: Sketch of the basic operation of the electron shuttle from Refs. [29] and [30]. A cyclic change in the direction of motion is due to the repeated “loading” of electrons near the electrode with larger chemical potential μ_L and the subsequent “unloading” at the other electrode. As a result, the sign of the net grain charge alternates leading to a reciprocating grain motion.

the original proposal from Refs. [29] and [30].

An interesting question is whether new physics arise if one replaces the reciprocating grain from the electron shuttle described above with electronic islands (e.g. metallic grain, quantum dot, molecule, etc.) * mounted on a rotor. Rotary dynamics are naturally closer to motor functionality than reciprocating dynamics. This is also reflected on the focus of the first studies on charge-tunneling-driven nanorotors: in 2008, Wang, Vuković, and Král used molecular dynamics simulations to show that driving nanoscale rotary motors by electron tunneling is possible³⁵. In the same year, Smirnov, Savel’ev, Mourokh, and Nori proposed a nanorotor driven by proton tunneling to model and study the dynamics of biomotors³⁶. A different approach emerged in 2012, when Croy and Einfeld aimed at studying the *general* dynamics of a simple nanorotor driven by single-electron tunneling³⁷. Their rotor, which is sketched in Fig. 3.2, is composed of two electronic islands attached to a support shaft via rigid insulating arms. The stator part of their setup is the same as in the electron shuttle from Gorelik et al.^{29,30}. Three dynamical regimes were identified in the device from Croy et al. (two of them are sketched in Fig. 3.3): (i) a standstill regime, (ii) an oscillatory regime, and (iii) a rotatory regime. In (i) the rotor stays still vertically, and this situation is identical to a fixed island tunnel-coupled to two flanking leads. (ii) is somewhat similar to the shuttling regime found in Refs. [29] and [30] — but not identical. While the electron shuttle from Gorelik et al. has a well-defined mechanical frequency, the frequency in (ii) was found to get smaller as one increases the bias voltage across the system. As a result, the *conductance decreases* in response to a *bias increase*. In (iii) positive differential conductance was found and the device can be used as a motor. For the parameter

*With “electronic island” we mean a physical system which has a charged state in which the excess charge is well localized in space.

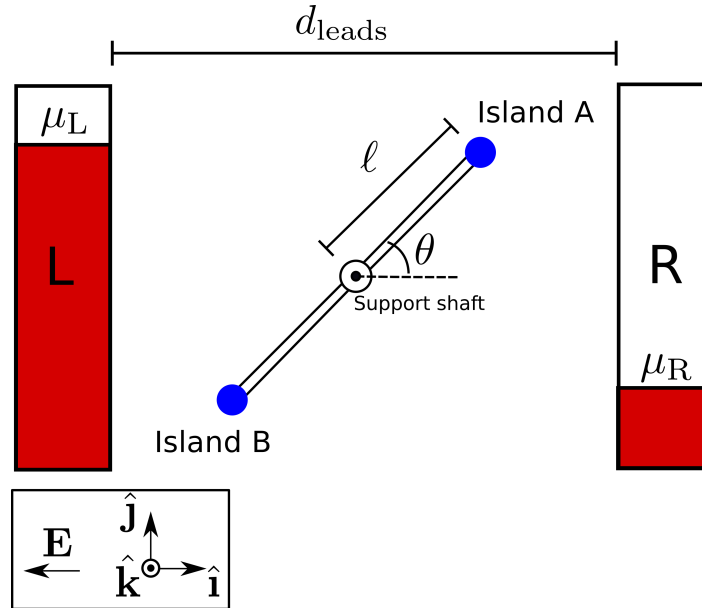


Figure 3.2: Sketch of the setup from Croy and Eisfeld³⁷ and its main parts. The rotor is composed of two electronic islands A and B connected to a support shaft via insulating rigid arms of length ℓ . An uniform electrostatic field \mathbf{E} permeates the region occupied by the rotor. The leads are biased at chemical potentials $\mu_{L(R)}$.

set explored in Ref. [37] the system’s dynamics depend approximately on just two quantities: the ratio of the driving strength to the viscosity and the tunneling length. Exploiting the sensitive dependence of the current on that ratio, one can employ the system to sense viscosity variations in the rotor’s medium by tuning the voltage such as to keep a constant current.

These studies did not touch many questions, and the following have motivated the work presented in this chapter: (a) systems described by nonlinear dynamical equations, of which the rotor is an instance, may present chaos in some region of the parameter space. Is it also possible to have chaotic dynamics in a charge-tunneling-driven rotor? If yes, do these dynamics enable some new functionality? (b) Although in a “classical picture” the dynamics of the rotor are inherently stochastic (due to the charge fluctuations on the islands), it is often useful to have an approximate set of *deterministic* equations of motion for physical understanding. This is exemplified by³⁷, where Croy et al. explained different current and rotational regimes using the corresponding deterministic steady-state trajectories in phase space. However, it is important to know if, and in which parameter regions these deterministic equations agree (at least) qualitatively with approaches that take into account charge fluctuations. (c) Given the interesting phenomenology shown by the deterministic set of equations introduced in Ref. [37], it would be interesting to obtain a limit in which these equations are exact. (d) The experimental realizability of parameter regions of interest can just be fully discussed based on a specific experimental setup. Therefore, it would be desirable to know whether one can propose a setup with which these regions are accessible. (e) In the context of rotary *motors* it is often necessary/useful to have control over the direction of rotation. This can be achieved e.g. by picking an initial condition that leads

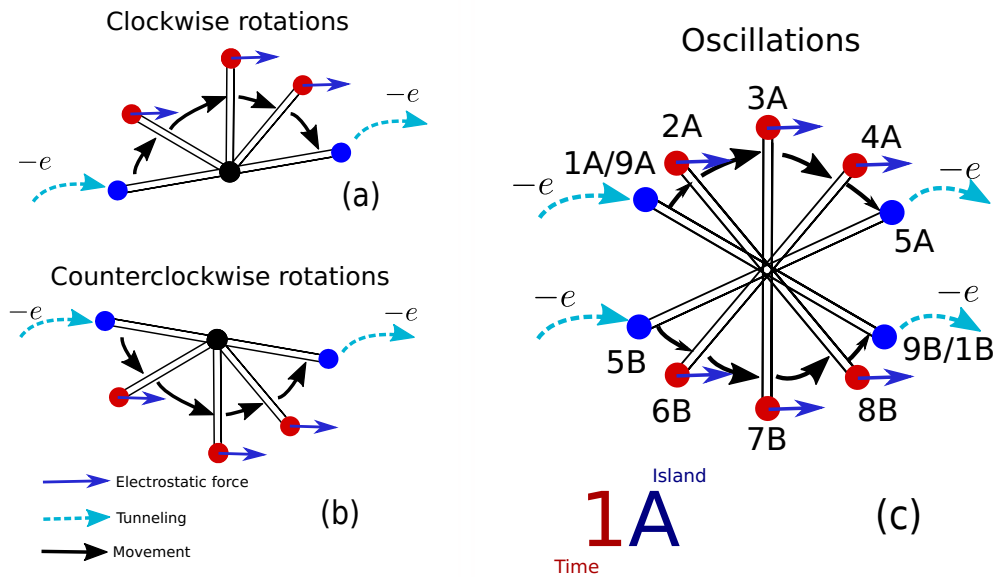


Figure 3.3: Sketch of the (idealized) rotatory and oscillatory dynamics. (a) and (b) Sketch of respectively clockwise and counterclockwise rotatory dynamics (half cycle). (c) Sketch of the oscillatory dynamics (one cycle). The island labels (e.g. 1A) indicate respectively the time ordering and the electronic island that is being represented. For the sake of clarity, we represent just the island that is charged at a given moment in time (and the ones involved in the tunneling events). At time 1 the island A gets charged and the island B gets discharged. From times 2 to 4 A (B) approaches the right (left) lead. At time 5 A gets discharged and B gets charged. From times 6 to 8 B (A) approaches the right (left) lead. At time 9 B gets discharged and A gets charged again, and the cycle is closed.

to the desired direction. However, the experimental preparation of a specific initial condition can be difficult, imprecise or even inconvenient, depending on the system scale, suppression of noise-sources, etc. Moreover, fabrication imperfections can also lead to uncertainty in the direction of rotation. Therefore, it is desirable to somehow introduce a preferable sense of rotation such that at least most of, and ideally all, initial conditions rotate in the same sense^{*}. These questions will be addressed in this chapter.

The chapter is organized as follows: in Sec. 3.1 we use two different sets of equations of motion for the rotor: the (i) “mean-field” equations, where the charge fluctuations are neglected; and the (ii) “stochastic” equations, where the charge fluctuations are fully taken into account. The equations (i) were already studied by Croy et al. in Ref. [37] and we present some of their results. We also show new results using (i), in particular that a new dynamical regime resembling chaos emerges if one considers larger damping than in Ref. [37] (thereby addressing (a)). Moreover, we compare results obtained through equations (i) and (ii) in different parameter regions, thereby addressing (b). We will show that the agreement between the results obtained via (i) and (ii) can be very good or inexistent depending on the damping. In Sec. 3.2 we will address (c) by deriving (i) from the established theory of single-electron tunneling. We also derive (ii).

^{*}Here we mean sense of rotation in *time average*: for a specific initial condition the sense may be inverted from time to time. However, considering times long enough the rotor performs more rotations in one sense than in the other.

The set of equations (i) will be shown to be exactly valid in the limit where the product between the electronic island's capacitance times the bias voltage is much larger than the elementary charge. The question (d) will be addressed in Sec. 3.3, where we propose experimental realizations for the models (from Sec. 3.2) leading to (i) and (ii). We also discuss the assumptions made in Sec. 3.2 and the difficulties in accessing some parameter regions based on those proposals. In Sec. 3.4 we show that by changing the rotor's geometry it is possible to introduce a preferred direction of rotation in both models of Sec. 3.2, this is to address (e). The conclusions of each section are given within that section.

3.1 The dynamics of the mean-field and stochastic equations of motion

In this section we “showcase” the dynamics of the mean-field and stochastic equations of motion of the rotor: in Sec. 3.1.1 we present the mean-field equations and discuss the main results obtained by Croy et al. in Ref. [37] in other parameter regions. In particular, we extend their conclusions to values of damping two orders of magnitude larger than in Ref. [37]. Due to the symmetry of the rotor considered here, the rotatory solutions of the mean-field equations exist in pairs composed of a clockwise and a counterclockwise solution. Different initial conditions may therefore lead to different senses of rotation, and this is discussed in Sec. 3.1.2. We will come back to this discussion later on in Sec. 3.4, where we will break the rotor symmetry to introduce a preferred sense of rotation. In Sec. 3.1.3 we show that a new dynamical regime resembling chaos emerges for larger damping than considered in Ref. [37]. In Sec. 3.1.4 we present the stochastic equations and compare the results obtained using them to those results shown in Sec. 3.1.1 and Sec. 3.1.3. We will see that the results stemming from stochastic and mean-field equations can strongly disagree, specially at large values of damping.

The dynamics shown here have motivated us to derive the mean-field and stochastic equations using the “orthodox” theory of single-electron tunneling (Sec. 3.2) and propose experimental setups which can be described by them (Sec. 3.3).

3.1.1 The dynamics of the mean-field equations revisited

A sketch of the rotor and its main parts can be seen in Fig. 3.2. The rotor is composed of two electronic islands A and B connected to a support shaft via insulating rigid arms of length ℓ (contrastingly, in Ref. [37] ℓ is the full rotor's length). The left/right lead (L/R) is biased to a chemical potential $\mu_{L(R)}$. The chemical potential difference (or, equivalently, the bias voltage $\Delta V_{LR} = (\mu_R - \mu_L) / (-e)$, where e is the [positive] elementary charge) gives rise to a uniform electrostatic field \mathbf{E} permeating the region occupied by the rotor. The rotor is also coupled to some external degrees of freedom which damp the rotational dynamics.

The motion of the rotor is characterized by the angle θ and the corresponding moment of inertia I . The electrons can tunnel between the leads and the electronic islands. An exponential dependence of the tunneling amplitudes on the lead-island distance is assumed. For example, the tunneling amplitude from the left contact to island A

is $T_{L,A} \propto \exp(-\Delta x_{L,A}/\lambda_{L,A})$, where $\Delta x_{L,A}$ is the distance between the left contact and island A, and $\lambda_{L,A}$ is the tunneling length. Analogous expressions are used for the remaining tunneling amplitudes. We express the (inverse) tunneling length by the dimensionless parameter

$$\xi_{L(R),A(B)} = \frac{\ell}{\lambda_{L(R),A(B)}}, \quad (3.1)$$

which from now on we refer to as inverse tunneling length. The islands are considered to have very small capacitances, which implies that their charging is determined by the Coulomb-blockade effect. The Coulomb blockade in this system is the suppression of the lead-island tunneling current when the charge in the island is above a certain threshold. Here, it is further assumed that this threshold is a single electron, such that the island can be either empty or charged with $-e$. The electrons are considered to be transferred sequentially and the tunneling rates W are taken from the orthodox theory of Coulomb blockade⁵⁹:

$$W_{L,A(B)}(\theta_{A(B)}) = \Gamma_{L,A(B)} e^{-\xi_{L,A(B)} \cos \theta_{A(B)}}, \quad (3.2)$$

$$W_{R,A(B)}(\theta_{A(B)}) = \Gamma_{R,A(B)} e^{\xi_{R,A(B)} \cos \theta_{A(B)}}, \quad (3.3)$$

where, for example, $\Gamma_{L,A}$ is defined as the tunneling rate from L to island A when the rotor is upright ($\theta = \pi/2$). $\theta_A = \theta$ and $\theta_B = \theta + \pi$. By means of a large-bias limit assumption³⁷ the tunneling occurs only in one direction: from the left contact to the islands and from the islands to the right contact.

In the mean-field equations of motion just the average charge is taken into account. Denoting the electronic population of island A (B) by $P_{A(B)}$ one can write the average charge of the islands as $Q_{A(B)} = -eP_{A(B)}$, where $P_{A(B)}$ varies continuously between 0 and 1. The time evolution of the electronic populations, which is governed by the tunneling from L and to R, is given by the following rate equation

$$\frac{d}{dt} P_{A(B)} = W_{L,A(B)}(\theta_{A(B)}) (1 - P_{A(B)}) - W_{R,A(B)}(\theta_{A(B)}) P_{A(B)}. \quad (3.4)$$

The first term on the right-hand side describes tunneling from the left lead onto island A (B) and the second term is responsible for tunneling from the island to the right lead. When the island A (B) possesses a charge $Q_{A(B)}$, it experiences a force $-EQ_{A(B)}\hat{\mathbf{i}}$, where E is the magnitude of the electrostatic field \mathbf{E} and $\hat{\mathbf{i}}$ is a unit vector (see the inset in Fig. 3.2). Then, in the mean-field description introduced above, the corresponding torque acting on the rotor is given by $M_{A(B)} = -eEP_{A(B)}\ell \sin \theta_{A(B)}$. We will consider a symmetric setup: $\Gamma_{L(R),A(B)} = \Gamma$ and $\xi_{L(R),A(B)} = \xi$ (for this reason, we will denote the tunneling rates $W_{L(R),A(B)}$ simply as $W_{L(R)}$). The unique Γ can then be used to introduce a dimensionless time,

$$\tau = \Gamma t, \quad (3.5)$$

and a dimensionless driving strength,

$$\eta_0 = \frac{eE\ell}{\Gamma}. \quad (3.6)$$

Considering the dimensionless angular momentum

$$\Lambda = \frac{L}{\Gamma}, \quad (3.7)$$

Table 3.1: Dimensionless quantities used within Sec. 3.1 and their definitions.

Quantity	Symbol	Formula
Time	τ	Γt
Charge (population)	$P_{A(B)}$	$-Q_{A(B)}/e$
Charge (population) difference	ΔP	$P_A - P_B$
Charging rate	$w_{L(R)}(\theta_{A(B)})$	$W_{L(R)}(\theta_{A(B)})/\Gamma$
Angular momentum	Λ	$L/\Gamma I$
Driving strength	η_0	$\ell [eE/\Gamma^2 I]$
Viscosity parameter	γ	$\tilde{\gamma}/\Gamma$

the mean-field equation of motion for the angle is

$$\frac{d}{d\tau}\theta = \Lambda, \quad (3.8)$$

and for the angular momentum,

$$\frac{d}{d\tau}\Lambda = -\eta_0 \sin \theta \Delta P - \gamma \Lambda, \quad (3.9)$$

where the population difference $\Delta P = P_A - P_B$ and the coupling to the environmental degrees of freedom was accounted for through the phenomenological damping term $-\gamma\Lambda$, with γ being the dimensionless rotational viscosity (which we will simply refer to as “viscosity” within this section). Finally, the population difference dynamics follow the equation of motion

$$\frac{d}{d\tau}\Delta P = -2 \sinh(\xi \cos \theta) - 2 \cosh(\xi \cos \theta) \Delta P. \quad (3.10)$$

A definition of the dimensionless quantities used within Sec. 3.1 is given in Tab. 3.1.

3.1.1.1 Quantities of interest

Later on, we will scan over parameters like the η_0 and initial conditions, and it will not be practical to look at every individual trajectory in detail. Therefore, we define some “quantities of interest”, which are time-averaged scalars that can objectively give information over the system dynamics. The same strategy was used in Ref. [37], where the authors employed time averages of the angular momentum and of the current. Following their definition, the time-averaged angular momentum is

$$\langle \Lambda \rangle = \frac{1}{\mathcal{T} - \tau_{\text{tran}}} \int_{\tau_{\text{tran}}}^{\mathcal{T}} \Lambda(\tau) d\tau, \quad (3.11)$$

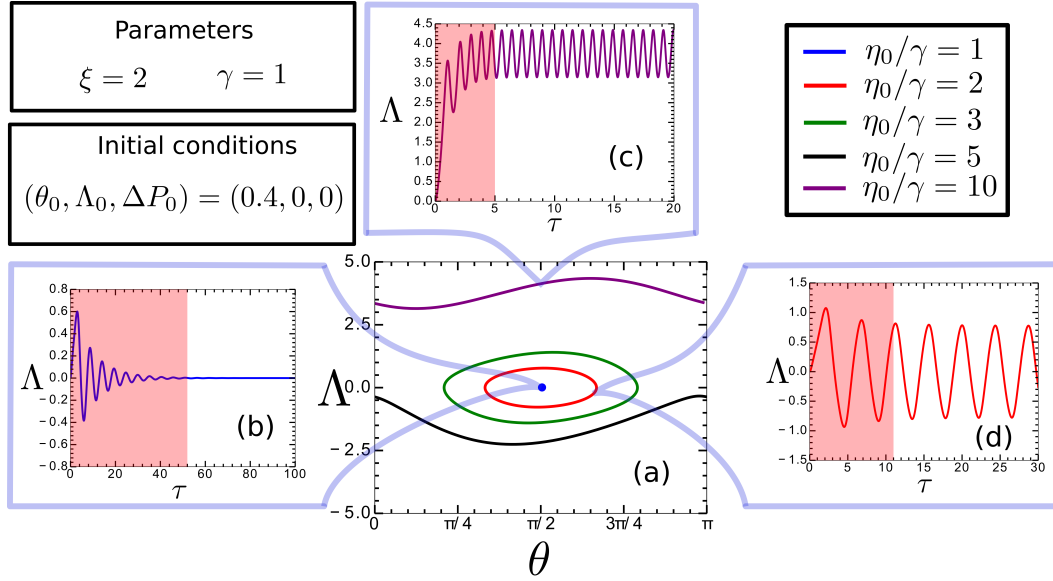


Figure 3.4: Phase portrait of the steady-state dynamics and the time dependence of Λ for all types of dynamical regimes. The different regimes are assessed by changing the values of η_0 . Note that for every rotatory attractor represented by a curve $\Lambda(\theta)$ in this figure there is another one $-\Lambda(\theta)$ which is obtained e.g. through the initial condition $(\theta_0, \Lambda_0, \Delta q) = (-0.4, 0, 0)$. The red-shadowed portions of the figures (b), (c), and (d) correspond to the transient dynamics.

where τ_{tran} is a typical transient time* and \mathcal{T} is sufficiently large to make $\langle \Lambda \rangle$ reach its stationary value (the same will apply to the time-averaged quantities we will define in the following). The dimensionless time-averaged current is

$$\langle \mathcal{J} \rangle = \frac{1}{\mathcal{T} - \tau_{\text{tran}}} \int_{\tau_{\text{tran}}}^{\mathcal{T}} [w_{\text{R}}(\theta(\tau))P_{\text{A}}(\tau) + w_{\text{R}}(\theta(\tau) + \pi)P_{\text{B}}(\tau)]d\tau, \quad (3.12)$$

where we have used the dimensionless rates (see Tab. 3.1)

$$w_{\text{L(R)}}(\theta_{\text{A(B)}}) = \frac{W_{\text{L(R)}}(\theta_{\text{A(B)}})}{\Gamma}. \quad (3.13)$$

Note that one also could define the current using the the rates of tunneling from the left lead to the islands as well:

$$\langle \mathcal{J} \rangle = \frac{1}{\mathcal{T} - \tau_{\text{tran}}} \int_{\tau_{\text{tran}}}^{\mathcal{T}} [w_{\text{L}}(\theta(\tau))(1 - P_{\text{A}}(\tau)) + w_{\text{L}}(\theta(\tau) + \pi)(1 - P_{\text{B}}(\tau))]d\tau. \quad (3.14)$$

3.1.1.2 Dynamics

Eqs. (3.8)-(3.10) define a dissipative dynamical system. Their trajectories approach an invariant set in phase space[†] which is called “attractor”¹²⁰. The type of asymptotic

*In deterministic systems it is well known that a dissipative system needs a certain time τ_{tran} (depending on the initial conditions) to reach with a certain precision an asymptotic manifold in phase space called attractor¹²⁰. For systems described by stochastic differential equations one still has the concept of transient-time, although the concept of attractors as asymptotic manifolds in phase space becomes meaningless¹²¹. This will be important later on when we describe the rotor dynamics using stochastic equations of motion.

[†]The space formed by the dynamical variables Λ , θ , and ΔP .

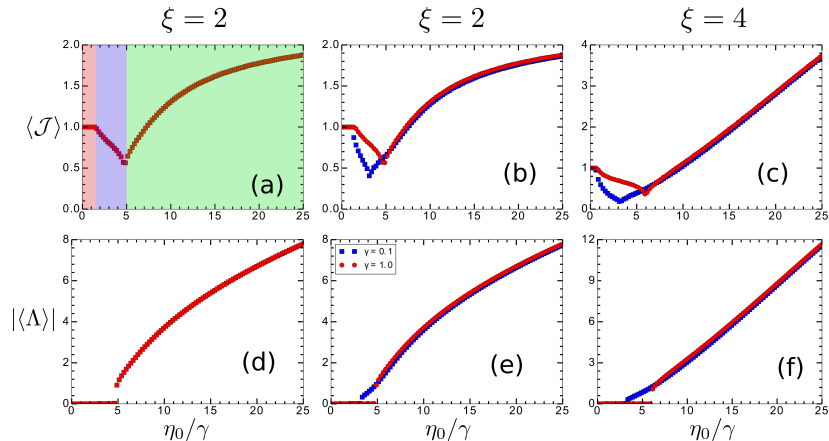


Figure 3.5: Time averages of the current and of the angular momentum as a function of η_0/γ . Time-averaged current $\langle \mathcal{J} \rangle$ and of the absolute value of the time-averaged angular momentum are plotted respectively in the first and second rows. In the first column we plot a curve for $\gamma = 1$ ($\xi = 2$) alone, in the second we add $\gamma = 0.1$ ($\xi = 2$), and in the third we plot curves for $\xi = 4$ (for $\gamma = 0.1$ and $\gamma = 1$). In (a) the standstill, oscillatory, and rotatory regimes are shadowed respectively in red, blue and green.

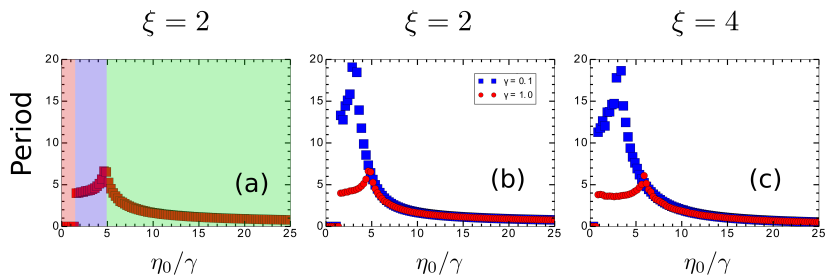


Figure 3.6: Period of the steady-state oscillations/rotations as a function of η_0/γ . For the standstill regime we plot the period as zero. In (a) we plot a curve for $\gamma = 1$ ($\xi = 2$) alone, in (b) we add $\gamma = 0.1$ ($\xi = 2$), and in (c) we plot curves for $\xi = 4$ (for $\gamma = 0.1$ and $\gamma = 1$). In (a) the standstill, oscillatory, and rotatory regimes are shadowed respectively in red, blue and green.

dynamics of this system depends, in general, on all system parameters, i.e. upon the inverse tunneling length ξ , the driving η_0 , and the viscosity γ . Moreover, it can also depend on the initial conditions. In Ref. [37] a region of the parameter space was analysed, where the dependence on η_0 and γ can be approximately simplified to a dependence on the ratio η_0/γ only. Upon increasing that ratio gradually from zero, the asymptotic dynamics goes from standstill to oscillatory and finally to rotatory in this order. The different types of dynamics can be seen in the steady-state phase portrait in from Fig. 3.4, where $\gamma = 1$, $\xi = 2$, and η_0 is varied (different curves). Note that in Ref. [37] $\gamma = 0.01$, i.e. 100 times smaller than the viscosity considered here. Nevertheless, the same dynamics are observed.

Fig. 3.4 shows three types of steady-state dynamics: (b) standstill, (c) oscillatory, and (d) rotatory trajectories. In (a), the attractors for various values of η_0 (different colors) are projected upon the (θ, Λ) plane of the phase space. Different initial conditions lead to the same attractor, apart from the rotatory case where a clockwise-rotating and a

counterclockwise-rotating attractor coexist in phase space. This coexistence will be discussed later on in Sec. 3.1.2. The transient dynamics appear red-shadowed in (b), (c), and (d), where the time dependence of the angular momentum can be seen.

For η_0 small enough, the stationary solution is given by the single (blue) point in Fig. 3.4 (a), located at $\theta = \pi/2$ and $\Lambda = 0$. Electrons tunnel with the constant rate Γ to/from the islands from/to the leads and the charges stay still at $P_A = P_B = 0.5$. The charge current is therefore $\langle \mathcal{J} \rangle = 1$ throughout the parameter region correspondent to the standstill regime,

$$\mathcal{J} = w_R(\theta)P_A + w_R(\theta + \pi)P_B = 1. \quad (3.15)$$

This can be seen in Fig. 3.5 (a), where we plot the current as a function of the ratio η_0/γ for $\gamma = 1$ (standstill regime is red-shadowed).

Upon increasing η_0 , the first transition encountered is to a regime where the rotor oscillates around the position $\theta = \pi/2$. The trajectories in this regime are concentric closed curves (centered at $(\theta, \Lambda) = (\pi/2, 0)$) in the phase space from Fig. 3.4 (a) (see also (c) for the time dependence of Λ). This oscillatory regime resembles the self-excited shuttling from shuttle devices^{29,30}. However, in stark contrast to the conventional charge shuttle, the period of oscillation for the rotor increases with increasing driving³⁷. This is shown in Fig. 3.6, where the period of the rotatory and oscillatory attractors is shown as a function of the ratio η_0/γ . In the oscillatory regime, the period of oscillation spikes at a certain value of η_0/γ which depends on γ and ξ . As explained below, this point marks the transition to the rotatory regime.

Upon increasing η_0/γ within the oscillatory regime, the period of oscillation gets larger because the amplitude increases and thereby the rotor spends more time on the turning points $\theta = 0$ and $\theta = \pi$. For these points the electrostatic torque is null, and thereby the rotation is very slow. This also explains the negative differential conductance* region seen throughout the oscillatory regime in the first row of Fig. 3.5, since the orientations $\theta = 0$ and $\theta = \pi$ carry the smallest current. The limits of the oscillatory regime and the corresponding steepness of the current drop in the η_0/γ axis depend on γ and ξ , as one can see in Fig. 3.5 (b) and (c).

For even larger values of η_0 rotational motion sets in (e.g. see the purple curve for $\eta_0/\gamma = 10$ in Fig. 3.4). The rotatory regime is characterized by a nonzero value of $|\langle \Lambda \rangle|$: in all other dynamical regimes $\langle \Lambda \rangle = 0$. This can be seen in in Fig. 3.5 (d), (e), and (f). We have taken the absolute value because different initial conditions lead to different stationary senses in the rotatory regime, as we can see in Fig. 3.7 (this figure will be discussed in Sec. 3.1.2). Deep in the rotatory regime, the dependence of the angular momentum on η_0/γ was estimated analytically in Ref. [37] to be

$$\Lambda_{\text{stat}} \approx \sqrt{c(\xi) \frac{\eta_0}{\gamma} - d(\xi)}, \quad (3.16)$$

with $c = 2I_1(\xi)$, where I_n is the n th-order modified Bessel function of the first kind. The second term is more difficult to evaluate³⁷, but it also gets less and less important as η_0/γ gets larger. We stress that the asymptotic behavior of $\langle \Lambda \rangle$ just depends on η_0/γ and ξ (and not on η_0 and γ separately).

*“Negative differential conductance” is defined here as the decrease of current in response to an increase of the driving η_0 — which in Ref. [37] is proportional to the voltage drop between the leads.

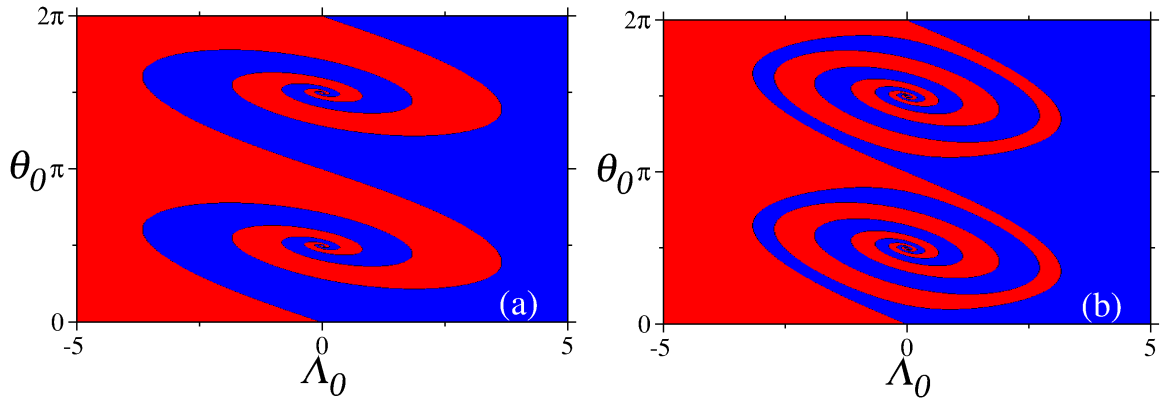


Figure 3.7: Time averaged angular momentum (color) $\langle \Lambda \rangle$ as a function of the initial conditions (Λ_0, θ_0) for $P_A(\tau=0) = P_B(\tau=0) = 0$, $\xi = 2.0$, $\gamma = 1$ and (a) $\eta_0/\gamma = 10.0$ (b) $\eta_0/\gamma = 5.0$. Red stands for clockwise (negative $\langle \Lambda \rangle$) and blue for counter-clockwise (positive $\langle \Lambda \rangle$) rotation direction. These results were obtained using the mean-field equations Eqs. (3.8)-(3.10).

The time-averaged current is independent of the initial condition and, in particular, of the direction of rotation in the rotatory regime. Numerical results are shown in Fig. 3.5 (a), (b), and (c). In contrast to the oscillatory regime, the rotatory regime shows solely a positive differential conductance. In the limit of very large ratio η_0/γ , the stationary current reaches a constant value, which was determined in Ref. [37] to be

$$\langle \mathcal{J} \rangle_{\text{stat}} = I_0(\xi). \quad (3.17)$$

We stress that the asymptotic current from Eq. (3.17) depends just on ξ , and, particularly, gets larger for larger ξ . Analogously, by comparing Fig. 3.5 (e) to (f) we observe that all structures in these figures get larger in the y axis for larger ξ (notice the different scale on the y axis).

Now we turn our attention to the dependence of the rotational direction upon the initial conditions in the rotatory regime. As we have already mentioned, clockwise and counterclockwise rotatory attractors always coexist, and now we want to determine the sets of initial conditions converging to a single attractor. These sets are called basins of attraction.

3.1.2 Basins of attraction in the case of a symmetric rotor

The rotor model discussed in Sec. 3.1.1 is a “symmetric rotor”, in that to every initial condition leading to a trajectory with $\Lambda(\tau)$ there is another one leading to $-\Lambda(\tau)$. The most striking consequence of this symmetry is that every clockwise-rotating attractor coexists with a counterclockwise-rotating one. Although the properties of the initial condition space were not investigated in Ref. [37], the authors mentioned the bistability in that space when presenting the curves of $\langle \Lambda \rangle$ as a function of η_0/γ (this bistability prompted them to show $|\langle \Lambda \rangle|$ instead of $\langle \Lambda \rangle$). Here we determine the origins of this symmetry as an invariance in the equations of motion Eqs. (3.8)-(3.10). Moreover, we analyze the properties of the basins of attraction for opposite senses of rotation in the (θ_0, Λ_0) projection of the initial condition space. Later on, in Sec. 3.4, we will break the aforementioned symmetry to avoid needing to have information about the initial

condition in order to choose a certain sense of rotation. This may be desirable in the context of nanomotors.

Invariances of the equations of motion Eqs. (3.8)-(3.10)

Solutions of Eqs. (3.8)-(3.10) possess the following invariance: substituting $\tilde{\Lambda} = -\Lambda$ and $\tilde{\theta} = -\theta$ *simultaneously* in these equations, i.e. changing the direction of rotation and reflecting around $\theta = 0$ ($\theta = \pi$), one obtains the same equation. The same is achieved by (ii) substituting $\tilde{\Lambda} = -\Lambda$, $\tilde{\theta} = -\theta + \pi$, and $\tilde{\Delta}q = -\Delta q$, i.e. changing the direction of rotation, the charge difference, and reflecting around $\theta = \pi/2$ ($\theta = 3\pi/2$). Due to these invariances, for every counterclockwise (positive Λ) rotating solution with initial condition (Λ_0, θ_0) there is another clockwise (negative Λ) rotating one with initial condition $(-\Lambda_0, -\theta_0)$. This invariance will be of fundamental importance in Sec. 3.4 when we consider the time-averaged angular momentum $\langle \Lambda \rangle$, averaged over initial angles θ_0 for a rotor initially discharged ($P_A(\tau=0) = P_B(\tau=0) = 0$) and at rest ($\Lambda_0 = 0$)

$$\overline{\langle \Lambda \rangle} = \frac{1}{2\pi} \int_0^{2\pi} d\theta_0 \langle \Lambda \rangle. \quad (3.18)$$

This quantity becomes exactly zero in the presence of this invariance. Our objective in Sec. 3.4 will be to break this invariance such that $\overline{\langle \Lambda \rangle} \neq 0$, which indicates that the rotor possesses a preferred direction of rotation.

Numerical calculation of the basins of attraction in the rotatory regime

Fig. 3.7 is an example on how one can use the time-averaged angular momentum defined by Eq. (3.11) to obtain information about the dynamics without looking at the trajectories. Using $\langle \Lambda \rangle$, we determine the basins of attraction of the two rotatory attractors corresponding to $\gamma = 1$, $\xi = 2$, (a) $\eta_0 = 5$ and (b) $\eta_0 = 10$. Red stands for clockwise (negative $\langle \Lambda \rangle$) and blue for counterclockwise (positive $\langle \Lambda \rangle$) rotation direction. Throughout the initial-condition space, for both negative and positive $\langle \Lambda \rangle$, one has the same $|\langle \Lambda \rangle|$. Note that in Fig. 3.4 (a), for which $\gamma = 1$ and $\xi = 2$, just one rotatory attractor per value of η_0 appears because we have considered a single initial condition.

In both Fig. 3.7 (a) and (b) one observes intertwined patterns spiraling towards $(\theta_0 = \pi/2, \Lambda_0 = 0)$ and $(\theta_0 = 3\pi/2, \Lambda_0 = 0)$. Those points correspond to a standstill situation ($\Lambda = 0$) with the rotor in a vertical orientation. Both locations are fixed points in phase space: Once the system reaches those states, it stays there forever. The spiraling pattern around those fixed points can be understood as follows: the rotor transiently oscillates and as it swings it gains energy until it reaches the rotatory steady-state. In each half oscillation the rotor has the chance to set into the rotatory steady-state with a certain rotation direction. If it does not have enough energy, it performs another half oscillation gaining more energy and having the opportunity to start rotating in the opposite direction. This process is repeated until the stationary rotatory state is reached, whose direction depends on the initial condition of the rotor. For initial conditions closer to the fixed points a larger number of oscillations is required to reach the steady-state*, and small changes in the initial conditions can lead to a

*In the vicinity of those fixed points a small charge imbalance builds up, leading to a torque that

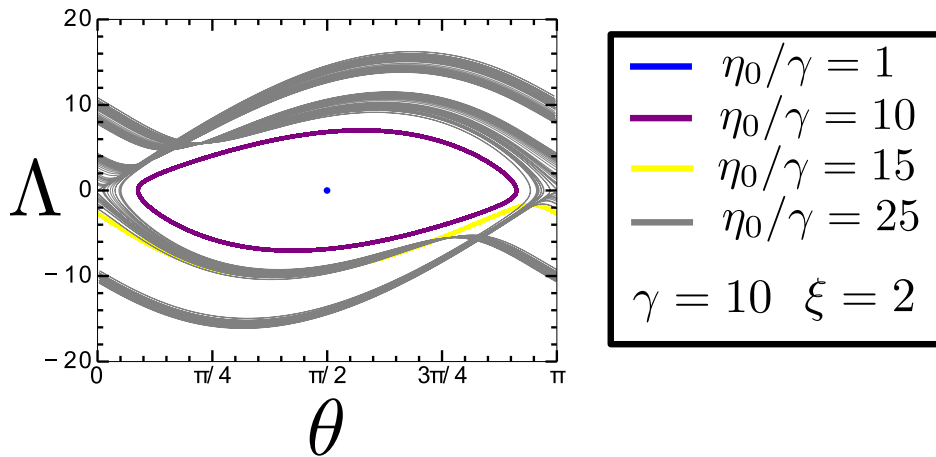


Figure 3.8: Phase portrait of the steady-state dynamics featuring the new dynamical regime. To generate these plots, we considered an initially discharged rotor and $(\theta_0, \Lambda_0) = (0.4, 0)$. Curves of different colors were calculated with a different value of η_0 . We have plotted the gray attractor (from the new regime found in this thesis) in an exceptionally thin line for better visualization of the attractor's fine structure.

different direction of rotation. This fact causes the complex spiraling pattern seen in Fig. 3.7. As one decreases the driving strength η_0 the rotor gains energy more slowly, and therefore more and more oscillations are required in order to reach the rotatory regime. The larger number of oscillations leads to finer spiraling patterns, as seen in Fig. 3.7 (b) compared to (a).

In Fig. 3.7 one can also see a consequence of the invariance discussed above, namely an anti-symmetry around $(\theta_0, \Lambda_0) = (0, 0)$ (also $\theta_0 = \pi$) and $(\theta_0, \Lambda_0) = (\pi/2, 0)$ (also $\theta_0 = 3\pi/2$). That anti-symmetry implies in particular that $\overline{\langle \Lambda \rangle} = 0$. In Sec. 3.4 we will show how one can induce a preferred rotation direction, i.e. how to make $\overline{\langle \Lambda \rangle} \neq 0$, even in the case when the angular momentum is initially zero.

3.1.3 A new dynamical regime

Considering the results obtained in Ref. [37], for $\gamma = 0.01$ ($\xi = 2$), and the results we have shown in Sec. 3.1.1, for $\gamma = 0.1$ and $\gamma = 1$, the dynamics have not changed qualitatively over 2 decades of the viscosity parameter: no new dynamical regime has appeared and the curves of $\langle \mathcal{J} \rangle$ and $\langle \Lambda \rangle$ as a function of η_0/γ are qualitatively the same. Notice that none of the dynamical regimes shown until now are chaotic.

A new, apparently chaotic* regime emerges at $\gamma = 10$ ($\xi = 2$). A typical attractor from this regime can be seen in the steady-state phase portrait from Fig. 3.8 (gray curve), alongside standstill, oscillatory and rotatory attractors. Surprisingly, this new regime appears as one increases the driving further away of the rotatory regime.

drives an oscillation. As the time goes on the oscillation is amplified until the rotor starts to rotate. Notice that the closer one starts from the referred points the smaller the first oscillation amplitude is, and therefore one needs more oscillations until the rotor starts rotating.

*We did not perform any formal assessment of the chaoticity of the attractors within this regime (e.g. calculation of the Lyapunov exponents¹²⁰).

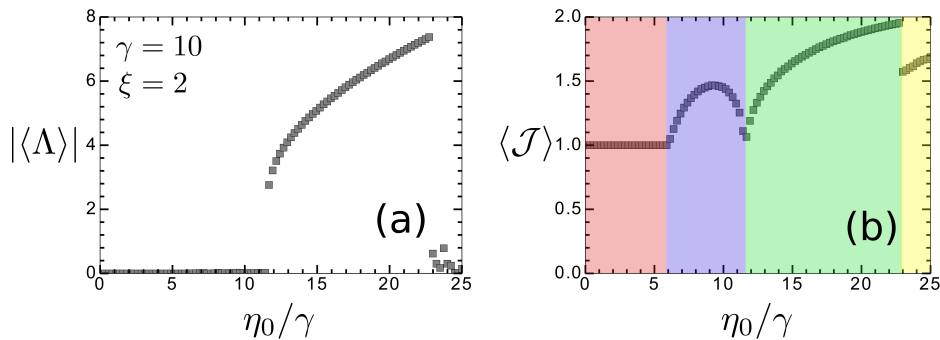


Figure 3.9: Time averages of (a) the angular momentum and of (b) the current as a function of η_0/γ featuring the new dynamical regime found in this thesis. In (b) the standstill, oscillatory, rotatory regimes are shadowed respectively in red, blue and green. The new regime appears yellow-shadowed.

As one can guess from Fig. 3.8, the attractor depicted in gray has a very small (possibly zero) value of $\langle \Lambda \rangle$. The time averaged angular momentum as a function of η_0/γ can be seen in Fig. 3.9 (a). The transition from the rotatory to the new regime found here is characterized by a sudden decrease of $\langle \Lambda \rangle^*$. This transition can also be seen in Fig. 3.9 (b), where we plot the current $\langle \mathcal{J} \rangle$ as a function of η_0/γ : when the dynamics transition to this new regime (yellow-shadowed) a discontinuity in the current is observed.

3.1.4 Stochastic equations of motion

In the model considered in Secs. 3.1.1-3.1.3 the islands have two charging states: they are either discharged or charged with a single excess electron. In such a situation, it is not clear whether/when one can neglect the charge fluctuations on the islands. However the mean-field approach presented in Sec. 3.1.1 was used throughout Secs. 3.1.1-3.1.3, and it neglects charge fluctuations. In this section we introduce a new set of equations which fully takes into account charge fluctuations. Similar approaches were used in Refs. [36] and [38] for rotors driven by charge tunneling, and in many works for the electron shuttle (e.g. in Refs. [29] and [30]). We compare then the results for the time averages of the current and of the angular momentum obtained with this set of (stochastic) equations to the ones obtained with the mean-field equations (Secs. 3.1.1.2 and 3.1.3).

We start by rewriting Eq. (3.9) as

$$\frac{d}{d\tau} \Lambda = -\eta_0 \sin \theta (P_A - P_B) - \gamma \Lambda, \quad (3.19)$$

where $P_{A(B)}$ are the electronic populations on the islands A (B), but now they can assume just the discrete values 0 (discharged) or 1 (charged with a single excess electron). The electronic populations are now stochastic quantities, and the transition rates are given by the dimensionless tunneling rates defined by Eq. (3.13). In other words, the

*While we could not prove that $\langle \Lambda \rangle$ is exactly zero, it is always very small for all parameter combinations we evaluated numerically.

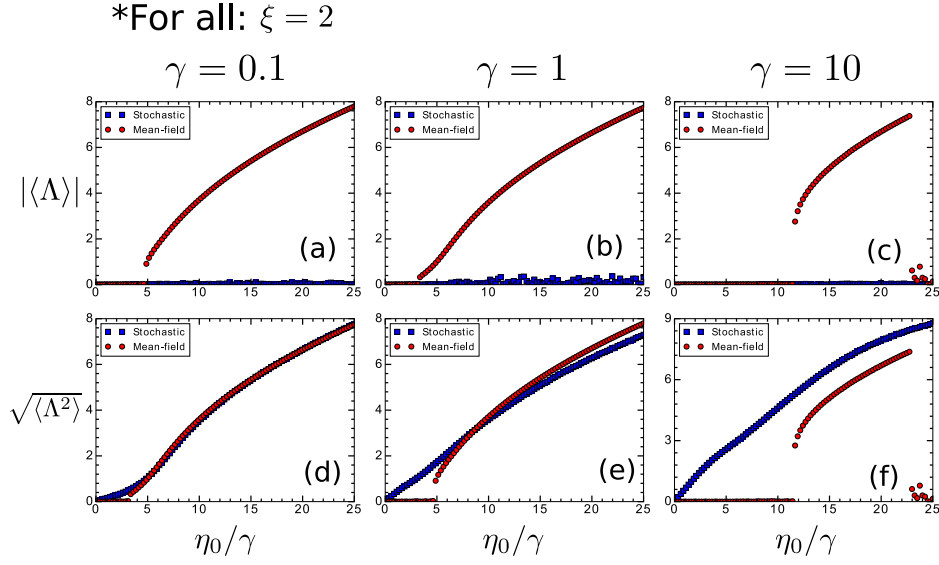


Figure 3.10: Time averages of (first row) the angular momentum and of (second row) the angular momentum squared as a function of η_0/γ for mean-field (red circles) and stochastic (blue squares) equations of motion. For the stochastic equations we additionally average both quantities over 1000 realizations, limited the time of integration to $\mathcal{T} = 200$ and discarded a transient of $\tau_{\text{tran}} = 100$.

probability of transition from $P_{A(B)} = 0$ to $P_{A(B)} = 1$ within the time infinitesimal $d\tau$ is

$$\mathcal{P}_{A(B)}^+ = w_L(\theta_{A(B)}) d\tau, \quad (3.20)$$

and from $P_{A(B)} = 1$ to $P_{A(B)} = 0$ is

$$\mathcal{P}_{A(B)}^- = w_R(\theta_{A(B)}) d\tau. \quad (3.21)$$

Eq. (3.8) remains the same

$$\frac{d}{d\tau} \theta = \Lambda. \quad (3.22)$$

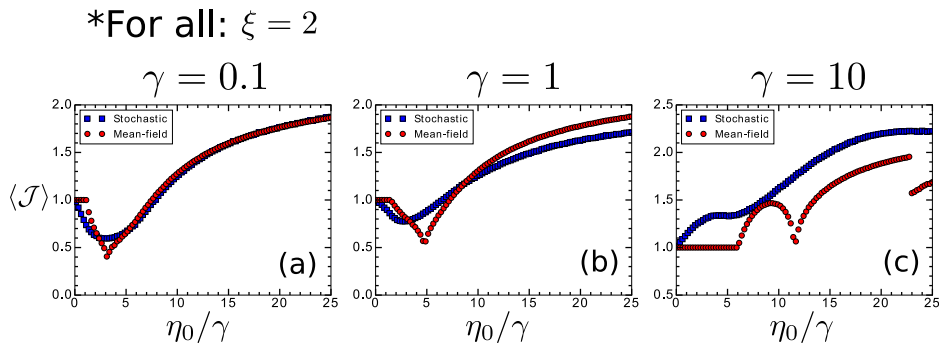


Figure 3.11: Time-averaged current as a function of η_0/γ for mean-field (red circles) and stochastic (blue squares) equations of motion. For the stochastic equations we additionally average the current over 1000 realizations.

The stochastic equations defined by Eqs. (3.19)-(3.22) are equivalent to a set of deterministic equations for the probability density in phase space (θ, Λ) (see Ref. [122], equation (3.4.22)). Herewith, we refer to these equations as “Fokker-Planck equations”^{*}. They are given by

$$\begin{aligned} \frac{d}{d\tau} P_{00}(\tau, \theta, \Lambda) = & \left[\left(-\Lambda \frac{\partial}{\partial \theta} - w_L(\theta_A) - w_L(\theta_B) \right) + \mathcal{B}(\Lambda) \right] P_{00} + \\ & w_R(\theta_A) P_{01} + w_R(\theta_B) P_{10}, \end{aligned} \quad (3.23)$$

$$\begin{aligned} \frac{d}{d\tau} P_{01}(\tau, \theta, \Lambda) = & \left[\left(-\Lambda \frac{\partial}{\partial \theta} + \eta_0 \sin \theta \frac{\partial}{\partial \Lambda} - w_R(\theta_A) - w_L(\theta_B) \right) + \mathcal{B}(\Lambda) \right] P_{01} + \\ & w_L(\theta_A) P_{00} + w_R(\theta_B) P_{11}, \end{aligned} \quad (3.24)$$

$$\begin{aligned} \frac{d}{d\tau} P_{10}(\tau, \theta, \Lambda) = & \left[\left(-\Lambda \frac{\partial}{\partial \theta} - \eta_0 \sin \theta \frac{\partial}{\partial \Lambda} - w_R(\theta_B) - w_L(\theta_A) \right) + \mathcal{B}(\Lambda) \right] P_{10} + \\ & w_R(\theta_A) P_{11} + w_L(\theta_B) P_{00}, \end{aligned} \quad (3.25)$$

$$\begin{aligned} \frac{d}{d\tau} P_{11}(\tau, \theta, \Lambda) = & \left[\left(-\Lambda \frac{\partial}{\partial \theta} - w_R(\theta_A) - w_R(\theta_B) \right) + \mathcal{B}(\Lambda) \right] P_{11} + \\ & w_L(\theta_A) P_{10} + w_L(\theta_B) P_{01}, \end{aligned} \quad (3.26)$$

where $P_{a,b}(\tau, \theta, \Lambda)$ is the probability density in the phase space (θ, Λ) for having $P_A = a$ and $P_B = b$ at the time τ , with $a, b \in \{0, 1\}$; and the operator

$$\mathcal{B}(\Lambda) = \gamma \frac{\partial}{\partial \Lambda} \Lambda = \gamma \left(1 + \Lambda \frac{\partial}{\partial \Lambda} \right). \quad (3.27)$$

3.1.4.1 Time averages of the current and of the angular momentum

In the first row of Fig. 3.10 we plot the absolute value of the time-averaged angular momentum as a function of η_0/γ , obtained with the mean-field (red circles) and stochastic (blue squares) equations of motion. In the latter case, we additionally average $\langle \Lambda \rangle$ over 1000 realizations. Notice that in the stochastic case $\langle \Lambda \rangle$ will always vanish for times long enough because fluctuations can always randomly sum up to invert the direction of rotation. In our stochastic simulations, we limited the time of integration to $\mathcal{T} = 200$ and discarded a transient of $\tau_{\text{tran}} = 100$.

In the second row of Fig. 3.10 we compare $\sqrt{\langle \Lambda^2 \rangle}$ (stochastic equations) to $|\langle \Lambda \rangle|$ (mean-field equations). Since $\langle \Lambda \rangle$ vanishes in the oscillatory regime and in the new regime found in this thesis, comparison makes sense only in the rotatory regime. For (d) $\gamma = 0.1$ the results obtained via the mean-field and the stochastic equations agree very well, but they disagree more and more as we increase the viscosity, first to (e) $\gamma = 1$ and then to (f) $\gamma = 10$.

A similar trend is observed for the time-averaged current, which can be seen in Fig. 3.11. For (a) $\gamma = 0.1$ the only strong difference between the mean-field and the stochastic case is that the latter does not feature a standstill regime (where the

^{*}The equation (3.4.22) is called “differential Chapman-Kolmogorov equation” in Ref. [122], and it is named “Fokker-Planck equation” when no jump processes are involved (in our case, electron tunnelings).

time-averaged current is constantly equal to 1). All the values agree very well, specially in the rotatory regime. However, for (b) $\gamma = 1$ the region of negative differential conductance is shifted to smaller values of η_0/γ , and the values in the rotatory regime do not agree so well as in (a). In (c) $\gamma = 10$ the curves disagree both qualitatively and quantitatively. Remarkably, the discontinuity which characterizes the transition to the new regime we report in this thesis is completely erased by the charge fluctuations.

3.1.5 Conclusions

In this section we have showcased the dynamics of the mean-field and stochastic models. The mean-field dynamics were already studied in detail in Ref. [37], where Croy et al. identified three regimes: the standstill, the oscillatory, and the rotatory. They also suggested possible applications of these dynamics, e.g. for sensing and electron pumping³⁷.

Our results show that new phenomena can arise for stronger dissipation in the mean-field equations. In particular, we showed in Sec. 3.1.3 that a new, chaotic-like dynamical regime emerges. The transition from the rotatory to this new regime is characterized by a discontinuous change in the time averages of the current and of the angular momentum. This strong response of the system to a minute variation of the parameters could be used e.g. to realize a nanoswitch, if there is a system in the nanoscale which is well described by the mean-field equations of motion within the parameter region where that new regime appears.

The comparison between mean-field and stochastic equations of motion we presented in Sec. 3.1.4 shows that their dynamics can differ completely, specially for larger values of viscosity. In special, our results seem to indicate that, in a system driven by a small number of electrons, the charge fluctuations erase the aforementioned discontinuity, thereby frustrating the chances of realizing the nanoswitch.

Because of the discrepancy between the mean-field and stochastic results, it is important to know which assumptions are made when using which model. Therefore, in the next section we derive the mean-field and stochastic equations from the “orthodox” theory of single-electron tunneling.

3.2 A model of the nanoelectromechanical rotor based on the “orthodox” theory of single-electron tunneling

In the last section we dynamics of the mean-field and stochastic models. These models show interesting dynamics which can be used for many purposes: e.g. the transition from the rotatory regime to the chaotic-like regime in the mean-field model can be used to realize a nanoswitch. However, the mean-field and stochastic results disagree in certain parameter regimes (specially for large damping). Therefore, it is desirable to know which assumptions are made when using which model. With that goal in mind, in this section we derive these models from the “orthodox” theory of single electron tunneling developed by Averin and Likharev in 1985⁵⁹.

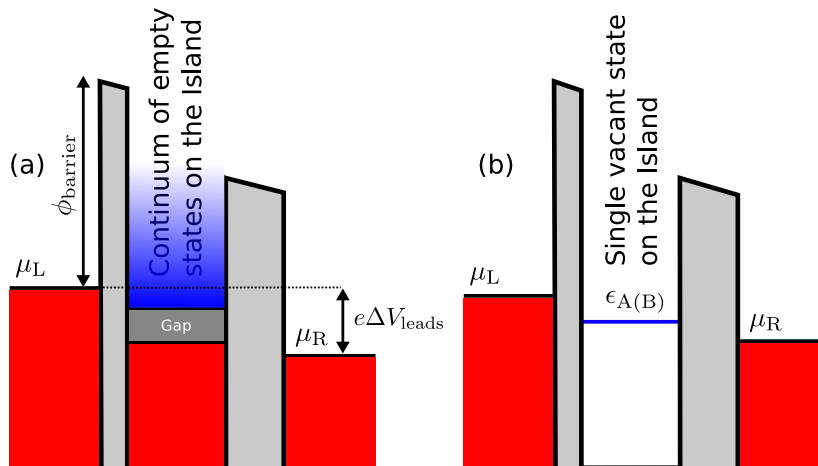


Figure 3.12: Band-edge-profile models of the double tunnel junction formed by an island between two leads. Note that the island is oversized for clarity. On the leads: red stands for occupied states and white for vacant states. (a) A continuum of states in the island participates in the electronic transport (blue). The gap (dark gray) corresponds to the charging energy. (b) A single state in the island (of energy $\epsilon_{A(B)}$) participates in the electronic transport (blue line).

We consider the same system presented in Sec. 3.1.1, except by the fact that here the islands A and B can bear more than a single excess electron. Following the orthodox theory of single-electron tunneling, which is presented in Sec. 3.2.1, we derive expressions for the rates of lead-island charge tunneling using golden-rule arguments. We obtain these rates for the case of a continuous energy spectrum on the island in Sec. 3.2.1.1, and for a single energy level on the island in Sec. 3.2.1.2. The mechanical equations of the rotor are discussed in Sec. 3.2.2.

We specialize the tunneling rates obtained in Sec. 3.2.1 for the case where the islands can be either discharged or charged with a single excess electron in Sec. 3.2.3. The specialized rates are the same as the ones used in Sec. 3.1.4, and, together with the mechanical equations discussed in Sec. 3.2.2 (at temperature $T \rightarrow 0$), they lead to stochastic equations of motion of the rotor. We also explore the opposite limit, where the islands can bear a maximal excess charge much larger than the elementary charge e in Sec. 3.2.4. This procedure leads to a deterministic set of equations of motion, i.e. without charge fluctuations. If the “bias energy” (voltage times e) is large compared to both thermal and “charging” (energy necessary to charge the island with one electron) energies, these deterministic equations are the same as the mean-field equations.

3.2.1 Orthodox theory of single-electron tunneling for a single island

The objective of this section is to obtain rates of tunneling between the contacts and a single island. Our approach is to write down a Hamiltonian which contains the degrees of freedom of a single island and of the contacts, with the mechanical degree of freedom being included only parametrically. The degrees of freedom of the other island do not enter that Hamiltonian because we regard no coupling between the islands. Using

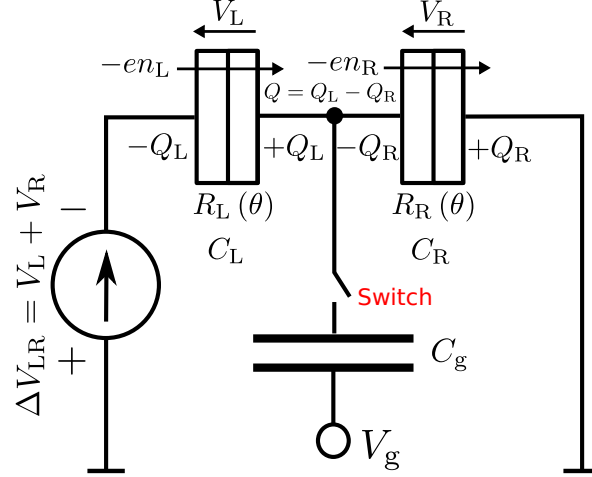


Figure 3.13: Circuit representation of the double tunnel junction formed by an island (A or B) and the leads with the additional gate electrode, which will be introduced later on. Note that this system is equivalent to a single-electron transistor¹²³.

the coupling between the island and the leads, and with the aid of the golden rule of quantum mechanics, we derive expressions for the tunneling rates.

In the nanoscale, electronic islands of smaller dimensions tend to feature energy spectra whose discreteness needs to be taken into account; in contrast, larger islands, possibly reaching the microscale (see the experimental proposal of Sec. 3.3.2), tend to show continuous energy spectra in the scale of interest. Therefore, we focus on the two extreme situations depicted respectively in Fig. 3.12 (a) and (b). In both cases the island, together with the leads, can be seen as a double tunnel junction. The circuit sketched in Fig. 3.13 is equivalent to this double tunnel junction if the switch is turned off. Later on in this section, we will discuss the possibility of coupling a gate electrode capacitively to the islands in order to overcome the Coulomb blockade of current in the device we propose in Sec. 3.3.1 (switch turned on). The difference between Fig. 3.12 (a) and (b) is that in (a) the energy spectrum of the island is continuous while in (b) there is just one energy level in the transport window. This will lead to a fundamental difference when calculating the total tunneling rate through the junctions: in (a) it varies linearly with the lead-island voltage drop $V_{L(R)}$ because the number of states involved in the charge transport is proportional to $V_{L(R)}$; contrastingly, in (b) it is insensitive to $V_{L(R)}$ because there is just one energy level involved in the transport regardless of $V_{L(R)}$.

For both cases from Fig. 3.12, the Hamiltonian is¹²⁴

$$H = H_{\text{isl}} + H_{\text{tun}} + H_L + H_R + H_C, \quad (3.28)$$

where the island Hamiltonian $H_{\text{isl}} = \sum_{\mathbf{k}, \sigma} \epsilon_{\mathbf{k}} c_{\mathbf{k}, \sigma}^\dagger c_{\mathbf{k}, \sigma}$ describes noninteracting electrons with wave vector \mathbf{k} and spin σ ; $c_{\mathbf{k}, \sigma}^{(\dagger)}$ is the annihilation (creation) operator for a mode (\mathbf{k}, σ) . Similar expressions hold for the Hamiltonians $H_{L(R)}$ of the leads (with wave vectors \mathbf{k}_L and \mathbf{k}_R). Note that since the islands A and B are identical, all the arguments are valid for both of them and therefore we often drop the notation indicating the island (A (B)). The Coulomb interaction is assumed to depend only on the charge on the

island

$$H_C = \frac{\hat{n}^2 e^2}{2C}, \quad (3.29)$$

where $\hat{n} = \sum_{\mathbf{k},\sigma} c_{\mathbf{k},\sigma}^\dagger c_{\mathbf{k},\sigma}$ is the number operator of excess electrons on the island, and $C = C_L + C_R$ where $C_{L(R)}$ is the capacitance of the left (right) tunnel junction. Charge-transfer processes are described by the standard tunneling Hamiltonian¹²⁴

$$H_{\text{tun}} = \sum_{\mathbf{k},\mathbf{k}_L,\mathbf{k}_R,\sigma} M_{\mathbf{k},\mathbf{k}_L} c_{\mathbf{k},\sigma}^\dagger c_{\mathbf{k}_L,\sigma} + M_{\mathbf{k},\mathbf{k}_R} c_{\mathbf{k},\sigma}^\dagger c_{\mathbf{k}_R,\sigma} + \text{h.c.}, \quad (3.30)$$

where $M_{f,i}$ are the tunnel matrix elements from a state i to a state f . Since these elements are overlap integrals of states in different electrodes (island/leads), they depend on the position operator of the island ($\hat{\mathbf{r}}$): $M_{f,i} = M_{f,i}(\hat{\mathbf{r}})$.

We determine tunneling rates using golden-rule arguments¹²⁴, which amounts to energy conservation within the tunneling process. Tunneling can happen between a lead and an island: island-island tunneling and lead-lead tunneling are neglected. The tunneling rate from an initial state of energy ϵ_i within an island/lead to a final state of energy ϵ_f within a lead/island is

$$W_{i \rightarrow f}(\Delta F) = \frac{2\pi}{\hbar} |M_{f,i}|^2 \delta(\epsilon_i - \epsilon_f - \Delta F), \quad (3.31)$$

where $\Delta F = F_f - F_i$ is the variation in the Helmholtz free energy of the system. The Helmholtz free energy here is defined as the maximum useful work extractable from the device by discharging the island, i.e. $n \rightarrow 0$, where n is the number of excess electrons on the island*. The total energy stored in the device is given by

$$E_{\text{tot}} = \frac{Q_L^2}{2C_L} + \frac{Q_R^2}{2C_R} + S(n) = \frac{C_L C_R \Delta V_{LR}^2 + n^2 e^2}{2C} + S(n), \quad (3.32)$$

where $Q_{L(R)}$ and $C_{L(R)}$ are respectively the stored charge and the capacitance of the single junction formed by the island and the lead L (R) (see Fig. 3.13). $S(n)$ is composed by the Fermi and confinement energies, and they tend to become more important when the dimensions of the island become smaller. The form of $S(n)$ is not relevant in the following. In Eq. (3.32) we have considered the following relations: $Q = Q_L - Q_R = -en$ (net charge in the island)[†], $\Delta V_{LR} = V_L + V_R$, $Q_L = C_L V_L$, and $Q_R = C_R V_R$, where the positive quantity V_L (V_R) is the voltage drop between L (R) and the island. All these quantities are represented in Fig. 3.13.

Not all the total stored energy can be transformed into useful work: to discharge the island one needs to “pay back” some of the work done by the power source in charging the island. If n_L electrons tunnel inside the island from the left lead, the power source needs to replace these electrons in L. However, the charge variation in the island changes the voltage drop between L and the island (V_L), leading to a change of polarization

*More precisely, if $n > 0$ it is the number of electrons on the island; if $n < 0$ then $-n$ is the number of holes on the island.

†We neglect any background charge since it can be suppressed in the device with the additional gate electrode¹²³.

charge in the left lead. We can write V_L and V_R noting that $n = n_L - n_R$ (see Fig. 3.13):

$$V_L = \frac{C_R \Delta V_{LR} - en}{C}, \quad (3.33)$$

$$V_R = \frac{C_L \Delta V_{LR} + en}{C}. \quad (3.34)$$

So, the variation in polarization charge in the left lead due to the injection of n_L electrons in the island is $\Delta V C_L = (en_L/C) C_L$, and the total charge to be replaced by the voltage source is $-en_L(1 - C_L/C) = -en_L C_R/C$. Since the voltage in that lead is $-\Delta V_{LR}$, the work done by the power source is $\Delta V_{LR} en_L C_R/C$. Note that the polarization charge also changes in the right lead, but the voltage there is 0 according to the convention adopted here. Similar considerations allow us to calculate the work done by power source when n_R electrons leave the island: $\Delta V_{LR} en_R C_L/C$. The total work done by the power source is therefore

$$W_{\text{volt}} = \frac{\Delta V_{LR} e}{C} (n_L C_R + n_R C_L). \quad (3.35)$$

Our definition of the Helmholtz energy is then

$$F = E_C - W_{\text{volt}}, \quad (3.36)$$

where E_C is the energy stored on the device due to the net charge in the island $-en$ * :

$$E_C = E_{\text{tot}} - \frac{C_L C_R \Delta V_{LR}^2}{2C} = \frac{n^2 e^2}{2C} + S(n), \quad (3.37)$$

i.e. the charging energy of an electrode of net charge $-en$ and self capacitance C (plus $S(n)$). Substituting Eqs. (3.35) and (3.37) into Eq. (3.36) yields

$$F(n_L, n_R) = \frac{n^2 e^2 - 2e \Delta V_{LR} (n_L C_R + n_R C_L)}{2C} + S(n). \quad (3.38)$$

We consider sequential tunneling, meaning that a single electron tunnels at a time. Hence, just transitions $n \rightarrow n \pm 1$ are allowed and there are four possible tunneling events, with the following variations in free energy:

$$\Delta F_L^\pm(n) = F(n_L \pm 1, n_R) - F(n_L, n_R) = \frac{e}{C} \left[\frac{e}{2} \pm (en - \Delta V_{LR} C_R) \right] + \Delta S_L^\pm(n), \quad (3.39)$$

$$\Delta F_R^\pm(n) = F(n_L, n_R \pm 1) - F(n_L, n_R) = \frac{e}{C} \left[\frac{e}{2} \pm (-en - \Delta V_{LR} C_L) \right] + \Delta S_R^\pm(n), \quad (3.40)$$

where

$$\Delta S_L^+(n) = \Delta S_R^-(n) = S(n+1) - S(n), \quad (3.41)$$

$$\Delta S_L^-(n) = \Delta S_R^+(n) = S(n-1) - S(n). \quad (3.42)$$

*In Ref. [123] the total energy stored in the device E_{tot} is considered instead of E_C . However, the variation in free energy ΔF due to the change of the net charge in the island is the same.

We will see from the expression of the tunneling rates that, for temperatures small enough compared to the absolute value of the variations in free energy $|\Delta F_{L(R)}^\pm|$, the only allowed transitions are those for which the variation in free energy is negative. This defines the Coulomb blockade of current in this system. For certain devices, as the one we will consider in Sec. 3.3.1, the capacitance of the islands may be very small, and thereby the energy drop $\Delta V_{LR} e C_{L(R)}/C$ alone may not be large enough to exceed the single-electron charging energy $E_{el} = e^2/2C$. As a result, the tunneling is halted by the Coulomb blockade. To overcome the Coulomb blockade, we can consider the addition of a gate electrode capacitively coupled to the island (switch turned on in Fig. 3.13). In this situation the island, together with the leads and the gate, form a single-electron transistor^{59,123,124}. In practice, the variations in the Helmholtz free energy for the tunneling processes from Eqs. (3.39)-(3.40) are altered, such that¹²³

$$\Delta F_L^\pm = \frac{e}{C} \left\{ \frac{e}{2} \pm [en - \Delta V_{LR} (C_R + C_g) - V_g C_g] \right\} + \Delta S_L^\pm(n), \quad (3.43)$$

$$\Delta F_R^\pm = \frac{e}{C} \left\{ \frac{e}{2} \pm [-en - \Delta V_{LR} (C_L + C_g) + V_g C_g] \right\} + \Delta S_R^\pm(n), \quad (3.44)$$

where V_g and C_g are respectively the gate voltage and capacitance, and we redefine $C \rightarrow C_L + C_R + C_g$. From Eqs. (3.43) and (3.44) it is possible to see that one can use the gate voltage to overcome the Coulomb blockade of current. There are infinitely many windows of values of V_g for which this happens, one for each value of n ^{59,123,124}

$$\frac{e \left(n + \frac{1}{2} \right) - \Delta V_{LR} (C_R + C_g) + \frac{C \Delta S_L^\pm(n)}{e}}{C_g} < V_g < \frac{e \left(n + \frac{1}{2} \right) + \Delta V_{LR} (C_L + C_g) - \frac{C \Delta S_R^\pm(n+1)}{e}}{C_g}. \quad (3.45)$$

With the help of Eqs. (3.43) and (3.44), one can see that the voltage window 3.45 is equivalent to a free energy window of width

$$\Delta V_{LR} e \left(1 + \frac{C_g}{C} \right) - \left(\Delta S_L^\pm(n) + \Delta S_R^\pm(n) \right).$$

Now we focus on the determination of the tunneling rates for the processes from Eqs. (3.39) and (3.40) (Eqs. (3.43) and (3.44)). At this point, it is important whether the island's energy spectrum is continuous or discrete, and therefore we obtain the rates for these two situations separately.

3.2.1.1 Tunneling rates for continuous energy spectrum on the island

Following the prescription of the orthodox theory of single electron tunneling⁵⁹, we write the total tunneling rate as

$$W(\Delta F) = \frac{2\pi}{\hbar} \sum_i \sum_f f_i(\epsilon_i) (1 - f_f(\epsilon_f)) |M_{f,i}|^2 \delta(\epsilon_i - \epsilon_f - \Delta F), \quad (3.46)$$

where $f_{i(f)}(\epsilon_{i(f)})$ is the Fermi-Dirac distribution (Fermi function), which gives the occupation probability of the energy levels in both electrodes. The index “i” stands for the “initial side” of the tunnel barrier, i.e. the electrode *from* which the tunneling happens, while “f” stands for “final side” of the tunnel barrier, i.e. the electrode *to*

which the tunneling occurs. Note that $1 - f_{i(f)}(\epsilon_{i(f)})$ is therefore the probability of finding an unoccupied energy level $\epsilon_{i(f)}$ on the electrode i (f). The Fermi function is given by

$$f_{i(f)}(\epsilon_{i(f)}) = \frac{1}{1 + \exp\left(\frac{\epsilon_{i(f)} - \mu_{i(f)}}{k_B T}\right)}, \quad (3.47)$$

where $\mu_{i(f)}$ is the chemical potential on the electrode i (f). The concept of density of states $D(\epsilon)$ can be used to substitute the sums in Eq. (3.46) for integrals over energy, where $D(\epsilon)d\epsilon$ is the number of states with energies lying between ϵ and $\epsilon + d\epsilon$ (not considering any degeneracies). If the temperature is small enough, the main contribution of the resulting integral from Eq. (3.46) comes from a narrow, almost rectangular tunneling window (in energy), which is defined by the product $f_i(\epsilon)(1 - f_f(\epsilon - \Delta F))$. We assume moreover that the tunnel matrix elements $M_{f,i}$ and the densities of states for the initial and final sides of the barrier $D_{i(f)}(\epsilon)$ do not appreciably depend on the energy (nor momentum) within this narrow window. Then, the delta function eliminates one of the integrations in Eq. (3.46), such that

$$W(\Delta F) = s \frac{2\pi}{\hbar} |M|^2 D_i D_f \int_{-\infty}^{\infty} d\epsilon f_i(\epsilon) (1 - f_f(\epsilon - \Delta F)). \quad (3.48)$$

We have accounted for any kind of degeneracy on the island by multiplying the right-hand side of Eq. (3.48) by s (the degeneracy on the leads are included on the density of states).

Since the tunnel junction we are considering here has an Ohmic current-voltage characteristic, which means that the current through the junction is proportional to the applied bias voltage across the junction^{*}, the phenomenological quantity “tunneling resistance” R can be introduced

$$R = \frac{\hbar}{2\pi e^2 |M|^2 D_i D_f}. \quad (3.49)$$

We assume that the tunneling resistance depends exponentially on the lead-island distance (i.e. on $\cos\theta$)

$$R_L(\theta_{A(B)}) = R_0^L e^{\xi \cos\theta_{A(B)}}, \quad (3.50)$$

$$R_R(\theta_{A(B)}) = R_0^R e^{-\xi \cos\theta_{A(B)}}, \quad (3.51)$$

where $R_0^{L(R)}$ is the tunneling resistance for the upright configuration ($\theta = \pi/2$), $\xi = \ell/\lambda$ where λ is the tunneling length, $\theta_A = \theta$ and $\theta_B = \theta + \pi$. This assumption is typically done in the context of electron shuttles^{29,30} and STMs¹⁴¹. Inserting Eq. (3.49) in Eq. (3.48), and performing the integration, we obtain the following expression for the tunneling rate

$$W(\Delta F) = s \frac{-\Delta F}{e^2 R \left[1 - \exp\left(-\frac{\Delta F}{k_B T}\right)\right]}. \quad (3.52)$$

^{*}This is not the case if the island possesses a single state participating in the transport, as we will see later on in Sec. 3.2.1.2.

Each different tunneling process is associated with a different free-energy variation (see Eqs. (3.39) and (3.40)). Therefore, each process has also a different rate

$$W_L^\pm(n_{A(B)}, \theta_{A(B)}) = s_L^\pm \frac{-\Delta F_L^\pm(n_{A(B)})}{e^2 R_L(\theta_{A(B)}) \left[1 - \exp\left(\frac{\Delta F_L^\pm(n_{A(B)})}{k_B T}\right) \right]}, \quad (3.53)$$

$$W_R^\pm(n_{A(B)}, \theta_{A(B)}) = s_R^\pm \frac{-\Delta F_R^\pm(n_{A(B)})}{e^2 R_R(\theta_{A(B)}) \left[1 - \exp\left(\frac{\Delta F_R^\pm(n_{A(B)})}{k_B T}\right) \right]} \quad (3.54)$$

where we now indicate the island (A (B)) explicitly on the argument of the free energy. Moreover, we stress that the degeneracy $s_{L(R)}^\pm$ depends on the direction of tunneling. To illustrate this we regard spin degeneracy for a system in the Coulomb blockade regime, with a gate voltage V_g tuned within the window defined by setting $n = 0$ in (3.45). In this case, tunneling events *to* the island involve two electronic states on the island. However, the island can be maximally charged by a single electron, and therefore tunneling events *from* the island just involve one electronic state on the island.

The total rates of tunneling inward and outward the island, respectively “injection” and “ejection” rates, are given by

$$W_{\text{in}}(n_{A(B)}, \theta_{A(B)}) = W_L^+(n_{A(B)}, \theta_{A(B)}) + W_R^-(n_{A(B)}, \theta_{A(B)}), \quad (3.55)$$

$$W_{\text{out}}(n_{A(B)}, \theta_{A(B)}) = W_L^-(n_{A(B)}, \theta_{A(B)}) + W_R^+(n_{A(B)}, \theta_{A(B)}). \quad (3.56)$$

Since in experiments in the Coulomb blockade regime the thermal fluctuations typically do not play a major role (they are much smaller than the free-energy variations of the system), it is instructive to look at the expressions of the tunneling rates in the limit $T \rightarrow 0$. In this limit,

$$\frac{1}{1 - \exp\left(\frac{\Delta F}{k_B T}\right)} = \begin{cases} 1 & \Delta F < 0, \\ 0 & \Delta F > 0. \end{cases}$$

This simplifies the rates from Eqs. (3.53) and (3.54) substantially. For example, let us consider the first current window obtained from setting $n = 0$ in 3.45. In this case, just two tunneling processes have $\Delta F < 0$, namely tunneling from the left lead to the island and from the island to the right lead. Therefore, the injection and ejection rates (see Eqs. (3.55) and (3.56)) can be simply expressed as

$$W_{\text{in}}(0, \theta_{A(B)}) = W_L^+(0, \theta_{A(B)}) = s_L^+ \frac{-\Delta F_L^+(0)}{e^2 R_L(\theta_{A(B)})}, \quad (3.57)$$

$$W_{\text{out}}(1, \theta_{A(B)}) = W_R^+(1, \theta_{A(B)}) = s_R^+ \frac{-\Delta F_R^+(1)}{e^2 R_R(\theta_{A(B)})}. \quad (3.58)$$

Note that the rates increase linearly with the applied voltage, as can be seen from Eqs. (3.43) and (3.44). As we will show in the following, this is not the case if the island possesses only one electronic state participating in the electronic transport.

3.2.1.2 Tunneling rates for a single energy level in the island

Due to the very small dimensions of the islands in nanodevices, the level spacing $\Delta\epsilon$ can be very large and one can select a single energy level to participate in the tunneling (if the temperature is small enough). Here we focus on deriving the tunneling rates in the case of a single energy level on the island. The situation that we consider is sketched in Fig. 3.12 (b). The only electronic state (possibly degenerate) participating in the tunneling process has energy $\epsilon_{A(B)}$. The temperature is considered to be low enough so that the energy fluctuations cannot populate other electronic levels, i.e. $k_B T \ll \Delta\epsilon$. Eq. (3.31) is again taken as valid, i.e. we calculate the tunneling rates using the golden rule of quantum mechanics (this is formally correct for a single state coupled to a continuum of states⁶³ — and this is the case that we are dealing with). Therefore, the tunneling rates between the state of energy ϵ_i within the lead and the sole state in the island are

$$W_{i \rightarrow A(B)}(\Delta F) = \frac{2\pi}{\hbar} |M_{A(B),i}|^2 \delta(\epsilon_i - \epsilon_{A(B)} - \Delta F), \quad (3.59)$$

$$W_{A(B) \rightarrow i}(\Delta F) = \frac{2\pi}{\hbar} |M_{i,A(B)}|^2 \delta(\epsilon_{A(B)} - \epsilon_i - \Delta F). \quad (3.60)$$

Note that the index A(B) in the tunnel matrix elements $M_{A(B),i}$ [$M_{i,A(B)}$] indicates tunnel to [from] the island A (B). Notice also that the concept of a “capacitance” is just well defined for bulky electrodes and may be meaningless for very small nanoparticles (or other physical system that composes the island, e.g. a molecule). In any case, the concept of free energy is still meaningful and to each tunneling event there is a correspondent free-energy variation^{*}. To obtain the total tunneling rate we need to sum over the electronic states in the lead (i) weighted by their occupation probabilities

$$W_{L(R) \rightarrow A(B)} = s \frac{2\pi}{\hbar} \sum_i f(\epsilon_i) |M_{A(B),i}|^2 \delta(\epsilon_i - \epsilon_{A(B)} - \Delta F_{L(R)}^{+(-)}(n_{A(B)} = 0)), \quad (3.61)$$

where now $f(\epsilon_i)$ is the Fermi function of the lead evaluated at energy ϵ_i . Since Coulomb blockade prevents a double occupation of the island, $n_{A(B)} = 0$ in the argument of the Helmholtz free energy. Note that the island cannot be positively charged because this would require an additional energy level participating in the electronic transport. We have accounted for any kind of degeneracy on the island by multiplying the right-hand side of Eq. (3.61) by s (we assume $M_{A(B),i}$ does not change among degenerate states). Again, using the density of states of the leads $D_i(\epsilon)$ (which may include degeneracies) we can substitute the sums in Eq. (3.61) by integrals over energy, obtaining

$$W_{L(R) \rightarrow A(B)} = s \frac{2\pi}{\hbar} D_i(\epsilon_{A(B)} + \Delta F_{L(R)}^{+(-)}(0)) f(\epsilon_{A(B)} + \Delta F_{L(R)}^{+(-)}(0)) |M_{A(B),i}|^2, \quad (3.62)$$

where the state i from $M_{A(B),i}$ has energy $\epsilon_i = \epsilon_{A(B)} + \Delta F$. The total tunneling rate from the island to the lead has an expression analogous to the one from Eq. (3.62), where we note that the factor s is now absent because just one island state is occupied

^{*}Note also that we have introduced the energy $S(n)$ in the total stored energy (Eq. (3.32)) to take some of the discrepancies between bulk electrons and very small nanoparticles formally into account.

at a time (due to the Coulomb blockade, the island is maximally singly charged)

$$W_{A(B) \rightarrow L(R)} = \frac{2\pi}{\hbar} D_i \left| M_{i,A(B)} \right|^2 \left(\epsilon_{A(B)} + \Delta F_{L(R)}^{+(-)}(1) \right) \left(1 - f \left(\epsilon_{A(B)} + \Delta F_{L(R)}^{+(-)}(1) \right) \right). \quad (3.63)$$

Now noting that the tunnel matrix elements $M_{i,A(B)}$ depend on the angle $\theta_{A(B)}$ (because it depends on the island's position), we define the function (analogous to the tunneling resistance from Eq. (3.49))

$$B_{L(R)} \left(\theta_{A(B)} \right) = \frac{\hbar}{2\pi D_i \left| M_{i,A(B)} \left(\theta_{A(B)} \right) \right|^2}, \quad (3.64)$$

where we again suppose that the density of states in the leads is constant over the energy scale of interest ($\approx e\Delta V_{LR}$). As in Sec. 3.2.1.1, we assume that the tunnel matrix elements depend exponentially on the lead-island distance (i.e. on $\cos \theta$). Therefore

$$B_L \left(\theta_{A(B)} \right) = B_0^L e^{\xi \cos \theta_{A(B)}}, \quad (3.65)$$

$$B_R \left(\theta_{A(B)} \right) = B_0^R e^{-\xi \cos \theta_{A(B)}}, \quad (3.66)$$

where $B_0^{L(R)}$ is a real constant, $\theta_A = \theta$ and $\theta_B = \theta + \pi$, and $\xi = \ell/\lambda$ where λ is the tunneling length.

If we take the limit $T \rightarrow 0$ in Eqs. (3.62) and (3.63), we obtain the rates

$$W_{L(R) \rightarrow A(B)} = s \frac{\Theta \left(\mu_{L(R)} - \epsilon_{A(B)} - \Delta F_{L(R)}^{+(-)}(0) \right)}{B_{L(R)} \left(\theta_{A(B)} \right)}, \quad (3.67)$$

$$W_{A(B) \rightarrow L(R)} = \frac{\Theta \left(-\mu_{L(R)} + \epsilon_{A(B)} + \Delta F_{L(R)}^{+(-)}(1) \right)}{B_{L(R)} \left(\theta_{A(B)} \right)}, \quad (3.68)$$

where $\Theta(x)$ is the Heaviside step function and we have used the definition of $B_{L(R)} \left(\theta_{A(B)} \right)$ from Eq. (3.64). It is clear from Eqs. (3.67) and (3.68) that the energy transport window is

$$\mu_R - \Delta F_R^+(0) < \epsilon_{A(B)} < \mu_L - \Delta F_L^+(0), \quad (3.69)$$

and within this window the injection and ejection rates, respectively the rates of total tunneling inward and outward the island, are

$$W_{\text{in}} \left(\theta_{A(B)} \right) = W_{L \rightarrow A(B)} \left(\theta_{A(B)} \right) = \frac{s}{B_L \left(\theta_{A(B)} \right)}, \quad (3.70)$$

$$W_{\text{out}} \left(\theta_{A(B)} \right) = W_{A(B) \rightarrow R} \left(\theta_{A(B)} \right) = \frac{1}{B_R \left(\theta_{A(B)} \right)}, \quad (3.71)$$

while the other rates vanish, namely the ones for tunneling from the island to L and from R to the island.

3.2.2 Mechanical equations

Herewith we regard the mechanical equations of the rotor, taking into account the model of the electronic islands presented in Sec. 3.2.1. We consider the potential energy associated to a single island to be given by

$$U_{A(B)} = E_{\text{tot}}^{A(B)} + \frac{Q_{A(B)} \Delta V_{\text{LR}}}{d_{\text{leads}}} x_{A(B)}, \quad (3.72)$$

where $E_{\text{tot}}^{A(B)}$ is the total energy stored on the island (defined by Eq. (3.32)), $x_{A(B)}$ is the projection of the position vector of island A (B) on the horizontal unit vector $\hat{\mathbf{i}}$ (see inset in Fig. 3.2), and d_{leads} is the distance between the leads. Depending on how one realizes the rotor, the island capacitances $C_{L(R)}$ may depend on the position of the island, i.e. on the angle θ . Therefore, $E_{\text{tot}}^{A(B)}$ may feature an angular dependence. We need to disregard this dependence in order to obtain the mean-field and stochastic equations of motion presented in Sec. 3.1.

In Eq. (3.72), $x_A = \ell \cos(\theta)$ and $x_B = \ell \cos(\theta + \pi) = -\ell \cos(\theta)$, where ℓ is the distance between the centers of mass of the islands and of the support shaft (“rotor arm length”), and θ is the angle between the rotor arm of the island A and the horizontal unit vector $\hat{\mathbf{i}}$ (see Fig. 3.2). The kinetic energy is

$$K_{\text{rot}} = \frac{L^2}{2I}, \quad (3.73)$$

where L is the angular momentum and I is the moment of inertia of the rotor. These considerations lead to the following classical Hamiltonian:

$$H_{\text{rot}}(\theta, L, P_A, P_B) = K_{\text{rot}} + U_A + U_B = \frac{L^2}{2I} + \ell E \cos \theta (Q_A - Q_B), \quad (3.74)$$

where $E = \Delta V_{\text{LR}}/d_{\text{leads}}$ is the magnitude of the electrostatic field \mathbf{E} . The Hamilton’s equations of motion for the Hamiltonian of Eq. (3.74) are

$$\frac{d}{dt} \theta = \frac{\partial}{\partial L} H_{\text{rot}}(\theta, L, P_A, P_B) = \frac{L}{I}, \quad (3.75)$$

$$\frac{d}{dt} L = -\frac{\partial}{\partial \theta} H_{\text{rot}}(\theta, L, P_A, P_B) = E \ell \sin \theta (Q_A - Q_B). \quad (3.76)$$

The rotor is coupled to environmental degrees of freedom, and this leads to damping and fluctuations in the angular dynamics. There are many possible dissipation channels for our rotor, depending on the physical system that is used to realize it. If one describes the dissipation via a Langevin equation (with the drift term proportional to the angular momentum), one obtains the mean-field and stochastic equations of motion presented in Sec. 3.1

$$dL = (E \ell \sin \theta (Q_A - Q_B) - \tilde{\gamma} L) dt + \sqrt{2I \tilde{\gamma} k_B T} dw, \quad (3.77)$$

$$\frac{d}{dt} \theta = \frac{L}{I}, \quad (3.78)$$

where w denotes a Wiener process and $\tilde{\gamma}$ is a phenomenological angular-viscosity parameter.

3.2.3 Deriving the stochastic equations of motion from Sec. 3.1.4

In Sec. 3.1.4 we introduced stochastic equations of motion, Eqs. (3.19)-(3.22). There, we considered that the islands are in the Coulomb blockade regime, and that they can be either discharged or charged with a single excess electron. This situation can be described within the theory presented in Sec. 3.2.1 and Sec. 3.2.2. Using a gate electrode, one can tune V_g within the window defined by the interval (3.45) in the case $n = 0$, in which case the islands can be either discharged or occupied by one electron. In this case, the charge $Q_{A(B)}$ fluctuates stochastically between 0 and $-e$. The probabilities of charge transition on the islands within the infinitesimal time $d\tau$ can be obtained through the injection and ejection rates, analogously as we did in Sec. 3.1.4. In order to derive the stochastic equations we need to show that, in some limit, the injection and ejection rates are the same as the tunneling rates defined by Eqs. (3.2) and (3.3).

Considering the temperature $T \rightarrow 0$ in Eqs. (3.57) and (3.58) for the continuous energy spectrum on the island, and in Eqs. (3.70) and (3.71) for the single-energy-level case, the nonvanishing injection and ejection rates are given by

$$W_{\text{in}}(0, \theta_{A(B)}) = W_{\text{in}}(\theta_{A(B)}) = \Gamma_L e^{-\xi \cos \theta_{A(B)}}, \quad (3.79)$$

$$W_{\text{out}}(1, \theta_{A(B)}) = W_{\text{out}}(\theta_{A(B)}) = \Gamma_R e^{\xi \cos \theta_{A(B)}} \quad (3.80)$$

where

$$\Gamma_{L(R)} = -s_{L(R)}^+ \frac{\Delta F_{L(R)}^+(n=0(1))}{e^2 R_0^{L(R)}} \quad (3.81)$$

for the case where the island has a continuous spectrum, and

$$\Gamma_L = \frac{s}{B_0^L}, \quad (3.82)$$

$$\Gamma_R = \frac{1}{B_0^R}, \quad (3.83)$$

for the case where there is just a single energy level involved in the electronic transport. Note that no tunneling from an island to the left lead or from the right lead to an island can occur because the tunneling rates for these processes are zero. As we wanted to show, the rates from Eqs. (3.79) and (3.80) have the same structure as the tunneling rates defined by Eqs. (3.2) and (3.3). Considering the symmetric case $\Gamma_L = \Gamma_R = \Gamma$ and the dimensionless quantities outlined in Tab. 3.1, one can rewrite Eqs. (3.77) and (3.78) (with $T \rightarrow 0$) in the same form as Eqs. (3.19) and (3.22). Therefore, Eqs. (3.77) and (3.78) along with the stochastic process defined by the tunneling rates from Eqs. (3.79) and (3.80) are equivalent to the Fokker-Planck equation defined by Eqs. (3.23)-(3.26), i.e. we derived the stochastic equations of motion from Sec. 3.1.4.

3.2.4 Deriving the mean-field equations of motion from Sec. 3.1.1

In Sec. 3.1.1 it was assumed that the islands are in the Coulomb blockade regime, and that moreover they can be either discharged or charged with a single excess electron. However, considering the theory presented in Sec. 3.2.1 and Sec. 3.2.2, this assumption

leads to the stochastic equations of motion introduced in Sec. 3.1.4, and not to the mean-field equations of motion presented in Sec. 3.1.1 (which Croy et al. employed to study the rotor’s dynamics in Ref. [37]).

In order to obtain the mean-field equations from the theory from Sec. 3.2.1 and Sec. 3.2.2, we need to regard the case where the islands can bear many electrons and many holes (it can also be positively charged). Therefore, we do not consider a single electronic level on the island but rather a continuum of states, as in Sec. 3.2.1.1. Moreover, we neglect the terms $S(n)$ in the definition of the free energy (Eq. (3.38)), which tend to be important for islands of very small dimensions.

The typical scale of the charge on the islands is $\Delta V_{\text{LR}}C$, and we actually mean with “many electrons/holes” that the unit of charge transfer $e \ll \Delta V_{\text{LR}}C$. It is convenient to rewrite the tunneling rates from Eqs. (3.53)-(3.54) using the dimensionless charges

$$\tilde{Q}_{\text{A(B)}} = \frac{Q_{\text{A(B)}}}{\Delta V_{\text{LR}}C}, \quad (3.84)$$

$$\Delta\tilde{Q} = \frac{e}{\Delta V_{\text{LR}}C}, \quad (3.85)$$

obtaining

$$W_{\text{L}}^{\pm}(n_{\text{A(B)}}, \theta_{\text{A(B)}}) = - \left(\frac{1}{\Delta\tilde{Q}} \right) \frac{\frac{\Delta\tilde{Q}}{2} \pm \left(-\tilde{Q}_{\text{A(B)}} - \frac{C_{\text{R}}}{C} \right)}{C R_{\text{L}}(\theta_{\text{A(B)}}) \left[1 - \exp\left(\beta_{\text{CB}} \mp \alpha \left(\tilde{Q}_{\text{A(B)}} + C_{\text{R}}/C \right)\right) \right]}, \quad (3.86)$$

$$W_{\text{R}}^{\pm}(n_{\text{A(B)}}, \theta_{\text{A(B)}}) = - \left(\frac{1}{\Delta\tilde{Q}} \right) \frac{\frac{\Delta\tilde{Q}}{2} \pm \left(\tilde{Q}_{\text{A(B)}} - \frac{C_{\text{L}}}{C} \right)}{C R_{\text{R}}(\theta_{\text{A(B)}}) \left[1 - \exp\left(\beta_{\text{CB}} \pm \alpha \left(\tilde{Q}_{\text{A(B)}} - C_{\text{L}}/C \right)\right) \right]}, \quad (3.87)$$

where we have not considered any degeneracy. If all degeneracies $s_{\text{L(R)}}^{\pm}$ are the same, Eqs. (3.86) and (3.87) are just renormalized and all the following discussion/derivation is still valid. The dependence on the temperature is summarized by the parameters

$$\alpha = \frac{\Delta V_{\text{LR}}e}{k_{\text{B}}T}, \quad (3.88)$$

$$\beta_{\text{CB}} = \frac{e^2}{Ck_{\text{B}}T}. \quad (3.89)$$

The parameters α and β_{CB} represent two different energy scales normalized by the thermal fluctuations, respectively the power-source and single-electron charging energy scales. We denote the probability density of the island A (B) being charged with $\tilde{Q}_{\text{A(B)}}$ at the time t by $\tilde{p}(\tilde{Q}_{\text{A(B)}}, t)$, and we define new tunneling rates and injection/ejection rates, respectively $\tilde{w}_{\text{L(R)}}^{\pm}(\tilde{Q}_{\text{A(B)}}, \theta_{\text{A(B)}})$ and $\tilde{w}_{\text{in/out}}(\tilde{Q}_{\text{A(B)}}, \theta_{\text{A(B)}})$, by

$$\tilde{w}_{\text{L}}^{\pm}(\tilde{Q}_{\text{A(B)}}, \theta_{\text{A(B)}}) = \Delta\tilde{Q}W_{\text{L}}^{\pm}(n_{\text{A(B)}}, \theta_{\text{A(B)}}), \quad (3.90)$$

$$\tilde{w}_{\text{R}}^{\pm}(\tilde{Q}_{\text{A(B)}}, \theta_{\text{A(B)}}) = \Delta\tilde{Q}W_{\text{R}}^{\pm}(n_{\text{A(B)}}, \theta_{\text{A(B)}}), \quad (3.91)$$

$$\tilde{w}_{\text{in}}(\tilde{Q}_{\text{A(B)}}, \theta_{\text{A(B)}}) = \Delta\tilde{Q}W_{\text{in}}(n_{\text{A(B)}}, \theta_{\text{A(B)}}), \quad (3.92)$$

$$\tilde{w}_{\text{out}}(\tilde{Q}_{\text{A(B)}}, \theta_{\text{A(B)}}) = \Delta\tilde{Q}W_{\text{out}}(n_{\text{A(B)}}, \theta_{\text{A(B)}}) \quad (3.93)$$

(note that injection and ejection rates for a continuous spectrum on the island were defined before in Eqs. (3.55) and (3.56)). If we “freeze” the mechanical degree of freedom θ , these rates define the following master equation for the probability density:

$$\begin{aligned} \frac{d}{dt} \tilde{p}(\tilde{Q}_{A(B)}, t) \Delta \tilde{Q} = & \tilde{w}_{\text{out}}(\tilde{Q}_{A(B)} - \Delta \tilde{Q}, \theta_{A(B)}) \tilde{p}(\tilde{Q}_{A(B)} - \Delta \tilde{Q}, t) + \\ & \tilde{w}_{\text{in}}(\tilde{Q}_{A(B)} + \Delta \tilde{Q}, \theta_{A(B)}) \tilde{p}(\tilde{Q}_{A(B)} + \Delta \tilde{Q}, t) - \\ & [\tilde{w}_{\text{out}}(\tilde{Q}_{A(B)}, \theta_{A(B)}) + \tilde{w}_{\text{in}}(\tilde{Q}_{A(B)}, \theta_{A(B)})] \tilde{p}(\tilde{Q}_{A(B)}, t). \end{aligned} \quad (3.94)$$

In the limit $\Delta \tilde{Q} \rightarrow 0$, Eq. (3.94) is equivalent to the Fokker-Planck equation (angle entering as a parameter)

$$\frac{d}{dt} \tilde{p}(\tilde{Q}_{A(B)}, t) = \frac{\partial}{\partial \tilde{Q}_{A(B)}} \left\{ \tilde{p}(\tilde{Q}_{A(B)}, t) [\tilde{w}_{\text{in}}(\tilde{Q}_{A(B)}, \theta_{A(B)}) - \tilde{w}_{\text{out}}(\tilde{Q}_{A(B)}, \theta_{A(B)})] \right\}. \quad (3.95)$$

This Fokker-Planck equation has no fluctuation term, and therefore it is completely equivalent to a deterministic equation for the time variation of the charge¹²²

$$\frac{d}{dt} \tilde{Q}_{A(B)}(t) = -\tilde{w}_{\text{in}}(\tilde{Q}_{A(B)}, \theta_{A(B)}) + \tilde{w}_{\text{out}}(\tilde{Q}_{A(B)}, \theta_{A(B)}). \quad (3.96)$$

One can write Eq. (3.96) explicitly as

$$\begin{aligned} \frac{d}{dt} \tilde{Q}_{A(B)}(t) = & -\frac{\tilde{Q}_{A(B)} - C_L/C}{CR_R(\theta_{A(B)})} \frac{1 - \zeta \cosh[\alpha(\tilde{Q}_{A(B)} - C_L/C)]}{(1 + \zeta^2)/2 - \zeta \cosh[\alpha(\tilde{Q}_{A(B)} - C_L/C)]} \\ & - \frac{\tilde{Q}_{A(B)} + C_R/C}{CR_L(\theta_{A(B)})} \frac{1 - \zeta \cosh[\alpha(\tilde{Q}_{A(B)} + C_R/C)]}{(1 + \zeta^2)/2 - \zeta \cosh[\alpha(\tilde{Q}_{A(B)} + C_R/C)]}, \end{aligned} \quad (3.97)$$

where $\zeta = e^{\beta_{CB}}$ and we note that all terms proportional to $\Delta \tilde{Q}$ vanish in the limit $\Delta \tilde{Q} \rightarrow 0$. It will be convenient to define the shifted (and normalized) electronic population on the islands

$$\tilde{P}_{A(B)} = -\left(\tilde{Q}_{A(B)} - \frac{C_L}{C}\right). \quad (3.98)$$

With this definition, one can rewrite Eq. (3.97) as

$$\begin{aligned} \frac{d}{dt} \tilde{P}_{A(B)}(t) = & (1 - \tilde{P}_{A(B)}(t)) \frac{1 - \zeta \cosh[\alpha(1 - \tilde{P}_{A(B)}(t))]}{(1 + \zeta^2)/2 - \zeta \cosh[\alpha(1 - \tilde{P}_{A(B)}(t))]} \tilde{w}_L(\theta_{A(B)}) \\ & - \tilde{P}_{A(B)}(t) \frac{1 - \zeta \cosh(-\alpha \tilde{P}_{A(B)}(t))}{(1 + \zeta^2)/2 - \zeta \cosh(-\alpha \tilde{P}_{A(B)}(t))} \tilde{w}_R(\theta_{A(B)}), \end{aligned} \quad (3.99)$$

where

$$\tilde{w}_{L(R)}(\theta_{A(B)}) = \frac{1}{CR_{L(R)}(\theta_{A(B)})}. \quad (3.100)$$

From Eqs. (3.98) and (3.99) one sees that the charge $Q_{A(B)}$ on the island can vary between two well-defined values Q_{\min} and Q_{\max} :

$$-\Delta V_{LR}C_R < Q_{A(B)} < \Delta V_{LR}C_L. \quad (3.101)$$

This sums up to a total variation $Q_{\max} - Q_{\min} = Q_{\text{var}} = \Delta V_{LR}C$. An additional gate electrode changes $C_R \rightarrow C_R + C_g(1 + V_g/\Delta V_{LR})$ and $C_L \rightarrow C_L + C_g(1 - V_g/\Delta V_{LR})$ in Eq. (3.101). Considering the new island capacitance $C \rightarrow C_L + C_R + C_g$, the total variation is $Q_{\text{var}} = \Delta V_{LR}C + C_g\Delta V_{LR}$. Moreover, the charge is shifted by $-V_gC_g$. A detailed derivation for the case with the gate electrode is given in Appendix B.

Note that although Eq. (3.99) is a deterministic equation of motion for the charge, it is not identical to the mean-field Eq. (3.4) from Sec. 3.1.1. We will see that the mean-field equation for the charge emerges from Eq. (3.99) in two limiting cases of the parameters β_{CB} and α .

$\beta_{CB} \gg 1$ **alone**

The parameter β_{CB} is the ratio of the single-electron charging energy scale $E_{el} = e^2/2C$ to the thermal energy $k_B T$. α is a ratio of the scale of the energy supplied by the power source to tunneling electrons $\Delta V_{LR}e$ to $k_B T$. Therefore, if β_{CB} is much larger than 1 while α is not, $E_{el}/\Delta V_{LR}e \gg 1$, i.e. the bias ΔV_{LR} is not large enough to overcome the Coulomb blockade. Consequently, all tunneling rates go to zero.

$\beta_{CB} \gg 1$ **and** $\alpha \gg 1$

Substituting in Eq. (3.99) one obtains

$$\begin{aligned} \frac{d}{dt}\tilde{P}_{A(B)}(t) &= \left(1 - \tilde{P}_{A(B)}(t)\right) \frac{\cosh\left[\alpha\left(1 - \tilde{P}_{A(B)}(t)\right)\right]}{\zeta/2 - \cosh\left[\alpha\left(1 - \tilde{P}_{A(B)}(t)\right)\right]} \tilde{w}_L\left(\theta_{A(B)}\right) \\ &\quad - \tilde{P}_{A(B)}(t) \frac{\cosh\left(-\alpha\tilde{P}_{A(B)}(t)\right)}{\zeta/2 - \cosh\left(-\alpha\tilde{P}_{A(B)}(t)\right)} \tilde{w}_R\left(\theta_{A(B)}\right). \end{aligned} \quad (3.102)$$

$\alpha \gg 1$ **alone**

In this case the energy supplied by the power source to tunneling electrons is much larger than other energy scales in the system. All thermal effects are washed out, and by substitution in Eq. (3.97) one obtains

$$\frac{d}{dt}\tilde{P}_{A(B)}(t) = \left(1 - \tilde{P}_{A(B)}(t)\right) \tilde{w}_L\left(\theta_{A(B)}\right) - \tilde{P}_{A(B)}(t) \tilde{w}_R\left(\theta_{A(B)}\right). \quad (3.103)$$

Cases where $\alpha \ll 1$

In these cases the bias is practically zero and, since there are no charge fluctuations, all the tunneling rates go to zero as well.

$\beta_{\text{CB}} \ll 1$ alone

In this case one is far away of the Coulomb blockade regime. Substitution in in Eq. (3.97) yields

$$\frac{d}{dt} \tilde{P}_{\text{A(B)}}(t) = \left(1 - \tilde{P}_{\text{A(B)}}(t)\right) \tilde{w}_{\text{L}}(\theta_{\text{A(B)}}) - \tilde{P}_{\text{A(B)}}(t) \tilde{w}_{\text{R}}(\theta_{\text{A(B)}}). \quad (3.104)$$

It should be noted that this equation is the same as Eq. (3.103) from the case where $\alpha \gg 1$ alone.

In the cases $\beta_{\text{CB}} \ll 1$ alone and $\alpha \gg 1$ alone we can obtain the mean-field equation of motion for the charge Eq. (3.4). If we define

$$\Gamma_{\text{L(R)}} = \frac{1}{CR_0^{\text{L(R)}}} \quad (3.105)$$

the tunneling rates from Eq. (3.100) can be simply written as

$$\tilde{w}_{\text{L}}(\theta_{\text{A(B)}}) = \Gamma_{\text{L}} e^{-\xi \cos \theta_{\text{A(B)}}}, \quad (3.106)$$

$$\tilde{w}_{\text{R}}(\theta_{\text{A(B)}}) = \Gamma_{\text{R}} e^{\xi \cos \theta_{\text{A(B)}}}. \quad (3.107)$$

If $\Gamma_{\text{L(R),A}} = \Gamma_{\text{L(R),B}}$ and $\xi_{\text{L(R),A}} = \xi_{\text{L(R),B}}$ in Eq. (3.4), this equation is the same as Eq. (3.103) (Eq. (3.104)). In most part of Sec. 3.1.1 we considered the symmetric case $\Gamma_{\text{R}} = \Gamma_{\text{L}} = \Gamma$, which can also be considered here.

To obtain the mechanical part of the mean-field equations of motion we first note that $Q_{\text{A}} - Q_{\text{B}} = (\tilde{P}_{\text{B}} - \tilde{P}_{\text{A}}) \Delta V_{\text{LR}} C$, and therefore Eq. (3.77) depends just on the difference between the populations $\tilde{P}_{\text{B}} - \tilde{P}_{\text{A}}$, analogously to Eq. (3.9). In the limit $T \rightarrow 0$ and with the definition of dimensionless quantities from Tab. 3.2, Eq. (3.77), Eq. (3.78), and Eq. (3.103) are equivalent to Eqs. (3.8)-(3.10). In other words, we have obtained the mean-field equations of motion from Sec. 3.1.1. In Appendix C we derive the mechanical equations of motion in detail for the more general case where the rotor's arms are tilted by an arbitrary angle β .

3.2.5 Conclusions

In Sec. 3.2 we used the orthodox theory of single-electron tunneling⁵⁹ to derive the stochastic and mean-field equations of motion from Sec. 3.1. While to derive the stochastic equations we needed to go to a “single-electron limit” (with the help of a gate electrode), where the islands can be either discharged or charged with a single excess electron; to derive the mean-field equations of motion we needed to go to a “continuous-charging limit”, where the scale of the charge on the islands is much larger than the unit of charge transfer e . In both cases, we needed to neglect thermal fluctuations both in the mechanical and in the charge equations of motion. Also the angular dependence of the capacitances was neglected. However, we have accounted for the discreteness of the energy spectrum in the single-electron limit case by obtaining tunneling rates for a single energy level on the island's spectrum.

The derivation of the mean-field and stochastic equations provided a clear set of assumptions for both models. However, we cannot assess whether these assumptions

Table 3.2: Dimensionless quantities used in the mean-field equations derived in Sec. 3.2.4 and their definitions.

Quantity	Symbol	Formula
Time	τ	Γt
Charge (population)	$\tilde{P}_{A(B)}$	$-\frac{Q_{A(B)}}{\Delta V_{LR} C} + \frac{C_L}{C}$
Angular momentum	Λ	$\frac{L}{\Gamma I}$
Driving strength	η_0	$\ell \left[\frac{Q_{\text{var}} E}{\Gamma^2 I} \right]$
Viscosity parameter	γ	$\frac{\tilde{\gamma}}{\Gamma}$

hold if we do not concretize the rotor model into an experimental proposal. Such a proposal also makes it possible to estimate the ranges of parameter values which can be accessed. In the next section, we propose two different devices, each of which is suited to one of the limits described here.

3.3 Experimental realization

In Sec. 3.1.1 we showcased the dynamics of the mean-field and stochastic models. These models show interesting dynamics which can be used to obtain certain functionalities (e.g. the rotor can work as a nanoswitch or electron pump). However, the dynamics of the mean-field and stochastic models disagree in certain parameter regimes, in particular for large damping. This discrepancy prompted us to derive these models from the theory of single electron tunneling in the previous section. Now we have a clear set of assumptions for these two models, and in this section we are aimed at proposing experimental devices for which these assumptions hold. Such devices will also allow us to estimate parameter ranges which can be accessed in an experimental situation.

We propose two devices, one for each set of equations. We estimate the parameters one can realize considering these two proposals. Clearly, all the elements composing the rotor, e.g. electronic islands, support shaft, etc. can be designed in a completely different way (we will briefly discuss some of these ways). However, these proposals allow us to base our estimates on physical systems (metallic nanoparticles, multi-walled carbon nanotubes, etc.) for which one can find plenty of experimental data in the literature. Moreover, with these proposals we show that the rotor can be fabricated with present-day technology. We stress though that the estimates we do are very rough and just have two purposes: giving an idea of the dimensions and materials that can be used to build these devices, and discussing some of the possible challenges involved.

The connection between device and set of equations is established through the theory presented in the previous section. The most critical assumptions made in Sec. 3.2 are discussed based on the devices proposed here.

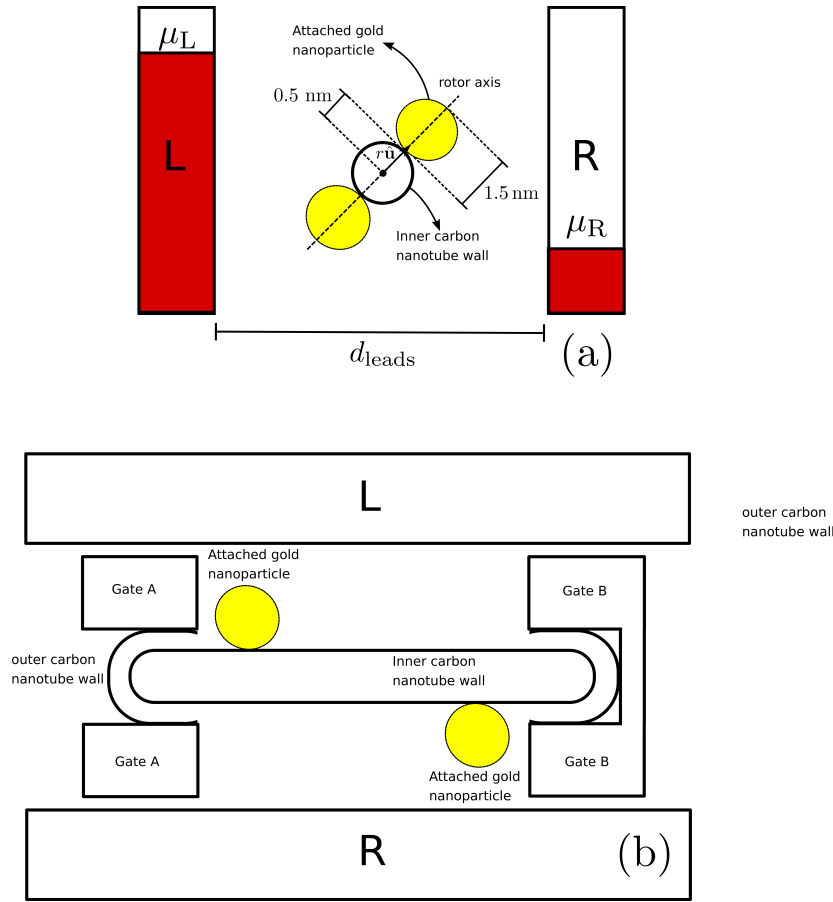


Figure 3.14: Sketch of the device proposed to realize the stochastic equations of motion. (a) and (b) represent two different perspectives of the same device.

3.3.1 Single-electron limit: stochastic equations of motion

As we have seen in Sec. 3.2.3, the stochastic equations of motion are obtained in a “single-electron limit” where the islands can be either discharged or charged with a single excess electron. A sketch of a possible experimental realization of this limit can be seen in Fig. 3.14. We consider a rotor composed of a carbon nanotube (support shaft) decorated with two Au nanoparticles (electronic islands) flanked by two leads. The Au nanoparticles are deposited on opposite sides of the carbon nanotube, so that their centers of mass and the nanotube’s axis are aligned. To avoid electronic coupling between them, the nanoparticles are further separated in the nanotube’s longitudinal direction (see Fig. 3.14 (b)). Such arrangement of Au nanoparticles deposited on opposite sides of a carbon nanotube can be experimentally achieved with present-day technology, using dip-pen nanolithography^{56,57}. This technique allows the site-specific deposition of Au nanoparticles without the introduction of any structural modification to the carbon nanotube*. Site-specific functionalization of carbon nanotubes with molecules (substituting the Au nanoparticles as electronic islands) is also possible via focused

*Single-electron tunneling in a system where a Au-nanoparticle electronic island is attached to the outer wall of a carbon nanotube was already achieved experimentally in the context of single-electron memories¹²⁵.

ion beam irradiation¹²⁶, but it is not suitable for non-destructive modification of the nanotube^{56,57} * . The support shaft is the inner wall of a multi-walled carbon nanotube whose outer walls were removed using the electrical-breakdown technique^{128,129}. The width of the carbon nanotube can be tailored with precision of a few angstroms using this technique. Moreover, the multi-walled-nanotube conductance can be tuned down to zero¹²⁸. Such a bearing was already realized experimentally for a nanorotor⁴ † . Bearings based on multi-walled carbon nanotubes lead to a friction coefficient which is proportional to the angular velocity, if the velocity is small enough ‡³. Moreover, engineering of this friction coefficient is possible due to its dependence on the temperature and interlayer spacing §³. In particular, the friction of this kind of bearings can be very low³⁻⁵, and therefore it imposes a fundamental limit on the friction coefficients that are obtainable. We will discuss the timescale of this mechanical relaxation channel in Sec. 3.3.3.3 ¶ . Additional friction can arise from the electronic coupling to the “image-charges” on the leads¹³¹ and from coupling to a surrounding gas. The former friction coefficient will be estimated in Sec. 3.3.3.3 (the second one can be controlled or even avoided e.g. by performing experiments in high-vacuum). Moreover, light emission from the accelerated charge on the island can also (in principle) damp the rotations. We will show that this effect is negligible for our setup in Appendix A. We note that one can engineer a nanoscale rotor in other ways, e.g. considering molecules with rotating parts^{15,16,132-134}, or replacing the metallic nanoparticles by quantum dots, molecules, etc. The above realization was chosen for the availability of experimental data on carbon nanotubes and gold nanoparticles, and because it allows for simple estimates.

This device can be designed such that the islands are in the Coulomb blockade regime. One can show this via a simple estimate of the island charging energy. The boundary between molecule-like and bulk-like charging of nanoparticles is not very clear¹³⁵, but it appears to start in particles of diameters between 1 nm and 2 nm¹³⁵⁻¹³⁷. To estimate the charging energy of the islands we perform a simple bulk estimation of their self capacitance considering a spheric geometry. Note that even if the island is so small that the bulk estimate is wrong¹³⁷ (or if the geometry deviates from a sphere), it should at least get the correct order of magnitude of the charging energy. Considering gold islands of diameter 1.5 nm, our estimate gives

$$C_{A(B)} \approx 4\pi\epsilon_0 r_{A(B)} \approx 0.5 \text{ e/V}, \quad (3.108)$$

where ϵ_0 is the electrostatic permittivity of vacuum and $r_{A(B)} = 0.75 \text{ nm}$ is the radius of the islands. Therefore, we obtain a single-electron charging energy $E_{\text{el}}^{A(B)} \approx e^2/2C_{A(B)} \approx 1.9 \text{ eV}$. This gives the scale of the energy-level splitting for different occupation numbers

*If strict control of the modification position is not needed, there is a large experimental freedom on the type of the deposited particles^{57,127}.

†A slightly different bearing where the outer wall rotates while the inner one is kept stationary is also possible⁵.

‡In Ref. [3] it was shown that the friction coefficient is proportional to the angular velocity at least up to angular velocities of approximately 1 rad/ps^{-1} . As we show in Sec. 3.3.3.2, the timescale of our system’s dynamics is in the nanosecond regime.

§The presence of impurities, defects, and deformations leads to an enhancement of the friction coefficient³.

¶Another advantage of multiwall-carbon-nanotube-based bearings is their (presumably perfect) wear and fatigue resistance^{5,130}.

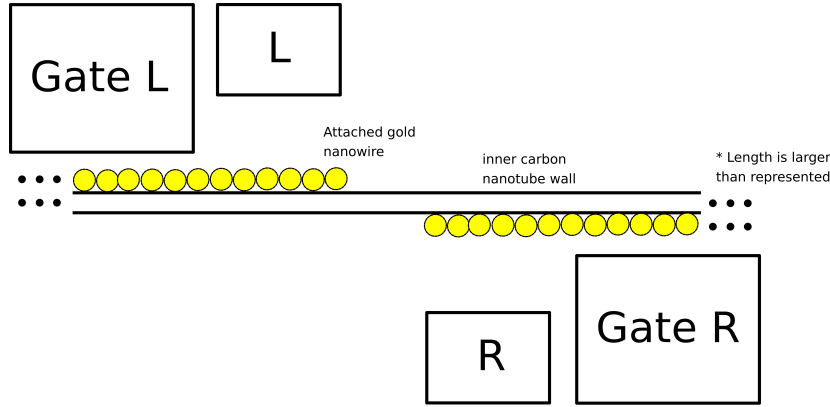


Figure 3.15: Sketch of a possible realization of the rotor for the continuous charging limit. The inner carbon nanotube is supported by the ends of the outer tube (not represented). For better visualization, just part of the inner tube and the nanowires (islands) is represented.

on the island. For comparison, the thermal energy at room temperature is in the scale of meV. In order to overcome the single-electron charging energy with the bias, one can couple the islands capacitively to gate electrodes of voltage V_g and capacitance C_g , as in a single-electron transistor^{59,123}. By tuning V_g within the window obtained by substituting $n = 0$ in the interval (3.45), the islands can be either discharged or charged with a single excess electron. The coupling to a gate electrode can also cure unpredictable behavior due to the presence of background charges^{59,123}. This electrode should interact with the island in the same way for all angles θ . An idea on how it could be accomplished is using the outer wall of the nanotube as a support for a ring-shaped gate electrode (see Fig. 3.14 (b)). Finally, additional electrodes can be used to control of the magnitude of electrostatic field driving rotations.

With that we showed that the single-electron limit can be realized experimentally using present-day technology. This indicates that the dynamics of such a device are described by the stochastic equations of motion. However, we still need to check whether the assumptions made when deriving these equations in Sec. 3.2 hold for this device. This will be done in Sec. 3.3.4. Before that, in Sec. 3.3.3, we will estimate de ranges of parameter values which can be achieved.

3.3.2 Continuous-charging limit: mean-field equations of motion

We showed in Sec. 3.2.4 that the mean-field equations of motion can be obtained in a “continuous-charging limit” where the absolute charge on the islands, of scale $C\Delta V_{LR}$, is always much larger the unit of charge transfer e . Additionally, the bias energy $\Delta V_{LR}e$ must be much larger than the single-electron charging energy $E_{el}^{A(B)} = e^2/2C_{A(B)}$ (bulk limit). A sketch of a possible experimental realization for this limit can be seen in Fig. 3.15. The main difference in design between this realization and the one from Sec. 3.3.1 is that now the islands are composed of gold nanowires instead of a *single* nanoparticle. This nanowire can be formed by juxtaposition of gold nanoparticles, such that the electronic wave function is delocalized across the wire¹³⁸. The formation of a polycrystalline wire can be achieved e.g. by heating up the deposited nanoparticles, similarly as in Ref. [139]. For being larger than a single nanoparticle, the wire has also

a larger capacitance. This capacitance is also scalable: one can in principle attain a desired capacitance by building a wire with the corresponding length. The maximum charge stored by the nanowire island is $Q_0 \approx C_{A(B)}\Delta V_{LR}$ (without gate electrodes). By extending the longitudinal dimension of the nanowire into the micrometer scale one eventually reaches the continuous-charging limit. The device proposed here includes gate electrodes, as the device from Sec. 3.3.1. The gate electrodes can control the maximal absolute value of the charge that the islands can bear. As in Sec. 3.3.1, additional electrodes can be used to control the magnitude of the electrostatic field driving rotations.

In order to get a feeling for the physical numbers, let us consider a $20\ \mu\text{m}$ long support shaft of a diameter of $1\ \text{nm}$. The islands composing the nanowire have a diameter of $1.5\ \text{nm}$. The capacitance of such a device can be estimated considering the self capacitance of a bulky gold wire¹⁴⁰:

$$C_{\text{wire}} = \frac{2\pi\epsilon_0 l}{\Xi} \left\{ 1 + \frac{1}{\Xi} (1 - \ln 2) + \frac{1}{\Xi^2} \left[1 + (1 - \ln 2)^2 - \frac{\pi^2}{12} \right] + O\left(\frac{1}{\Xi^3}\right) \right\}, \quad (3.109)$$

where $\Xi = \ln(l/a)$, l is the wire length, and a is the wire radius. Plugging in $l = 10\ \mu\text{m}$, $a = 0.75\ \text{nm}$, and considering the expansion up to second order yields a capacitance of

$$C_{A(B)} \approx 380\ e/V, \quad (3.110)$$

which is equivalent to a single-electron charging energy of $E_{\text{el}}^{A(B)} \approx e^2/2C_{A(B)} \approx 1\ \text{meV}$. As an example, let us consider the temperature for which $k_B T = 5\ \text{meV}$. This is $T \approx 58\ \text{K}$, showing that we are no longer in the Coulomb blockade regime even for temperatures much lower than the room temperature. If the gate electrodes are all turned off, the maximum charge on the island is approximately

$$C_{A(B)}\Delta V_{LR} \approx 38\ e. \quad (3.111)$$

As we mentioned before, one can change this charge (and the driving electrostatic field) through gate electrodes.

With that we showed that the continuous-charging limit can be realized experimentally using present-day technology. Moreover, this device allows us to go all the way from the single-electron to the continuous-charging limit. This is possible because we can extend the electronic islands along the dimension which is not directly involved in the rotor's dynamics. Indeed, in the continuous-charging limit this device has two dimensions sized in the nanoscale and one in the microscale. In order to show that the mean-field equations describe the dynamics of this device, we need to check whether the assumptions made when deriving these equations in Sec. 3.2 hold. This will be done in Sec. 3.3.4. Before that, in Sec. 3.3.3, we will estimate de ranges of parameter values which can be achieved.

3.3.3 Dimensionless parameters from the stochastic and mean-field models

The three dimensionless parameters present in the stochastic and in the mean-field equations of motion are the inverse tunneling length ξ , the driving strength η_0 , and the angular viscosity γ . Herewith we analyze which ranges of these parameters are obtainable in the devices proposed in Sec. 3.3.1 and Sec. 3.3.2.

3.3.3.1 Inverse tunneling length ξ

For the devices from both Sec. 3.3.1 and Sec. 3.3.2, the inverse tunneling length is defined as

$$\xi = \frac{\ell}{\lambda}, \quad (3.112)$$

where ℓ is the “arm length”, i.e. the distance between the island’s center of mass and the axis of rotation, and λ is the tunneling length, which characterizes the scale at which tunneling occurs. In principle, ℓ can be as small as ≈ 1 nm (pushing the nanotube’s and the nanoparticle’s diameters to the extreme). The tunneling length depends on the tunnel barrier. In the context of STMs, the probability for an electron in the sample state ψ_n to present at the tip surface, at a distance $x = d$ from the sample, is proportional to $|\psi_n(x = 0)|^2 e^{-2kd}$ ($x = 0$ is at the sample’s surface)¹⁴¹. Here, $k = \sqrt{2m_{\text{el}}\phi_{\text{bar}}}/\hbar$, ϕ_{bar} is the height of the tunnel barrier, and m_{el} is the electronic mass. The tunneling length in this context is given by

$$\lambda = \frac{1}{2k} = \frac{\hbar}{2\sqrt{2m_{\text{el}}\phi_{\text{bar}}}}. \quad (3.113)$$

The tunnel-barrier value $\phi_{\text{bar}} = 1$ eV can be easily encountered in the literature, e.g. in scanning tunneling microscope (STM) experiments^{141,142}; and it is shown to be reproducible and to persist at least over a tip-sample distance variation of some angstroms. In Ref. [142], tunnel-barrier values as small as $\phi_{\text{bar}} = 0.01$ eV were also reported. Plugging the electronic mass and the tunnel-barrier value $\phi_{\text{bar}} = 1$ eV in Eq. (3.113) one obtains $\lambda \approx 0.98$ Å, which leads to ξ in the order of 10. If one uses $\phi_{\text{bar}} = 0.01$ eV instead one gets ξ in the order of 1 (which is the scale that we have explored in Sec. 3.1).

3.3.3.2 Driving strength η_0

In the single-electron limit, the driving strength is defined as

$$\eta_0 = \frac{eE\ell}{I\Gamma^2}, \quad (3.114)$$

where e is the elementary charge, E is the magnitude of the driving electrostatic field \mathbf{E} , I is the moment of inertia of the rotor, and Γ is the tunneling rate for the rotor at upright configuration ($\theta = \pi/2$). In the continuous-charging limit η_0 is defined as

$$\eta_0 = \frac{Q_{\text{var}}E\ell}{I\Gamma^2}, \quad (3.115)$$

where Q_{var} is the maximal variation of the charge on the islands (see the discussion in Sec. 3.2.4). Via additional electrodes, it is in principle possible to engineer the driving electrostatic field E independently of the bias voltage ΔV_{LR} and the distance between the leads d_{leads} . This may be an engineering challenge, but one can achieve control of electrostatic fields in the nanoscale with the present technology. For example, in Ref. [58] two 4 nm long quantum dots distant 10 nm apart could be electrostatically controlled independently. However, also the magnitude of the electrostatic field is limited: if it is too large, the chemical bonds which keep the rotor together may be

broken. Typical magnitudes required to break chemical bonds are in the scale of 1 V/nm (see e.g.¹⁴³). Therefore, we consider that a maximum $E = 0.1$ V/nm can be safely achieved experimentally considering the devices we have proposed.

The parameter Γ gives the timescale of tunneling. In the following, we focus our discussion on the device from Sec. 3.3.1. in Ref. [144] the tunneling current through gold nanoparticles between an STM tip and a gold surface was measured. The nanoparticles were ligand-stabilized (hexanethiolate), and therefore they were larger than their gold core. One of the nanoparticles used had a diameter of 3.2 nm, which is equivalent to an estimated core diameter of 1.8 nm. Moreover, there was a monolayer of hexanethiol over the gold surface. Although the authors do not say how long these molecules are, they estimate the length of hexanethiolate to be 0.77 nm*. If we consider that the hexanethiol monolayer contributed with 0.5 nm (the molecules are not perpendicularly oriented with respect to the surface and the geometry is not given), the minimum distance between the gold surface and the nanoparticle's center of mass was 2.1 nm. The currents obtained in this experiment (for a voltage large enough to overcome the Coulomb blockade) were in the nA scale — note that 1 nA is equivalent to 6.25 electrons per nanosecond. This result can be used to estimate Γ : let $d_{\text{leads}} = 4.2$ nm, the lead-island distance at $\theta = \pi/2$ is 2.1 nm, and therefore $\Gamma \approx 6$ ns⁻¹ is an estimate consistent with the experiment from¹⁴⁴. Note that this value can be easily tuned down by making d_{leads} larger.

In theory, one has complete control over the driving strength, because one can decrease both Γ and E at will. However, the angular viscosity γ also depends (although not quadratically) on Γ , such that, in practice, these parameters cannot be unlimitedly tuned independently. For this reason, it is important to check what is the range of η_0 that can be varied using E only. Let us consider a 5 nm long support shaft of diameter 1 nm, and islands of diameter 1.5 nm. In order to calculate I we have considered bulky gold spheres and we have used¹⁴⁵ for the nanotube, obtaining $I \approx 100$ zg nm². Considering maximal $E = 0.1$ V/nm, $\Gamma = 6$ ns⁻¹, and $\ell = 1.25$ nm, we obtain $\eta_0 \approx 5$. Again, one can make this value larger by tuning Γ down. But in this case one needs to take into account the changes in γ .

For the device proposed in Sec. 3.3.2 we expect one to be able to achieve larger values of Γ , since now many gold nanoparticles are involved in the charge transport. Moreover, using gate electrodes one can also control the charge variation Q_{var} (see Sec. 3.2.4). However, the minimal moment of inertia I must be inevitably larger (which could be compensated e.g. with the larger absolute charge on the islands). Since for this device one has more parameters to control η_0 than in the device from Sec. 3.3.1, we also expect that a larger range of η_0 is attainable.

3.3.3.3 Dimensionless angular viscosity γ

The dimensionless angular viscosity, which we have often called “angular viscosity” or even simply “viscosity” within this thesis, is given by

$$\gamma = \frac{\tilde{\gamma}}{\Gamma}, \quad (3.116)$$

*The only structural difference of hexanethiolate compared to hexanethiol is the absence of an hydrogen atom bound to the S atom at the end of the chain.

where $\tilde{\gamma}$ is the “physical viscosity”, which has dimension of one over time. This definition is valid for the devices from Sec. 3.3.1 and Sec. 3.3.2. Notice that the dimensionless angular viscosity depends on Γ , which was already discussed in Sec. 3.3.3.2. This viscosity comes from coupling to different types of environmental degrees of freedom. These different types lead to different damping channels. Herewith we consider three damping channels:

- 1) The friction arising from the interaction between the walls of the double-walled carbon nanotube which constitutes the support shaft;
- 2) The mechanical damping arising from the coupling of the charge on the island with the image charge on the leads;
- 3) The mechanical damping arising from the coupling between the rotating charges on the islands and the electromagnetic field.

These damping channels lead to the dimensionless angular viscosity

$$\gamma = \gamma_{\text{bear}} + \gamma_{\text{im}} + \gamma_{\text{light}}, \quad (3.117)$$

where γ_{bear} , γ_{im} , and γ_{light} are the dimensionless angular friction “coefficients” from 1), 2), and 3) respectively. Actually, these “coefficients” may depend on the dynamical variables as well: we will see that 2) leads to an anisotropic damping coefficient and 3) does not lead to dissipation proportional to the first power of the angular momentum.

While we show in Appendix A that 3) can be neglected, we discuss the more important 1) and 2) here. In Ref. [3] the timescale of 1) for double-walled carbon nanotubes (4,4)@(9,9) * and (7,0)@(9,9) was determined to be in the nanosecond regime. Although we cannot directly use these results because the armchair configuration is conducting, we still expect the lower bound for the damping timescale in our system to lie in the nanosecond regime. Taking into account the value $\Gamma \approx 6 \text{ ns}^{-1}$ considered in Sec. 3.3.3.2 (device from Sec. 3.3.1), this suggests that obtaining $\gamma_{\text{bear}} \geq 1$ may be easy, and possibly one can reach $\gamma_{\text{bear}} \approx 0.1$. As mentioned before, for the device from Sec. 3.3.2 we expect one being able to achieve larger values of Γ , and thereby having more freedom in tuning γ_{bear} .

If the leads are metallic, the channel 2) represents a challenge for the devices proposed in Sec. 3.3.1 and Sec. 3.3.2. In first order with respect to the velocity of the island \mathbf{v}_{isl} , this channel leads to a force $-\mathbf{\Gamma}_{\text{im}}\mathbf{v}_{\text{isl}}$, where

$$\mathbf{\Gamma}_{\text{im}} = 2\Gamma_{\text{im}}\hat{\mathbf{i}} + \Gamma_{\text{im}}\hat{\mathbf{j}} + \Gamma_{\text{im}}\hat{\mathbf{k}} \quad (3.118)$$

is the (anisotropic) linear friction coefficient (for a definition of the unit vectors $\hat{\mathbf{i}}$, $\hat{\mathbf{j}}$, and $\hat{\mathbf{k}}$ see the inset in Fig. 3.2). As one can see from the expression for $\mathbf{\Gamma}_{\text{im}}$, the friction is twice stronger when the charged island is moving towards one of the leads (direction $\pm\hat{\mathbf{i}}$). Now we focus on the device from Sec. 3.3.1 and, in the end, we comment on

*The way the graphene sheet is wrapped to form a single-walled nanotube is represented by a pair of indices (n, m) . The integers n and m denote the number of unit vectors along two directions in the honeycomb crystal lattice of graphene. Since a double-walled nanobube is formed by two single-walled nanotubes, one needs two pairs of integers to describe them, e.g. (4,4)@(9,9).

the differences we expect for the device from Sec. 3.3.2. This friction coefficient was estimated in Ref. [131] (for the case of a single metallic surface) to be *

$$\Gamma_{\text{im}} = \sqrt{\frac{\epsilon}{4\pi}} \frac{e}{4\sigma_{\text{cond}} d^3}, \quad (3.119)$$

where ϵ is the electric permittivity of the medium (which we consider to be vacuum in our estimate, i.e. $\epsilon = \epsilon_0$), σ_{cond} is the conductivity of the leads, and d is the distance between the island and the lead. The linear friction coefficient from Eq. (3.119) can be transformed into the dimensionless angular friction coefficient:

$$\gamma_{\text{im}} = \frac{\Gamma_{\text{im}} \ell}{\Gamma I}. \quad (3.120)$$

Now we estimate γ_{im} considering $d_{\text{leads}} = 4.2 \text{ nm}$, which leads to $\Gamma \approx 6 \text{ ns}^{-1}$ (based on the experiment from¹⁴⁴). As in the discussion of the driving strength, let us consider a 5 nm long support shaft of diameter 1 nm, and gold islands of diameter 1.5 nm, leading to $\ell = 1.25 \text{ nm}$ and $I \approx 100 \text{ zg nm}^2$. For metals at a temperature $T \approx 50 \text{ K}$, $\sigma_{\text{cond}} \approx 10^8 \text{ S/m}$. As for the lead-island distance we simply consider 1 nm in our estimate. Substituting these values in Eq. (3.120) we obtain $\gamma_{\text{im}} = 2.2 \times 10^{15}$! Through cooling the system down to temperatures $T \approx 1 \text{ K}$ one gets σ_{cond} one order of magnitude larger. Supposing that the moment of inertia I can be changed at will (by using a longer nanotube and attaching heavy objects to it), one can in principle decrease γ_{im} . To decrease γ_{im} by a factor 10^{15} one needs to increase I by the same factor. For comparison, this moment of inertia would correspond to a solid gold particle whose radius is $\approx 1.3 \mu\text{m}$. However, this would make the driving be too small, and one would need to change Γ , which inevitably changes γ_{im} . Since η_0 depends quadratically on Γ , one may be able to obtain ratios η_0/γ as we have used in the simulations from Sec. 3.1, but it would be very difficult to realize the same values of γ .

A somewhat more elegant workaround is to replace superconducting electrodes for the metallic leads (and possibly islands). For all superconductive electrodes, if the Josephson coupling energies $\dagger E_j \ll E_C$ (single-electron charging energy $E_C = e^2/2C$), then the Josephson effects are suppressed^{146,147} and one can describe the system approximately with the theory we presented in Sec. 3.2. We note that considering the Josephson effects can bring about new physics: e.g. the charge carriers in the superconductive case are Cooper pairs and quasiparticles, and one needs to account for the superconducting energy gap 2Δ . Considering normal metal islands and superconducting leads can also lead to new phenomena, as the Andreev current^{148,149}. If these effects cannot be neglected, the theory presented in Sec. 3.2 does not describe the dynamics of the rotor.

Finally, notice that in the device from Sec. 3.3.2 one has to substitute the larger island's charge $Q_{\text{A(B)}}(t)$ for e in Eq. (3.119). The scale of $Q_{\text{A(B)}}(t)$ is given by $Q_{\text{var}} = n_{\text{cont}} e$, where n_{cont} is a positive integer. To keep the same η_0 , ξ , and Γ , $I_{\text{cont}} = n_{\text{cont}} I_{\text{sing}}$, where I_{sing} and I_{cont} are the moment of inertia of the devices from respectively Sec. 3.3.1 and Sec. 3.3.2. This means that the scale of the dimensionless angular friction coefficient defined by Eq. (3.120) is expected to be approximately the same for both devices.

*Note that we have transformed the equations in Ref. [131] from cgs to SI units.

[†]The Josephson coupling energy is $E_j = \hbar I_S / 2e$, where I_S is the maximal supercurrent. Typically, the tunnel resistance R is large enough so that $I_S = \pi 2\Delta / 4R$, where 2Δ is the superconducting gap¹⁴⁶.

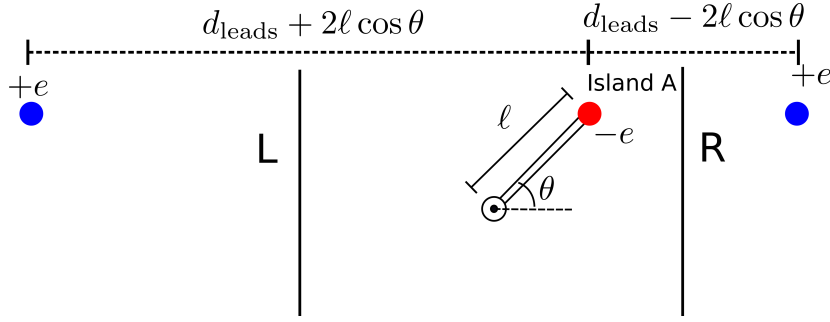


Figure 3.16: Sketch of the image charges induced on the leads by a charge on the island A. The island B is not represented in the figure.

3.3.4 Discussion of some model approximations performed in Sec. 3.2

In Sec. 3.2 we have performed some approximations to derive the stochastic and mean-field equations of motion. In this section, we discuss the most critical of these approximations based on the experimental proposals of Sec. 3.3.1 and Sec. 3.3.2.

3.3.4.1 Neglecting the image-charge conservative torque

In Sec. 3.2.2, we have neglected the angular dependence (through the capacitance) of the total energy stored on the islands. This angular dependence gives rise to a conservative torque, and we consider it here. To estimate this torque (“image-charge torque”), we take the Coulomb interaction between the charge on the islands and the induced image charges on the leads. We just regard the polarization on the leads coming as a response to the charge on the islands, neglecting the lead-lead interaction. Herewith, we only explicitly consider the device from Sec. 3.3.1. In the end, we comment on the differences we expect for the device from Sec. 3.3.2.

We will compare the image-charge torque to the “driving torque”, i.e. the torque arising from the driving electrostatic field. For island A charged and island B discharged, the driving torque as a function of θ is given by

$$M^A(\theta) = -E\ell \sin \theta. \quad (3.121)$$

For island B charged and A discharged the driving torque is simply

$$M^B(\theta) = -M^A(\theta). \quad (3.122)$$

Note that if the two islands are charged the driving torque is zero.

The interaction between the charge on the island and the image charge on the leads can be understood as the situation depicted in Fig. 3.16. The electric field on the position of the charged island A generated by the image charge from the left lead is

$$\mathbf{E}_L = \frac{1}{4\pi\epsilon} \frac{e}{(d_{\text{leads}} + 2\ell \cos \theta)^2} \hat{\mathbf{i}}, \quad (3.123)$$

and from the right lead is

$$\mathbf{E}_R = -\frac{1}{4\pi\epsilon} \frac{e}{(d_{\text{leads}} - 2\ell \cos \theta)^2} \hat{\mathbf{i}}, \quad (3.124)$$

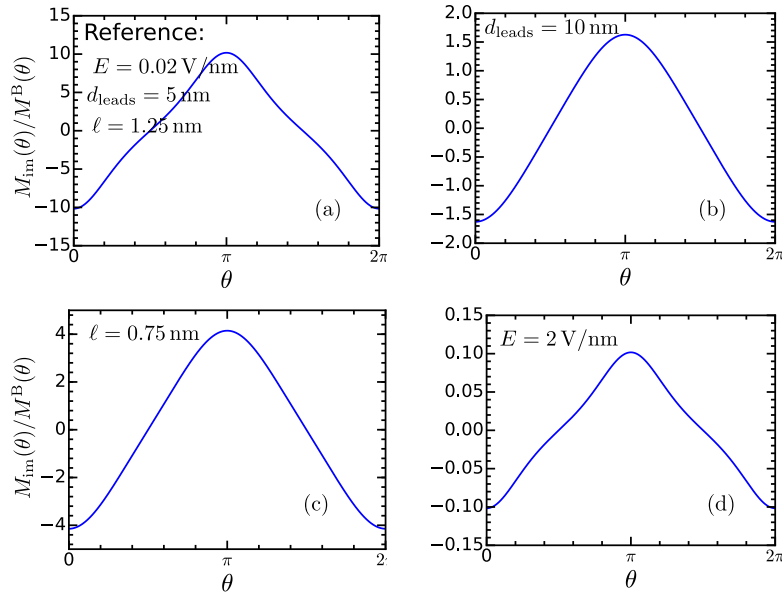


Figure 3.17: Ratio of the image-charge torque to the bias torque for the rotor of Sec. 3.3.1 in the case where just one island is charged. (a) is the result for the reference $E = 0.02 \text{ V/nm}$, arm length $\ell = 1.25 \text{ nm}$, and $d_{\text{leads}} = 5 \text{ nm}$. In the other panels we change (b) $d_{\text{leads}} = 10 \text{ nm}$, (c) $\ell = 0.75 \text{ nm}$, (d) $E = 2 \text{ V/nm}$. Note that in (d) it is unclear whether the rotor’s structure can resist such a strong electrostatic field.

where ϵ is the electric permittivity of the medium (we consider the value in vacuum for our estimate) ^{*}. The total image-charge torque impinged on the rotor is

$$M_{im} = -(E_R e - E_L e) \ell \sin \theta, \quad (3.125)$$

where $E_{L(R)}$ is the magnitude of $\mathbf{E}_{L(R)}$. The image-charge torque obtained for the case where the island B is charged while island A is discharged is the same (with the same sign) as from Eq. (3.125). The image-charge torque is zero at $\theta = 0$ ($\theta = \pi$) and $\theta = \pi/2$ ($\theta = 3\pi/2$) configurations, and it tends to stabilize the $\theta = 0$ ($\theta = \pi$) configuration. Moreover, this torque does not vanish for the case where the both islands are charged — but this state decays quickly to the singly charged state when $\theta = 0$ or $\theta = \pi$.

From Eqs. (3.121) and (3.125) (together with Eq. (3.122)) we can obtain the ratio of the image-charge torque to the driving torque:

$$\frac{M_{im}(\theta)}{M^A(\theta)} = -\frac{E_L - E_R}{E}, \quad (3.126)$$

$$\frac{M_{im}(\theta)}{M^B(\theta)} = \frac{E_L - E_R}{E}, \quad (3.127)$$

We plot $M_{im}(\theta)/M^B(\theta)$ in Fig. 3.17 for different values of the parameters. In (a) we have $E = 0.02 \text{ V/nm}$, arm length $\ell = 1.25 \text{ nm}$, and $d_{\text{leads}} = 5 \text{ nm}$. In this situation, the

^{*}A more appropriated formula for the image-charge interaction is given in Refs. [150] and [151]. However, for many metals, this formula does not differ appreciably from the one used in this thesis for lead-island distances in the order of nanometers.

image-charge torque can get up to approximately 10 times larger than the driving torque depending on the angle θ . Increasing the distance between the leads to $d_{\text{leads}} = 10$ nm (b), or decreasing the arm length to $\ell = 0.75$ nm (c), can reduce the magnitude of the ratio $M_{\text{im}}(\theta)/M^{\text{B}}(\theta)$. However, the image-charge torque is still strong for these parameters. In Fig. 3.17 (d) we consider $E = 2$ V/nm, and one sees that in this situation the magnitude of the ratio $M_{\text{im}}(\theta)/M^{\text{B}}(\theta)$ does not get larger than 10% for any θ . However, it is not clear whether the rotor's structure can resist such strong electrostatic field. Indeed, typical magnitudes required to break chemical bonds are in the scale of 1 V/nm (see e.g. Ref. [143]).

In the device from Sec. 3.3.1 the larger charge is spread over a long island. Taking the same timescale Γ^{-1} for the devices from Sec. 3.3.1 and Sec. 3.3.2, the length of the island in Sec. 3.3.2 needs to scale linearly with Q_{var} in order to obtain the same dimensionless parameters. This also implies the same d_{leads} and ℓ , and therefore the electrostatic field due to the image charges $E_{\text{L(R)}}$ should be the same for the both devices. The physical constraint imposed to the driving electrostatic field E , namely it cannot be strong enough to break the chemical bonds keeping the rotor together, does not change from one device to another. Moreover, both the image-charge torque and the driving torque scale linearly with the charge. These considerations indicate that the analysis performed here considering the device from Sec. 3.3.1 is also valid for the device from Sec. 3.3.2.

3.3.4.2 Assuming a single energy level on the electronic island

In Sec. 3.2.1.2 we have considered that the electronic island has a single energy level. The tunneling rates obtained in that section were later on used to derive the stochastic equations of motion in Sec. 3.2.3. In this section we base the discussion of this approximation on islands realized with gold nanoparticles. Experimental characterization of the energy spectrum of gold nanoparticles can be found in the literature. For instance, in Ref. [135] it was determined that the average level spacing of Au_{55} is 170 meV. The fact that such a measurement can be done at $T = 7$ K shows that this temperature is small enough to resolve well single electronic levels in the nanoparticle.

The level spacing must also be much larger than the quantum fluctuations, which are maximized for $\theta = 0$ ($\theta = \pi$) in the device from Sec. 3.3.1. Following¹⁵², we determine that the fluctuations are in the order of $\hbar\Gamma \exp(\xi \cos(\theta = 0, \pi)) = \hbar\Gamma \exp(\xi)$. Plugging in the values $\xi = 8$ (larger than used everywhere in this thesis) and $\Gamma = 6$ ns⁻¹ (from¹⁴⁴), we obtain 12 meV, which is more than 10 times smaller than the measured energy level spacing in Au_{55} .

3.3.5 Conclusions

In Sec. 3.3 we have discussed two experimental proposals: the first one, presented in Sec. 3.3.1, is meant to realize the stochastic equations of motion in a “single-electron limit”, where the islands can be either discharged or charged with one electron; the second one, presented in Sec. 3.3.2, is meant to realize the mean-field equations of motion in a “continuous-charging limit”, where the absolute value of the charge on the islands is typically much larger than the elementary charge. These proposals, together with the theory presented in Sec. 3.2, were used to unveil some of the challenges involved in

building a device to realize the nanoelectromechanical rotor from Sec. 3.1 in the regimes of interest (single-electron limit, continuous-charge limit, and parameter regions).

Our estimates indicate that the parameter regions whose dynamics was explored in Sec. 3.1 are accessible with the devices proposed in Sec. 3.3. However, the image charges induced on the leads can spoil the system through (i) dissipation on the leads and through (ii) a conservative torque impinging on the rotor. While (i) may be cured by replacing superconducting electrodes for the metallic leads, (ii) may restrict the parameter regions and/or operation timescale of the system.

We reiterate that our choice for gold nanoparticles and carbon nanotubes to realize the rotor was motivated by the amount of experimental data found in the literature. The physical systems composing the islands, rotor arms, and the bearing can be a completely different than the systems proposed here, and this may solve some of the problems we found in Sec. 3.3.

3.4 Nanoelectromechanical motor: rotational directionality

One of the intuitive applications of the nanoelectromechanical rotor we discuss in this thesis is yielding work, i.e. recasting it as a motor. Rotary motors are paradigmatic devices which transform input energies in controlled rotations. These rotations can be employed e.g. to power a nanomachine^{153,154}. In the microscale these devices have been assembled with nanowires^{155,156} and microfabricated gears¹⁵⁷. Since the advent of the first synthetic molecular motor^{15,16}, many different designs for nanoscale motors were proposed^{37,38,132,158–161} and realized^{17–24}. Significant steps towards application of rotary motors have been made: for instance, they have been used to propel a molecule in a Cu(111) surface¹⁶², rotate microscale objects¹⁶³, and control chemical reactions¹⁶⁴. These devices can be driven in many different ways, using e.g. light^{15,19,157}, chemical energy^{16,133}, electronic current^{20,23,24} and electric fields^{18,155}. Here, as in Ref. [37], Ref. [161], Ref. [38], and throughout this Chap. 3; we consider charge tunnelling to drive a nanoelectromechanical rotor.

The charging and discharging tunneling processes depend fundamentally on the size of the islands, and consequently on the size of the device. For nanoscale devices where the Coulomb blockade plays a role, as the device proposed in Sec. 3.3.1, the islands can only host a small number of electrons (in the extreme case only one). In this case, charge fluctuations caused by the stochastic nature of the tunnelling process lead to torque fluctuations on the rotor. For rotors with “macroscopic” islands^{*}, as the device proposed in Sec. 3.3.2, charge fluctuations are typically irrelevant because they are very small compared to the scale of the charge on the islands. The charge dynamics is therefore well captured by a mean-field approach, as the one described in Sec. 3.2.4. Similarly, torque noise arising from thermal fluctuations is typically negligible compared to the other torques acting upon a macroscopic rotor. Moreover, this torque can be controlled via the temperature.

^{*}With “macroscopic” here we mean with at least one dimension much larger than one nanometer. For example, the electronic islands of the rotor from Sec. 3.3.2 spans micrometers in one direction.

For many applications it is crucial to attain control over the directionality of the rotations of the motor. One possible way of achieving this is picking a specific initial condition which leads to rotations predominantly in the desired direction. The initial condition is characterized by the initial angular momentum $L(t=0) = L_0$, the initial angle $\theta(t=0) = \theta_0$, and the initial electronic charges $Q_A(t=0)$ and $Q_B(t=0)$ on the islands. However, the experimental preparation of a specific initial condition can be difficult, imprecise or even inconvenient, depending on the system scale, suppression of noise-sources, etc. Moreover, imperfections in the rotor fabrication, e.g. in the length of its arms, angle between them, capacitances of the islands, etc. could also lead to uncertainty in the rotational direction. Another way of attaining rotational directionality is to make a rotation direction “preferable”. With “preferred direction” we mean that most of, or even all initial conditions lead to rotations in this direction. This was achieved e.g. in the context of molecular motors¹³³, where the sense of rotation can be controlled by the choice of chemical reactants that power the motor. In the context of rotors driven by electron tunneling, a spatially asymmetric arrangement of source and drain electrodes was also proposed³⁸. If there is no much freedom on arranging the source and drain contacts one can introduce a preferred rotation direction by tailoring the rotor’s geometry. For a perfectly symmetric rotor, as we have regarded until here, it is intuitively clear that no directionality is achieved: for each initial condition leading to a certain rotation direction there exists another one leading to the opposite direction. This gives rise to the question which symmetries of the rotor one has to break in order to achieve directionality of the rotatory motion.

In this section we show that a rotor with tilted, uneven arms can feature a preferred direction of rotation. We start by introducing the modified mean-field and stochastic equations of motion of that rotor in Sec. 3.4.1. The experimental realization of these equations is discussed in Sec. 3.4.2. In Sec. 3.4.3, we use the mean-field equations to show that in the continuous-charging limit tilting the arms or making them uneven alone does not suffice to introduce a preferred rotational direction: one needs to do both. Moreover, we define a measure of asymmetry which allows us to explore the parameter space of the mean-field equations introduced in Sec. 3.4.1. This is to assess the impact of fabrication imperfections in the rotor. For some areas in the parameter space all initial conditions end up rotating in the same direction and with the same time-averaged angular momentum. It means that no control over initial condition is required to achieve a desired sense of rotation. In Sec. 3.4.4 we show that one can also introduce a preferred direction of rotation in the single-electron limit using the stochastic equations of motion. The parameter space is also investigated, and it shows large areas of rotational directionality. Finally, we wrap this section up in Sec. 3.4.5. The work presented in this section was published in Ref. [165].

3.4.1 Equations of motion

The equations of motion employed in Sec. 3.1 describe the dynamics of a symmetric rotor: it was shown in Sec. 3.1.2 that there is no preferred sense of rotation due to the invariances of the equations of motion. Although the argument in Sec. 3.1.2 was given for the mean-field equations, this invariance also persists in the stochastic equations of

motion^{*}. In order to break this symmetry, we bend the rotor's arms, such that $\theta_A = \theta$ but now $\theta_B = \theta + \beta$, where $\beta \neq \pi$. We will see that this alone is not enough to break the rotor's symmetry and we will need to make the arms uneven. This can be achieved by splitting the parameter η_0 into two different parameters η_A and η_B . The mechanical equations of motion, in both mean-field and stochastic approaches, are given by

$$\frac{d}{d\tau}\Lambda = -\eta_A \sin \theta_A P_A - \eta_B \sin \theta_B P_B - \gamma\Lambda, \quad (3.128)$$

$$\frac{d}{d\tau}\theta = \Lambda, \quad (3.129)$$

where in the stochastic case $P_{A(B)}$ are *discrete* stochastic variables which can acquire the values 0 and 1 and in the mean-field case $P_{A(B)}$ vary *continuously* between 0 and 1. Both parameters η_A and η_B contain both the strength of the driving and the “unevenness” of the arms. We can rewrite these parameters such to assign each property to a single parameter. We define χ and redefine η_0 such that $\eta_A = \sqrt{2}\eta_0 \sin \chi$ and $\eta_B = \sqrt{2}\eta_0 \cos \chi$. Notice that if $\chi = \pi/4$ the arms are even and we recover the symmetric equations of motion (with η_0 having the same definition as in Sec. 3.1). With this definition, Eq. (3.128) can be rewritten as

$$\frac{d}{d\tau}\Lambda = -\eta_0\sqrt{2}(\sin \chi \sin \theta P_A + \cos \chi \sin(\theta + \beta) P_B) - \gamma\Lambda, \quad (3.130)$$

where now we have used the definitions $\theta_A = \theta$ and $\theta_B = \theta + \beta$.

The dimensionless charging rates used here have the same definition as in Sec. 3.1,

$$w_L(\theta_{A(B)}) = e^{-\xi \cos \theta_{A(B)}}, \quad (3.131)$$

$$w_R(\theta_{A(B)}) = e^{\xi \cos \theta_{A(B)}}. \quad (3.132)$$

While in the mean-field approach they enter the deterministic equations of motion

$$\frac{d}{d\tau}P_{A(B)} = (1 - P_{A(B)})w_L(\theta_{A(B)}) - P_{A(B)}w_R(\theta_{A(B)}), \quad (3.133)$$

in the stochastic approach they compose the transition probabilities from Eqs. (3.20) and (3.21).

3.4.2 Experimental realization

While in Sec. 3.4.1 we have based our discussion of the equations of motion we use in Sec. 3.4 on alterations of the mean-field and stochastic equations presented in Sec. 3.1, it is not clear whether these alterations “make sense” from an experimental point of view. Herewith we discuss changes to the devices from Sec. 3.3.1 (single-electron limit) and Sec. 3.3.2 (continuous-charging limit) in order to realize the equations of motion introduced in Sec. 3.4.1.

^{*}To see that, make the changes of variables suggested in Sec. 3.1.2 in the Fokker-Planck equations of motion given by Eqs. (3.23)-(3.26).

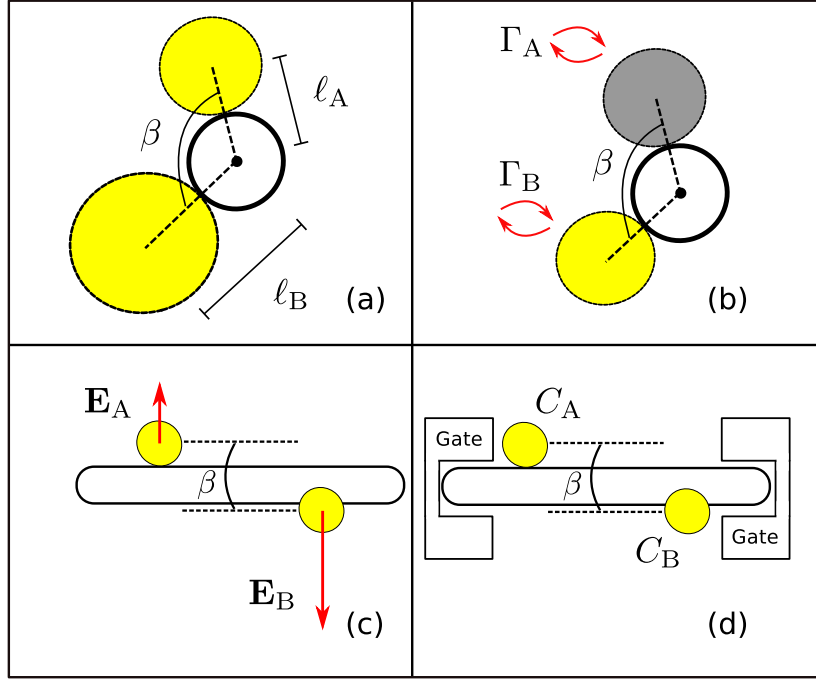


Figure 3.18: Sketch of possible alterations of the rotor in order to obtain uneven ($\chi \neq \pi/4$), tilted ($\beta \neq \pi$) arms. (a) The arm lengths $\ell_A \neq \ell_B$, (b) the tunneling timescales $\Gamma_A^{-1} \neq \Gamma_B^{-1}$, (c) the magnitude of the driving electrostatic fields $E_A \neq E_B$, and (d) the maximal charge variations $Q_{\text{var}}^A \neq Q_{\text{var}}^B$.

3.4.2.1 Tilting the rotor's arms: $\beta \neq \pi$

To attain $\beta \neq \pi$ in the devices from Sec. 3.3.1 and Sec. 3.3.2 one needs to attach the gold nanoparticles/nanowires angle-selectively on the support shaft (carbon nanotube), as illustrated in Fig. 3.18. This may be yet beyond reach experimentally, specially considering the minute radius of the carbon nanotubes needed to obtain the values of ξ in the order of 1. We stress that one could devise the rotor in a completely different way. For example, a chiral molecule could compose the entire rotor. From now on, we consider that it is *in principle* possible to engineer β with a certain precision. Later on, we will access which precision is needed in order to obtain rotational directionality in the rotor.

3.4.2.2 Making the arms uneven: $\chi \neq \pi/4$

The definition of the parameter $\eta_{A(B)}$ depends on the device. For the device from Sec. 3.3.1,

$$\eta_{A(B)} = \frac{e\ell_{A(B)}E_{A(B)}}{\Gamma_{A(B)}^2 I}, \quad (3.134)$$

and for the device from Sec. 3.3.2,

$$\eta_{A(B)} = \frac{Q_{\text{var}}^{A(B)}\ell_{A(B)}E_{A(B)}}{\Gamma_{A(B)}^2 I}. \quad (3.135)$$

In the definitions we have already denoted the parameters which can in principle be made arm-dependent with “A (B)”.

For example, one can have lengths $\ell_A \neq \ell_B$ (a), as illustrated in Fig. 3.18 (a). This can be achieved e.g. by realizing the islands with nanoparticles/nanowires of different diameters. This procedure also produces islands of different capacitances, but this can be corrected via gate electrodes. However, (a) also requires the tunneling lengths to be different for different islands, otherwise ξ will be island-dependent (see the definition given by Eq. (3.112)).

Another way of making the arms uneven is through $\Gamma_A \neq \Gamma_B$ (b), as depicted in Fig. 3.18 (b). This can be achieved e.g. by using different materials to build the islands. However, this procedure changes the equations of motion of the charges, in that the timescale of charging is not the same for different islands. In other words, the dimensionless charging rates from Eqs. (3.131) and (3.132) acquire different prefactors $\Gamma_{A(B)}$.

Making the magnitude of the driving electrostatic field island dependent, i.e. $E_A \neq E_B$ (c), has the advantage of not altering other dimensionless parameters (see Fig. 3.18 (c)). This can be achieved in the devices from Sec. 3.3.1 and Sec. 3.3.2 because the islands can be well separated along the support shaft’s axis.

Finally, in the continuous-charging limit one can also use the gate electrodes to make $Q_{\text{var}}^A \neq Q_{\text{var}}^B$ (d). This situation is illustrated in Fig. 3.18 (d). Notice that (d) just applies to the device from Sec. 3.3.2, while (a), (b), and (c) apply to the devices from both Secs. 3.3.1 and 3.3.2.

3.4.3 Rotational directionality in the continuous-charging limit

In this section we investigate how one can obtain a preferred rotational direction by breaking the rotor’s symmetry in the continuous-charging limit using the mean-field equations from Sec. 3.4.1. As described in Sec. 3.1.2, invariances of the equations of motion can lead to coexistence of attractors in phase space which rotate in opposite senses. We are interested in obtaining information over the basin of attraction of those attractors, and therefore we use the time-averaged angular momentum defined by Eq. (3.11). In particular we are interested in obtaining $\overline{\langle \Lambda \rangle} \neq 0$ (defined by Eq. (3.18)), which is equivalent to attaining a preferred direction of rotation. In Sec. 3.4.3.1 we show that alterations of β or χ alone do not lead to rotational directionality. In Sec. 3.4.3.2 we show how one should alter both parameters simultaneously to maximize directionality.

3.4.3.1 Changing either β or χ : no directionality of the rotatory motion

As mentioned before, individual alterations of the parameters β or χ (e.g. just $\beta \neq \pi$) do not lead to a preferred rotation direction. This occurs because in that case, the mean-field equations of motion from Sec. 3.4.1 also possess an invariance: for every counterclockwise-rotating solution $(\theta(t), \Lambda(t))$ there is a clockwise-rotating solution $(\tilde{\theta} = -\theta(t) + \phi, \tilde{\Lambda} = -\Lambda(t))$, where ϕ is a fixed angle. Therefore, $\overline{\langle \Lambda \rangle} = 0$. Although those individual changes in the parameters do not introduce a preferred rotation direction, it is instructive to understand the effects of changing β and χ in the initial-condition space. Examples can be seen in Fig. 3.19, where $\langle \Lambda \rangle$ is plotted as a function of the initial conditions (Λ_0, θ_0) . Red stands for clockwise (negative Λ) and blue for counter-clockwise

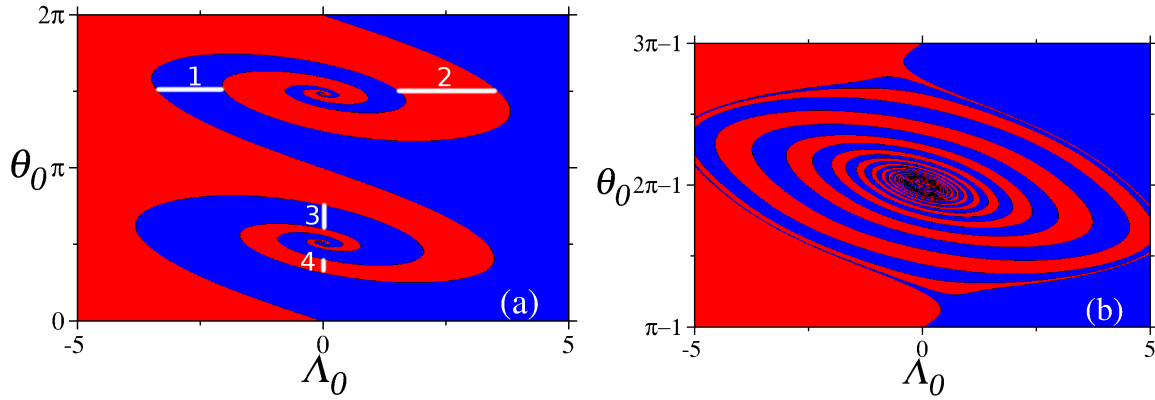


Figure 3.19: Time averaged angular momentum (color) $\langle \Lambda \rangle$ as a function of the initial conditions (Λ_0, θ_0) for $\xi = 2.0$, $\gamma = 1$, $\eta_0 = 10$ and $\tilde{P}_A(\tau=0) = \tilde{P}_B(\tau=0) = 0$. In (a) $\chi = 0.7$ and $\beta = \pi$. Marked with white lines is the width of several regions with the same $\langle \Lambda \rangle$. In (b) $\chi = \pi/4$ and $\beta = 2$ (notice the shifted θ_0 -axis). The color coding is as in Fig. 3.7. These results were obtained using the mean-field equations from Sec. 3.4.1.

(positive Λ) rotational direction. These two colors also indicate the basins of attraction of the two rotatory attractors that coexist in phase space. Notice that although $\langle \Lambda \rangle$ changes sign across the initial-condition space, its absolute value is constant. In Fig. 3.19 (a) one sees the case $\chi \neq \pi/4$ and $\beta = \pi$, while in (b) the case $\chi = \pi/4$ and $\beta \neq \pi$ is shown. The Fig. 3.19 (a) looks qualitatively similar to Fig. 3.7 (a) and (b). Again, one has fixed points (the same as for the symmetric rotor) and a patterned structure that spirals towards them. Nevertheless, the point anti-symmetry around the fixed points $\theta = \pi/2$ and $\theta = 3\pi/2$ ($\Lambda = 0$) is no longer present. This can be seen by comparing the lengths of the line segments 1 and 2 (3 and 4) in Fig. 3.19 (a), which are the widths of regions with the same $\langle \Lambda \rangle$ measured symmetrically with respect to the aforementioned fixed points. The point anti-symmetry around the fixed points $\theta = 0$ and $\theta = \pi$ is preserved though. Fig. 3.19 (b) presents other differences when compared to Fig. 3.7 (a) and (b): Two fixed points disappear and other two are localized at different positions, namely $\theta = 2\pi - \beta/2$ and $\theta = \pi - \beta/2$. Nevertheless, the initial-condition space is still point anti-symmetric with respect to the fixed point positions, and therefore again one has $\overline{\langle \Lambda \rangle} = 0$. The complete breakage of these point anti-symmetries is just possible by setting *both* $\chi \neq \pi/4$ and $\beta \neq \pi$, and it is exactly this symmetry-breaking that will be exploited to generate directed rotational motion in the next section.

3.4.3.2 Changing both β and χ : directionality of the rotatory motion

In order to obtain a preferred rotational direction one needs to set $\chi \neq \pi/4$ and $\beta \neq \pi$ simultaneously. The resulting set of equations of motion does not feature pairs of solutions $(\theta(t), \Lambda(t))$ and $(\theta'(t), \Lambda'(t))$ such that $\theta'(t) = -\theta(t) + \phi$ and $\Lambda'(t) = -\Lambda(t)$. Since this invariance is no longer present in the equations of motion, one expects directionality to emerge. However, we are not just interested in showing that for certain values of the parameters one obtains directionality; we also want to obtain the regions of directionality in the parameter space. Moreover, we want to know what is the “degree of directionality” in these regions, i.e. a measure of how many initial conditions lead to

the same rotation sense. In the following we define a directionality measure, which will be used later on in parameters scans in order to pursue the aforementioned objectives.

Directionality measure in the initial-condition space

To quantify the directionality of the rotatory motion we define a directionality measure in the initial-condition space

$$M = \frac{\overline{\langle \Lambda \rangle}}{\sqrt{\overline{\langle \Lambda \rangle^2}}}, \quad (3.136)$$

where the overbar was defined in equation (3.18). Note that M is zero when $\overline{\langle \Lambda \rangle} = 0$. For the case where all the θ_0 lead to rotation in the same direction (and with the same time-averaged angular momentum) one has $M = \pm 1$. By changing from negative to positive values of M (or vice-versa), we just change the direction of rotation. The possible values of M and their meanings can be summarized as

$M = 1$: All initial angles lead to steady-state counterclockwise rotations with the same $\langle \Lambda \rangle$;

$M = -1$: All initial angles lead to steady-state clockwise rotations with the same $\langle \Lambda \rangle$;

$0 < M < 1$: The ensemble of trajectories obtained through an uniform distribution over the initial angle θ_0 rotates counterclockwise on average in the steady-state, but not with the same $\langle \Lambda \rangle$;

$-1 < M < 0$: The ensemble of trajectories obtained through an uniform distribution over the initial angle θ_0 rotates clockwise on average in the steady-state, but not with the same $\langle \Lambda \rangle$;

$M = 0$ The ensemble of trajectories obtained through an uniform distribution over the initial angle θ_0 is standstill on average.

Notice that the cases where $|M| \neq 1$ may include standstill, oscillatory, and rotatory regimes for different initial angles.

In the following, we use the directionality measure defined here to assess directionality over a large set of parameters.

Numerical evaluation of M in the parameter space

The Fig. 3.20 shows M as a function of the parameters β and χ . White indicates no rotational directionality, while from white to blue (red) an increasing value of the directionality measure is found, with a positive (negative) $\overline{\langle \Lambda \rangle}$. In Fig. 3.20 we set the parameter $\gamma = 1$ and vary η_0 (in (a) to (c)). Along the two lines $\beta = \pi$ and $\chi = \pi/4$ we have $M = 0$, as expected. The M values are also anti-symmetric about those lines and, consequently, point-symmetric with respect to $(\chi = \pi/4, \beta = \pi)$. This point-symmetry stems from the analytic form in which the parameters χ and β appear into the mean-field equations from Sec. 3.4.1, and therefore it is present independently of the chosen γ and η_0 (and ξ). In Fig. 3.20 (a) ($\eta_0/\gamma = 5$) and (b) ($\eta_0/\gamma = 10$) there are regions with $|M| = 1$, in which a total rotational directionality is achieved. For

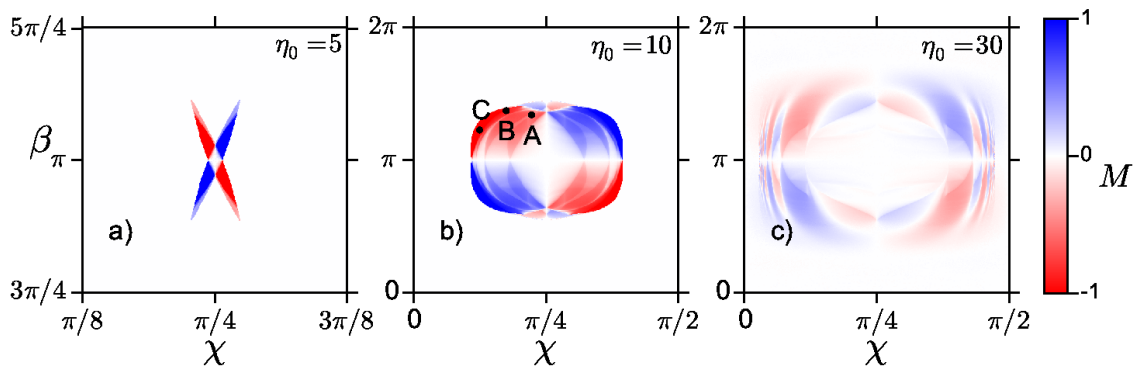


Figure 3.20: Directionality measure M defined in equation (3.136) as a function of the parameters (χ, β) , for $\xi = 2$ and $\gamma = 1$. These results were obtained using the mean-field equations from Sec. 3.4.1.

instance, the point C in Fig. 3.20 (b) has $M = 1$. In this case all the initial conditions lead to the same direction and magnitude of rotation (even for large $|\Lambda_0|$). However, in Fig. 3.20 (a) almost all the parameter space presents $M = 0$, since for such small ratio η_0/γ the rotor has $\langle \Lambda \rangle = 0$ for most of the (χ, β) values. Regions where $|M| < 1$ are also displayed in Fig. 3.20 (b) and (c) ($\eta_0/\gamma = 30$). Interestingly, Fig. 3.20 (c) presents no $|M| = 1$ regions, although larger extensions of the parameter space have $|M| > 0$. No significant changes in these figures are verified when $\xi = 1$ or $\xi = 4$.

Examples for the cases $1 > |M| > 0$ are the points A and B. For these points we generate the initial-condition space of Fig. 3.21. In Fig. 3.21 (a)(b) we plot $\langle \Lambda \rangle$ in the initial-condition space for the same parameters as in the point A(B) of Fig. 3.20. There, we find $M = 0.47$ ($M = 0.88$). The white line is drawn in Fig. 3.21 just with the purpose of indicating the locus where the average over initial conditions is performed. By comparing the segments of the white line which are inside regions with positive and negative $\langle \Lambda \rangle$ in both Fig. 3.21 (a) and (b), and noting that $|\langle \Lambda \rangle|$ is the same for both red and blue regions, one can understand why the point B presents a stronger rotational directionality than point A in Fig. 3.20 (b). We do not show a figure with $\langle \Lambda \rangle$ as a function of the initial conditions for the same parameters as on the point C of Fig. 3.20 (b) because *all* the initial conditions lead to the same $\langle \Lambda \rangle$ value (even for $\Lambda_0 \neq 0$).

3.4.4 Rotational directionality in the single-electron limit

If the size of the rotor (in particular the islands) is shrunk, such that only single electrons are transferred, the mean-field description used in Sec. 3.4.3 (and presented in Sec. 3.4.1) is not suitable. The charge fluctuations can be of the order of the mean values and it is more appropriate to consider the (dis)charging of the islands as a hopping process. The stochastic equations of motion presented in Sec. 3.4.1 are suited to describe the extreme situation where the islands can bear a maximal charge $-e$ (single-electron limit). Herewith, we use these equations to show that one can introduce a preferred direction of rotation in the rotor within the single-electron limit. For the sake of clarity, we consider that torque noise stemming from thermal fluctuations is negligible compared

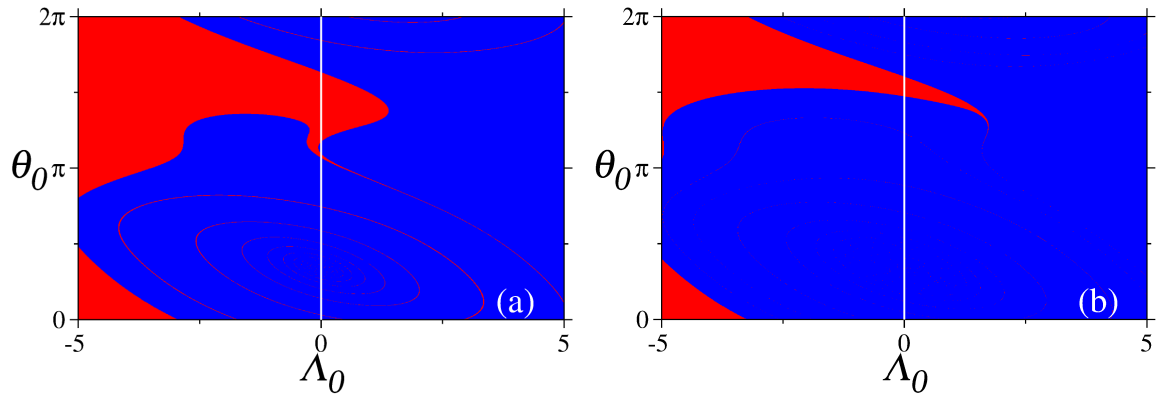


Figure 3.21: The averaged angular momentum $\langle \Lambda \rangle$ as a function of the initial conditions (Λ_0, θ_0) for the set of parameters correspondent to (a) point A ($\chi = 0.7, \beta = 4.2$), (b) point B ($\chi = 0.55, \beta = 4.3$) in Fig. 3.20 (b). The color coding is as in Fig. 3.7. Along the white line in the figures the directionality measure was calculated, as (a) $M \approx 0.47$ and (b) $M \approx 0.88$. These results were obtained using the mean-field equations from Sec. 3.4.1.

to that one coming from charge fluctuations.

In Sec. 3.4.4.1 we introduce a new directionality measure suited to the stochastic equations. By means of this measure, we scan the parameter space of the stochastic equations for regions of strong directionality in Sec. 3.4.4.2.

3.4.4.1 Directionality measure for the stochastic equations

In order to assess how precise one needs to fabricate the rotor to obtain rotational directionality, we will calculate directionality measure as a function of the parameters (χ, β) . However, since in the present model the tunneling is a stochastic process, one needs to redefine the directionality measure. Instead of considering $\langle \Lambda \rangle$ and $\langle \Lambda \rangle^2$, we consider their average over the realizations $\overline{\langle \Lambda \rangle}_{\text{re}}$ and $\overline{\langle \Lambda \rangle^2}_{\text{re}}$, such that the new directionality measure is

$$M_{\text{stoch}} = \frac{\overline{\langle \Lambda \rangle}_{\text{re}}}{\sqrt{\overline{\langle \Lambda \rangle^2}_{\text{re}}}}, \quad (3.137)$$

where $\langle \dots \rangle_{\text{re}}$ is an average over realizations and the overbar the same average over initial conditions as in equation (3.136). The directionality measure $M_{\text{stoch}} = 0$ when $\overline{\langle \Lambda \rangle}_{\text{re}} = 0$. For $M_{\text{stoch}} = \pm 1$ one has *all* initial conditions leading to net rotations in the same direction with the same $\overline{\langle \Lambda \rangle}_{\text{re}}$, such that the sign just indicates the direction of rotation. It must be noted that the sign of $\Lambda(t)$ within a *single trajectory* can change with time, even though we have $M_{\text{stoch}} = \pm 1$.

Moreover, for the parameters we have used in our simulations, all dependence on the initial conditions is quickly erased and one just needs to average over realizations. Therefore values $0 < M_{\text{stoch}} < 1$ and $-1 < M_{\text{stoch}} < 0$ are not observed.

3.4.4.2 Numerical evaluation of M_{stoch} in the parameter space

As we have done in Sec. 3.4.3.2 in the continuous-charging limit, we calculate M_{stoch} numerically in the parameter space. Fig. 3.22 shows M_{stoch} as a function of the

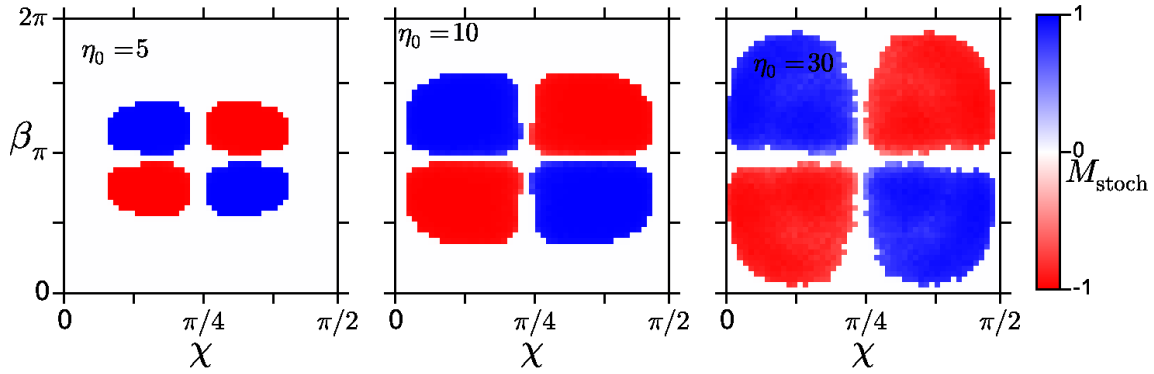


Figure 3.22: Directionality measure M_{stoch} defined in equation (3.137) as a function of the parameters (χ, β) , for $\xi = 2$ and $\gamma = 1$ (same parameter set and color coding as in Fig. 3.20). These results were obtained using the stochastic equations from Sec. 3.4.1.

parameters β and χ for the same γ , η_0 and ξ as in Fig. 3.20. White indicates no rotational directionality, while an increasing value of the directionality measure is indicated by a transition from white to blue (red), with a positive (negative) $\langle\langle\Lambda\rangle\rangle_{\text{re}}$. M_{stoch} presents the same symmetry in the parameter space as M does. Along the two lines $\beta = \pi$ and $\chi = \pi/4$ we have the expected $M_{\text{stoch}} = 0$ value. The M_{stoch} values are also anti-symmetric about those lines and, consequently, point-symmetric with respect to $(\chi = \pi/4, \beta = \pi)$. Again, this symmetry is independent of the chosen η_0 and γ . The Fig. 3.22 features extensive regions of total rotational directionality, namely in the red and blue areas (as mentioned before, we did not observe the cases $-1 < M_{\text{stoch}} < 0$ and $0 < M_{\text{stoch}} < 1$). This represents a striking difference to the results obtained through the mean-field equations (Fig. 3.20). The results also do not depend on η_0/γ so sensitively as in the mean-field case (compare Fig. 3.22 with Fig. 3.20). Nevertheless, the $|\langle\langle\Lambda\rangle\rangle_{\text{re}}|$ achieved are smaller than the typical $|\langle\Lambda\rangle|$ from the mean-field case. This can be partially explained by the fact that $\Lambda(t)$ can change its sign within a single trajectory.

3.4.5 Concluding remarks

In the present section we have studied how to control the rotational direction of an electromechanical rotor. We considered two different limits: the continuous-charging limit, whose dynamics were described using the mean-field equations of motion; and the single-electron limit, whose dynamics were described using the stochastic equations of motion. The continuous-charging limit is suited to systems where the islands are big objects which can bear many electrons (and wholes). The single-electron limit is suited to nanoelectromechanical devices where the Coulomb blockade effect is relevant and whose islands are maximally occupied by a single elementary charge.

In the continuous-charging limit, the sense of rotation can be controlled in two different ways: one can either select the rotational direction via choosing an appropriate initial condition, or one can break the symmetry of the rotor to introduce a preferred rotational direction. In order to experimentally perform the first method, the precision of the initial condition preparation must be high enough to resolve structures in the

initial-condition space. While our mean-field calculations show that increasing the ratio η_0/γ also increases the initial-condition space size of the structures, through the hopping process calculations one sees that charge fluctuations can destroy the dependence of the system on the initial condition. This means that an initial-condition preparation scheme may fail for a real nanoelectromechanical rotor (with nanoscale islands). Apart from that, fabrication imperfections can also spoil the attempts of selecting a specific initial condition which leads to a certain direction of rotation. In contrast, our numeric simulations show that, by breaking the rotor's symmetry, most or even *all* initial conditions lead to the same rotational direction. For this reason, we focused on the symmetry-breaking procedure.

We have shown that one needs to change the system's parameters χ and β *simultaneously* in order to break the symmetry of the rotor. The parameter β is tuned by setting a tilting angle between the two rotor's arms. There are many ways of tuning χ , e.g. impinging electrostatic fields of different magnitudes on the islands A and B or (in the continuous-charging limit) having islands with different maximal charges $Q_{\max}^{A(B)}$. The parameter space of both mean-field and stochastic equations features areas where a total rotational directionality is present. In these areas, initial-condition space scans indicate that the same $\langle\Lambda\rangle$ ($\langle\langle\Lambda\rangle\rangle_{\text{re}}$) in the mean-field (stochastic) equations is obtained *independently* of the chosen initial condition. The symmetry-breaking procedure works for large sections of the parameter space. In an experimental realization of our equations, imperfections in the rotor fabrication within the limits of these sections would not spoil the symmetry-breaking. As shown in Sec. 3.4.4, the directionality is not fundamentally linked to determinism, as a preferred rotational direction still exists although charge fluctuations completely erase the dependence on the initial conditions. When compared to the mean-field simulations, our stochastic simulations feature large regions in the parameter space leading to rotational directionality. Thus, this procedure may work specially well for nanoelectromechanical rotors.

Chapter 4

Summary and outlook

In this thesis we investigated coupled electronic and nuclear (mechanical) dynamics in the nanoscale, and we focused on their dependence upon the system parameters. As discussed in the introductory Chap. 1, this coupling can lead to complex dynamics nontrivially dependent on the system parameters. As a consequence, a specific functionality/phenomenon exists in a limited region of the parameter space. In this thesis, we were interested in this kind of nanoscale complex systems, and how to tune into regions of their parameter space leading to desired dynamics. We considered two systems which are “complimentary” in many aspects.

In Chap. 2 we considered a minimal example from supramolecular chemistry commonly found in nature^{39,40}: a molecular dimer composed of identical molecules. This system favors a quantum description in that it can display intrinsically quantum phenomena (e.g. quantum beating^{41,42}).

In Chap. 3 we considered a synthetic nanomachine: a nanorotor driven by charge tunneling. It favors assembly integrating (typically) larger, bulk-like systems such as nanoparticles and carbon nanotubes. These systems are often “more classical” than a molecular dimer: for example, charge tunneling between nanosized electrodes is often described using rate equations^{1,2}, and wall rotation in a multi-walled carbon nanotube is often described via Langevin equations³.

In the following, we summarize our main findings and discuss some of the new research directions stemming from the present work.

4.1 The molecular dimer

4.1.1 Summary

In Chap. 2 we investigated the nonradiative decay (NRD) dynamics in molecular aggregates, focusing on their dependence upon the intermolecular interaction. Electronic NRD is critical in a variety of molecular systems. In nature, it is essential e.g. in the vision process^{6,7,27,28}, photosynthesis^{8,43,44}, and DNA photoprotection^{9,45–47}. In technological applications, it is important in the context of e.g. OLEDs⁴⁸, light-driven molecular rotary motors⁴⁹, and light-driven molecular switches^{10,25,26}.

As a proof of concept we considered the simplest aggregate featuring the mechanism we are interested in: a dimer formed by identical monomers interacting via transition dipole-dipole interaction. Typically, photoemission in molecular systems occurs from the lowest excited state of a given multiplicity (Kasha’s rule⁶²). Therefore, we consider two electronic states in the monomer model. The electronic excited state can decay nonradiatively. We consider the typical situation (e.g. via conical intersections) where

the NRD occurs in a limited (well-localized) region of the monomeric nuclear space (NRD channel).

Since molecular aggregates can be formed from a variety of molecules, they can feature various *monomeric* potential energy surfaces (PESs). For simplicity, we consider here harmonic, shifted PESs. This model directly relates to previous studies of dimers, where NRD has not been taken into account (see e.g. Refs. ^{51,75-78,80}). A single nuclear coordinate is considered explicitly in each monomer. The influence of the other coordinates upon the dynamics is treated via a standard quantum open systems approach. Explicit consideration of an additional coordinate would introduce numerical difficulties and provide no further insight into the mechanism we are interested in. By solving the resulting multilevel Redfield equation of motion we showed that the dimer has a different NRD lifetime than its monomer. The magnitude of this difference depends on the strength of the intermolecular interaction. Remarkably, the way the intermolecular interaction influences the NRD dynamics depends on the position of the NRD channel: we found that the NRD lifetime can increase, be practically insensitive, or decrease with increasing interaction strength. The range of NRD lifetime variation depends exponentially on the shift between the monomeric PESs.

The intermolecular interaction we considered here is often relevant in molecular aggregates⁶⁴⁻⁶⁶. Hence, our results show that *molecular aggregation* can lead to significant changes in the NRD lifetime. The influence of molecular aggregation upon the *radiative* lifetime has been extensively studied⁶⁷⁻⁶⁹, and it is well understood e.g. in J- and H-aggregates. Our results expand this picture considerably by showing that also the *nonradiative* component of the lifetime is changed by aggregation. Our mechanism just requires transition dipole-dipole interaction and well-localized monomeric NRD channels. These requirements are commonly met by aggregates/molecules, and therefore this mechanism will be present in a variety of molecular aggregates.

A direct consequence of our mechanism is to the fluorescence quantum yield of molecular aggregates. We showed an exemplary calculation where the NRD lifetime can be tuned over 4 orders of magnitude by varying the interaction strength, and the tunability is not limited to that value. This can considerably alter the fluorescence quantum yield, specially in (but not limited to) J-aggregates, where bright states are located at the bottom of the exciton band. Our results also indicate that quantum yield measurements can, e.g., be exploited for the detection of molecular aggregation, pinpointing of NRD channel locations in molecules, and to infer the geometry of molecular aggregates.

4.1.2 Outlook

Consideration of real molecules/aggregates would make it possible to quantitatively test the mechanism introduced here against experimental results. This is a clear next research step. In practice, this means one needs to substitute PESs suited to specific molecules for the ones considered here. This may include more than one reaction coordinate and non-harmonic PESs, as exemplified by retinal^{7,27}. The numerical simulation performed here cannot account for more than two reaction coordinates. To include more coordinates, one can e.g. determine the dimer PESs via Born-Oppenheimer approximation and use surface hopping to simulate the dynamics^{? ?}. For arbitrary monomer PESs, the

transition dipole-dipole interaction can impose more severe modifications to the NRD dynamics. This is because the shape of the dimer PESs can differ from the monomer excited-state PES's shape even in the adiabatic limit. For instance, the dimer's PESs may present a minimum even if the excited-state PES of the monomer does not. This can lead to a fundamental change of the nuclear dynamics in the diabatic case, e.g. stabilizing a photodissociation.

In the end of Sec. 4.1.1 we discussed the consequences of our mechanism to the fluorescence quantum yield. Actually, it is well known that fluorescent molecules can become non-fluorescent when in the aggregate state. This phenomenon is called aggregation-caused quenching (ACQ), and is a hindrance to solid state devices where one is interested in a large quantum yield (e.g. in OLEDs)^{166,167}. In ACQ, the electronic excitation of the aggregate quickly decays via nonradiative pathways. It is also known that aggregation can also make non-fluorescent molecules become fluorescent. This is known by aggregation-induced emission (AIE), and has long been attributed to restriction of rotational motion in the monomer^{166,167}. Our mechanism can decrease/increase the NRD lifetime over many orders of magnitude and therefore can also lead to ACQ/AIE. In some molecules for which AIE occurs, the distortion of the aggregate's PESs induced by intermolecular interaction may be responsible for the restriction of intramolecular rotational motion. If confirmed, this would link the previous explanation of AIE with our mechanism.

A very exciting question stemming from our work is whether our mechanism is involved in singlet exciton fission. In organic semiconductors, a spin-singlet exciton may convert into a pair of spin-triplet excitons residing on different chromophores, entangled in an overall spin-zero state. This process is called singlet exciton fission, and it has long commanded interest as an exceptionally fast channel to generate triplet excitons. It may find application in the area of single-junction solar cells: by converting high-energy photons into two low-energy excited states, singlet fission offers a means to overcome thermalization losses. The mechanism behind this phenomenon is as-yet unknown. Recently, it has been suggested that NRD processes can also be involved in singlet fission. Some theoretical studies propose a conical intersection between a photoexcited singlet state and an intermediary dark state in the monomer level to be involved in the singlet fission mechanism — see e.g. Ref. [71], whose findings are supported by Ref. [70]. Through aggregation this dark state, which is not accessible to the excited-state dynamics of the monomer, becomes populated. Since our mechanism accounts for such situation, it may lead to singlet fission.

4.2 The nanoelectromechanical rotor

In Chap. 3 we investigated the dynamics of nanoscale rotors driven by charge tunneling. The rotors are composed of electronic islands linked to a shaft via insulating arms. The electronic islands can exchange electrons with flanking leads. A driving electrostatic field couples electronic and mechanical degrees of freedom. These systems integrate electronic and mechanical functionality, being able to work e.g. as a sensor, switch, current rectifier, charge pump, and motor. Functionalities like these are fundamental to the development of nanomachinery and nanocircuits^{54,55}.

We showed that the typical amount of charge on the islands, which is regulated by

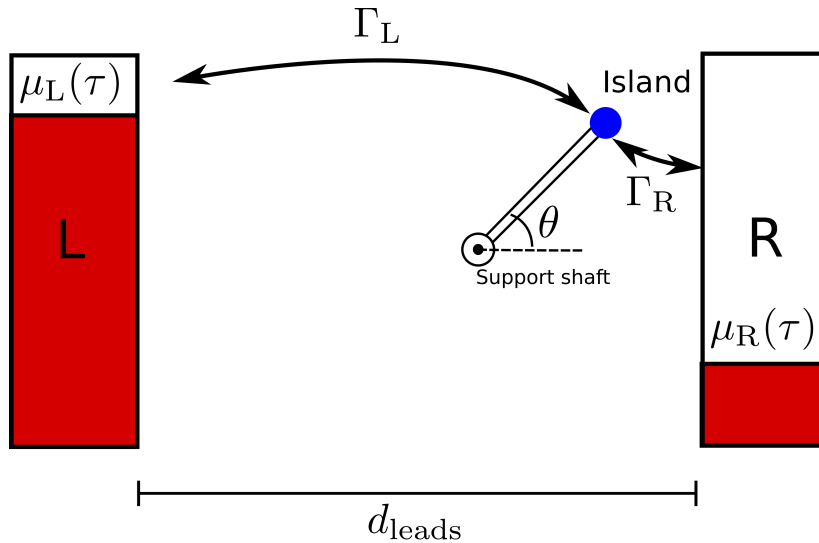


Figure 4.1: Sketch of the current rectifier and its main parts. The rotor is composed of an electronic island connected to a support shaft via insulating rigid arm. A *time-dependent* uniform electrostatic field $\mathbf{E}(\tau)$ permeates the region occupied by the rotor. The leads are biased at *time-dependent* chemical potentials $\mu_{L(R)}(\tau)$. The timescales Γ_L^{-1} and Γ_R^{-1} of tunneling from/to the island to/from respectively the left and the right lead are in general different.

their capacitance, is critical to the rotor’s dynamics (and thereby functionality). The capacitance depends on the size of the islands, and hence it is crucial in a nanoscale device. Generic models of the rotor were already introduced in the literature^{36–38}, but hitherto not linked to the island’s capacitance. We established this link. We proposed experimental realizations of the rotor based on materials and techniques which are available nowadays. Thereby we showed that the rotor can be fabricated with the present-day technology. Finally, we showed that rotational directionality can be achieved, which is important in the context of motors.

In the following, we provide a more detailed account of our achievements.

4.2.1 Summary

Mean-field and stochastic approaches can lead to different dynamics

In the literature one can identify two generic models of this type of rotor^{36–38}, which we refer to as “mean-field” and “stochastic” models in this thesis. In Sec. 3.1 we showcased the dynamics of the mean-field model, and compared them to the dynamics of the stochastic model. The mean-field dynamics had already been analyzed in detail in Ref. [37], but we showed the existence of a new, chaotic-like regime. The transition between this regime and the rotatory regime is characterized by a discontinuous change in the current through the system. Therefore, one can use this regime to realize a switch in the nanoscale.

We showed that the mean-field and stochastic approaches can lead to completely different dynamics, specially for large dissipation (which typically can be easily attained experimentally). For example, the aforementioned discontinuity in the current is not

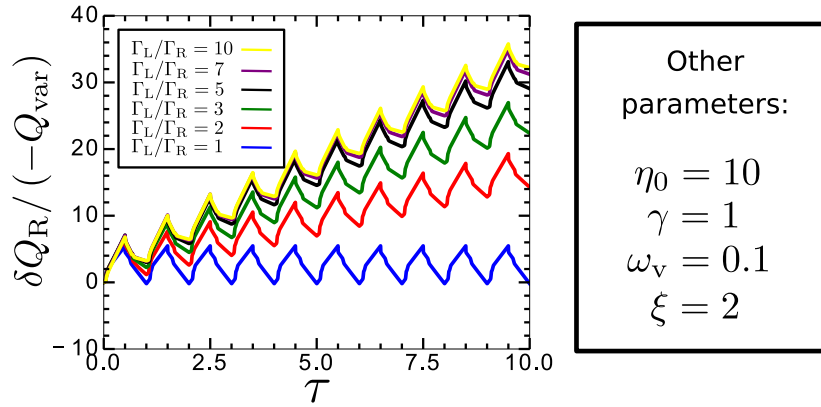


Figure 4.2: Charge accumulated on the right lead δQ_R as a function of time τ for various values of the ratio Γ_L/Γ_R . ω_v is the frequency of the voltage across the leads and of the driving electrostatic field (in phase). Note that no rectification is observed for the symmetric case $\Gamma_L/\Gamma_R = 1$.

observed in the stochastic model. This means that the mean-field and stochastic approaches predict different functionalities for the same set of parameters. Therefore, it is important to know under which conditions one can use which model.

The capacitance of the islands determines the approach to use

In Sec. 3.2 we derived the mean-field and stochastic models from the “orthodox” theory of single electron tunneling⁵⁹. This provides a clear set of conditions under which the models are valid. We showed that the stochastic model is valid in a “single-electron limit”, where the islands are either discharged or charged with a single excess elementary charge (e). This was expected because an analogous model had already been derived for the electron shuttle³⁰. We also showed that the mean-field model is valid in a “continuous-charging limit”, where the typical amount of charge on the islands is much larger than e . Since in this limit the charge fluctuations are negligible compared to the average charge on the islands, deterministic equations of motion were expected. However, the exact form of those equations was unclear before the derivation. The typical amount of charge on the islands is regulated by their capacitance, and hence the capacitance determines which approach is valid. As already mentioned, the capacitance is size-dependent and therefore crucial in a nanoscale device. In this context, an important question is whether one can reach the capacitance values needed to access the aforementioned limits in a real device.

The rotor can be realized with the present-day technology

In Sec. 3.3 we proposed experimental realizations of rotors to be assembled with materials which are extensively studied: gold nanoparticles and multi-walled carbon nanotubes. The bearing^{4,5} and the necessary site-selective attachment of gold nanoparticles on carbon nanotubes^{56,57} were already realized experimentally. The interaction between the charge on the islands and the image charge on the metallic leads poses a hindrance to our experimental realization. The most promising workaround is replacing superconducting

electrodes for the conducting leads.

Our proposals realize rotors in the single-electron and continuous-charging limits. Moreover, they “connect” the two limits. This is possible because the rotor dynamics is essentially confined to two dimensions, which need to be sized in the nanoscale. So one can use the third dimension to extend the islands and consequently increase their capacitances. Indeed, in the continuous-charging limit the device proposed here has two dimensions sized in the nanoscale and one sized in the microscale.

Our findings indicate that it is possible to achieve the dynamics and functionalities showcased in Sec. 3.1 in experiments.

Rotational directionality can be achieved

In the context of nanomotors it is often desirable to have control over the sense of rotation. For some rotors driven by charge tunneling this can be achieved via control over the initial condition. However, charge fluctuations (among other noise sources) and fabrication imperfections can spoil this strategy. A more robust alternative is to introduce a preferred direction of rotation.

In Sec. 3.4 we showed how to achieve rotational directionality via a symmetry-breaking principle working in both the single-electron and continuous-charging limits. To break the symmetry, we need to set an angle $\beta \neq \pi$ between the rotor’s arms and also make $\chi \neq \pi/4$. There are many ways of tuning χ , e.g. impinging electrostatic fields of different magnitudes on the islands A and B or (in the continuous-charging limit) having islands with different maximal charge variations $Q_{\max}^{A(B)}$. We showed that this symmetry-breaking procedure works for large sections of the rotor’s parameter space in both limits. In an experiment, imperfections in the rotor fabrication within the borders of these sections would not spoil the symmetry-breaking.

4.2.2 Outlook

Maybe the most appealing feature of nanoscale rotors driven by charge tunneling is their versatility: the *same* device can function as a sensor, a switch, and a motor. In other words, these rotors concentrate many functionalities which are fundamental to the development of nanomachinery and nanocircuitry^{54,55} in a single device. This is possible because one can access all different dynamical regimes by tuning parameters not fixed by the fabrication of the device (e.g. the driving electrostatic field or the voltage across the leads). We can show that the rotor can also function as a current rectifier, which is one of the fundamental elements of electrical circuits. We use the same strategy as the one employed in Ref. [34] to recast the electron shuttle from Gorelik et al.^{29,30} as a current rectifier. We consider *AC voltage* (and AC driving) between the leads, and (for simplicity) a rotor of a single arm. To break the left/right symmetry and induce a net current to one of the sides, we let the (inverse) timescale of tunneling Γ be lead-dependent: $\Gamma_L \neq \Gamma_R$. This can be achieved e.g. by displacing the rotor towards one of the leads, such that it is not exactly in the middle (as represented in Fig. 4.1). In Fig. 4.2 we plot mean-field results for the total charge transferred to the right lead δQ_R^* as a function of time for some values of the ratio Γ_L/Γ_R . A nonvanishing net

*In units of $-Q_{\text{var}}$, where Q_{var} the maximal charge variation on the island.

current through the system arises for $\Gamma_L \neq \Gamma_R$. We stress that the *mechanical motion is fundamental for the rectification* mechanism described here, as a fixed island does not lead to current rectification.

The simulations presented in this thesis had the purpose of showing principles. For example, we used them to show that obtaining rotational directionality in charge-tunneling-driven rotors is possible, and that chaotic-like dynamics may arise even if charge fluctuations are negligible (continuous-charging limit). When proposing experimental realizations, we showed that it is possible to fabricate a rotor with present-day technology, whose estimated parameters have the same values as those used in our simulations. The next step is to simulate the proposed devices using schemes which account for the specific materials to be used in the fabrication. In particular, this should involve molecular dynamics simulation of the multi-walled carbon nanotube forming the bearing (as in Ref. [3]), and calculation of the electrostatic potential generated by the induced charge distribution on the leads via the Poisson's equation. More sophisticated techniques for the simulation charge transport¹⁶⁸ may also be used. These simulations can show in detail how the rotor should be fabricated in order to reach a desired dynamics/functionality, and thereby motivate experimentalists to pursue this fabrication.

Appendix A

Damping due to light emission

Herewith we consider in detail the coupling between the rotating charges on the islands and the electromagnetic field, item 3) from Sec. 3.3.3.3. Because of this coupling, the rotor emits light, and therefore the ensuing power loss should be in principle taken into account. We will show now that the power radiated by the rotor can be neglected in the timescale of the system dynamics.

We can estimate the emitted power by modeling the singly-charged rotor as a rotating point dipole

$$\mathbf{p} = p_0 (\cos \Omega t \hat{\mathbf{i}} + \sin \Omega t \hat{\mathbf{j}}), \quad (\text{A.1})$$

where $\hat{\mathbf{i}}$ and $\hat{\mathbf{j}}$ are unit vectors (see inset in Fig. 3.2). In Eq. (A.1) p_0 is the magnitude of the dipole and Ω is the angular velocity of the rotation. In the following, we consider the device from Sec. 3.3.1. In the end, we comment on the differences one can find for the device from Sec. 3.3.2. For the estimate of the radiated power, we consider idealized rotations, whose dynamics are depicted in Fig. 3.3 (a) and (b). Within these rotations, the rotor is always singly charged and the dipole moment generated by the rotor's charge distribution at the point \mathbf{r} is

$$\mathbf{p}(\mathbf{r}) = -e (\mathbf{r}_Q - \mathbf{r}), \quad (\text{A.2})$$

where the position of the excess charge $\mathbf{r}_Q = \ell \hat{\mathbf{u}}$. We take then \mathbf{p} as the average value of $\mathbf{p}(\mathbf{r})$ over the rotor:

$$\mathbf{p} = \frac{1}{\ell} \int_{-\ell}^{\ell} d\mathbf{r} \mathbf{p}(\mathbf{r}), \quad (\text{A.3})$$

where the variable r runs over the rotor's length (see Fig. 3.14). We obtain $p_0 = -e\ell$ in Eq. (A.1). The power radiated by a rotating point dipole is

$$P_{\text{rad}} = \frac{\mu p_0^2 \Omega^4}{6\pi c}, \quad (\text{A.4})$$

where μ is the electric permeability of the medium (vacuum in our estimate) and c is the light velocity. We consider an extreme angular velocity: the outer wall of the double-walled nanotube rotates at the critical velocity v_c at which the nanotube collapses³. The angular velocity is then $\Omega = v_c/R_{\text{sh}} = \Omega_c = 8$ rad/ps, where $R_{\text{sh}} = 0.5$ nm is the radius of the support shaft nanotube. Plugging in the the numbers in Eq. (A.4) gives

$$P_{\text{rad}} \approx 5.8 \times 10^{-31} \text{ J/s}, \quad (\text{A.5})$$

while the critical rotational energy is

$$E_{\text{cr}} = \frac{I^2 \Omega_c^2}{2I} = 1.3 \times 10^{-14} \text{ J}, \quad (\text{A.6})$$

where to estimate the rotor's moment of inertia I we have considered a support-shaft nanotube 5 nm long and we have used Ref. [145]. If the rotor is given an initial energy E_{cr} , it will take more than 6 hours to entirely convert this energy into light. For comparison, the period of a single rotation at critical angular velocity is ≈ 0.8 ps!

The device from Sec. 3.3.2 has a larger moment of inertia and a larger absolute value of the charge Q_{var} . While the moment of inertia contributes linearly to the rotational energy E_{cr} , the charge contributes quadratically to the radiated power through p_0 . If we consider a factor 10^3 in I (for extending the nanotube's length into the micrometer scale) and $Q_{\text{var}} = 10^3 e$ (to keep η_0), our former estimate of 6 hours gets smaller by a factor 10^3 , i.e. ≈ 20 s. Still, this is very long compared to both the critical angular velocity and the timescale of item 1) from Sec. 3.3.3.3 (nanosecond).

Appendix B

Mean-field charge dynamics for the case with the gate electrode

We rewrite the tunneling rates from Eqs. (3.53)-(3.54) (now using the free energies for the case with the gate electrode, Eqs. (3.43) and (3.44)) using the dimensionless charges

$$\tilde{Q}_{A(B)} = \frac{Q_{A(B)}}{\Delta V_{LR} C}, \quad (\text{B.1})$$

$$\Delta \tilde{Q} = \frac{e}{\Delta V_{LR} C}, \quad (\text{B.2})$$

where here $C = C_R + C_L + C_g$, obtaining

$$W_L^\pm(n_{A(B)}, \theta_{A(B)}) = - \left(\frac{1}{\Delta \tilde{Q}} \right) \frac{\frac{\Delta \tilde{Q}}{2} \pm \left(-\tilde{Q}_{A(B)} - \frac{C_R + C_g}{C} - \frac{V_g C_g}{\Delta V_{LR} C} \right)}{C R_L(\theta_{A(B)}) \left[1 - \exp \left\{ \beta_{CB} \mp \alpha \left[\tilde{Q}_{A(B)} + \frac{C_R + C_g}{C} + \frac{C_g V_g}{\Delta V_{LR} C} \right] \right\} \right]}, \quad (\text{B.3})$$

$$W_R^\pm(n_{A(B)}, \theta_{A(B)}) = - \left(\frac{1}{\Delta \tilde{Q}} \right) \frac{\frac{\Delta \tilde{Q}}{2} \pm \left(\tilde{Q}_{A(B)} - \frac{C_L + C_g}{C} + \frac{V_g C_g}{\Delta V_{LR} C} \right)}{C R_R(\theta_{A(B)}) \left[1 - \exp \left\{ \beta_{CB} \pm \alpha \left[\tilde{Q}_{A(B)} - \frac{C_L + C_g}{C} + \frac{V_g C_g}{\Delta V_{LR} C} \right] \right\} \right]}, \quad (\text{B.4})$$

where we have not considered any degeneracy. If all degeneracies $s_{L(R)}^\pm$ are the same, Eqs. (B.3) and (B.4) are just renormalized and all the following discussion/derivation is still valid. The dependence on the temperature is summarized by the parameters

$$\alpha = \frac{\Delta V_{LR} e}{k_B T}, \quad (\text{B.5})$$

$$\beta_{CB} = \frac{e^2}{C k_B T}. \quad (\text{B.6})$$

The parameters α and β_{CB} represent two different energy scales normalized by the thermal fluctuations, respectively the power-source and single-electron charging energy scales. We denote the probability density of the island A (B) being charged with $\tilde{Q}_{A(B)}$ at the time t by $\tilde{p}(\tilde{Q}_{A(B)}, t)$, and we define new tunneling rates and injection/ejection rates, respectively $\tilde{w}_{L(R)}^\pm(\tilde{Q}_{A(B)}, \theta_{A(B)})$ and $\tilde{w}_{in/out}(\tilde{Q}_{A(B)}, \theta_{A(B)})$, by

$$\tilde{w}_L^\pm(\tilde{Q}_{A(B)}, \theta_{A(B)}) = \Delta \tilde{Q} W_L^\pm(n_{A(B)}, \theta_{A(B)}), \quad (\text{B.7})$$

$$\tilde{w}_R^\pm(\tilde{Q}_{A(B)}, \theta_{A(B)}) = \Delta \tilde{Q} W_R^\pm(n_{A(B)}, \theta_{A(B)}), \quad (\text{B.8})$$

$$\tilde{w}_{in}(\tilde{Q}_{A(B)}, \theta_{A(B)}) = \Delta \tilde{Q} W_{in}(n_{A(B)}, \theta_{A(B)}), \quad (\text{B.9})$$

$$\tilde{w}_{out}(\tilde{Q}_{A(B)}, \theta_{A(B)}) = \Delta \tilde{Q} W_{out}(n_{A(B)}, \theta_{A(B)}) \quad (\text{B.10})$$

(note that injection and ejection rates for a continuous spectrum on the island were defined before in Eqs. (3.55) and (3.56)). If we “freeze” the mechanical degree of freedom, these rates define the following master equation for the probability density:

$$\begin{aligned} \frac{d}{dt} \tilde{p}(\tilde{Q}_{A(B)}, t) \Delta \tilde{Q} = & \tilde{w}_{\text{out}}(\tilde{Q}_{A(B)} - \Delta \tilde{Q}, \theta_{A(B)}) \tilde{p}(\tilde{Q}_{A(B)} - \Delta \tilde{Q}, t) + \\ & \tilde{w}_{\text{in}}(\tilde{Q}_{A(B)} + \Delta \tilde{Q}, \theta_{A(B)}) \tilde{p}(\tilde{Q}_{A(B)} + \Delta \tilde{Q}, t) - \\ & [\tilde{w}_{\text{out}}(\tilde{Q}_{A(B)}, \theta_{A(B)}) + \tilde{w}_{\text{in}}(\tilde{Q}_{A(B)}, \theta_{A(B)})] \tilde{p}(\tilde{Q}_{A(B)}, t). \end{aligned} \quad (\text{B.11})$$

In the limit $\Delta \tilde{Q} \rightarrow 0$, Eq. (B.11) is equivalent to the Fokker-Planck equation (angle entering as a parameter)

$$\frac{d}{dt} \tilde{p}(\tilde{Q}_{A(B)}, t) = \frac{\partial}{\partial \tilde{Q}_{A(B)}} \left\{ \tilde{p}(\tilde{Q}_{A(B)}, t) [\tilde{w}_{\text{in}}(\tilde{Q}_{A(B)}, \theta_{A(B)}) - \tilde{w}_{\text{out}}(\tilde{Q}_{A(B)}, \theta_{A(B)})] \right\}. \quad (\text{B.12})$$

This Fokker-Planck equation has no fluctuation term, and therefore it is completely equivalent to a deterministic equation for the time variation of the charge¹²²

$$\frac{d}{dt} \tilde{Q}_{A(B)}(t) = -\tilde{w}_{\text{in}}(\tilde{Q}_{A(B)}, \theta_{A(B)}) + \tilde{w}_{\text{out}}(\tilde{Q}_{A(B)}, \theta_{A(B)}). \quad (\text{B.13})$$

One can write Eq. (B.13) explicitly as

$$\begin{aligned} \frac{d}{dt} \tilde{Q}_{A(B)}(t) = & - \frac{\tilde{Q}_{A(B)} - \frac{C_L + C_g}{C} + \frac{V_g C_g}{\Delta V_{LR} C}}{C R_R(\theta_{A(B)})} \frac{1 - \zeta \cosh \left\{ \alpha \left[\tilde{Q}_{A(B)} - \frac{C_L + C_g}{C} + \frac{V_g C_g}{\Delta V_{LR} C} \right] \right\}}{\frac{1 + \zeta^2}{2} - \zeta \cosh \left\{ \alpha \left[\tilde{Q}_{A(B)} - \frac{C_L + C_g}{C} + \frac{V_g C_g}{\Delta V_{LR} C} \right] \right\}} \\ & - \frac{\tilde{Q}_{A(B)} + \frac{C_R + C_g}{C} + \frac{V_g C_g}{\Delta V_{LR} C}}{C R_L(\theta_{A(B)})} \frac{1 - \zeta \cosh \left\{ \alpha \left[\tilde{Q}_{A(B)} + \frac{C_R + C_g}{C} + \frac{C_g V_g}{\Delta V_{LR} C} \right] \right\}}{\frac{1 + \zeta^2}{2} - \zeta \cosh \left\{ \alpha \left[\tilde{Q}_{A(B)} + \frac{C_R + C_g}{C} + \frac{C_g V_g}{\Delta V_{LR} C} \right] \right\}}, \end{aligned} \quad (\text{B.14})$$

where $\zeta = e^{\beta C_B}$ and we note that all terms proportional to $\Delta \tilde{Q}$ vanish in the limit $\Delta \tilde{Q} \rightarrow 0$. It will be convenient to define the shifted (and normalized) electronic population on the islands

$$\tilde{P}_{A(B)} = - \left(\tilde{Q}_{A(B)} - \frac{C_L + C_g}{C} + \frac{V_g C_g}{\Delta V_{LR} C} \right) \frac{C}{C + C_g}. \quad (\text{B.15})$$

With this definition, one can rewrite Eq. (B.14) as

$$\begin{aligned} \frac{d}{dt} \tilde{P}_{A(B)}(t) = & (1 - \tilde{P}_{A(B)}(t)) \frac{1 - \zeta \cosh \left[\alpha (1 - \tilde{P}_{A(B)}(t)) \right]}{\frac{1 + \zeta^2}{2} - \zeta \cosh \left[\alpha (1 - \tilde{P}_{A(B)}(t)) \right]} \tilde{w}_L(\theta_{A(B)}) \\ & - \tilde{P}_{A(B)}(t) \frac{1 - \zeta \cosh \left(-\alpha \tilde{P}_{A(B)}(t) \right)}{\frac{1 + \zeta^2}{2} - \zeta \cosh \left(-\alpha \tilde{P}_{A(B)}(t) \right)} \tilde{w}_R(\theta_{A(B)}), \end{aligned} \quad (\text{B.16})$$

where

$$\tilde{w}_{L(R)}(\theta_{A(B)}) = \frac{1}{C R_{L(R)}(\theta_{A(B)})} \frac{C + C_g}{C}. \quad (\text{B.17})$$

From Eqs. (B.15) and (B.16) one sees that the charge $Q_{A(B)}$ on the island can vary between two well-defined values Q_{\min} and Q_{\max} :

$$-\Delta V_{\text{LR}}(C_{\text{R}} + C_{\text{g}}) - V_{\text{g}}C_{\text{g}} < Q_{A(B)} < \Delta V_{\text{LR}}(C_{\text{L}} + C_{\text{g}}) - V_{\text{g}}C_{\text{g}}. \quad (\text{B.18})$$

This sums up to a total variation $Q_{\max} - Q_{\min} = Q_{\text{var}} = \Delta V_{\text{LR}}C + C_{\text{g}}\Delta V_{\text{LR}}$.

Appendix C

Mean-field mechanical dynamics for the case with the gate electrode

In Sec. 3.2.2 we have derived the mechanical equations of motion of the rotor in the case where the angle β between the arms is π . Here we generalize this to arbitrary β . Moreover, we write these equations using dimensionless quantities and we specialize them to the mean-field case where each island has an independent gate electrode.

Following Sec. 3.2.2, we consider the potential energy associated to a single island to be given by

$$U_{A(B)} = E_{\text{tot}}^{A(B)} + \frac{Q_{A(B)} \Delta V_{\text{LR}}}{d_{\text{leads}}} x_{A(B)}, \quad (\text{C.1})$$

where $E_{\text{tot}}^{A(B)}$ is the total energy stored on the island (defined by Eq. (3.32)), $x_{A(B)}$ is the projection of the position vector of island A (B) on the horizontal unit vector $\hat{\mathbf{i}}$ (see Fig. 3.2), and d_{leads} is the distance between the leads. In the following, we neglect any dependence of $E_{\text{tot}}^{A(B)}$ on the angle.

In Eq. (C.1), $x_A = \ell \cos(\theta)$ and $x_B = \ell \cos(\theta + \beta)$, where ℓ is the distance between the centers of mass of the islands and of the support shaft (“rotor arm length”), and θ is the angle between the rotor arm of the island A and the horizontal unit vector $\hat{\mathbf{i}}$. The kinetic energy is

$$K_{\text{rot}} = \frac{L^2}{2I}, \quad (\text{C.2})$$

where L is the angular momentum and I is the moment of inertia of the rotor. These considerations lead to the following classical Hamiltonian:

$$H_{\text{rot}}(\theta, L, P_A, P_B) = K_{\text{rot}} + U_A + U_B = \frac{L^2}{2I} + \ell E (\cos \theta Q_A + \cos(\theta + \beta) Q_B), \quad (\text{C.3})$$

where $E = \Delta V_{\text{LR}}/d_{\text{leads}}$ is the magnitude of the electrostatic field \mathbf{E} . The Hamilton’s equations of motion for the Hamiltonian of Eq. (C.3) are

$$\frac{d}{dt} \theta = \frac{\partial}{\partial L} H_{\text{rot}}(\theta, L, P_A, P_B) = \frac{L}{I}, \quad (\text{C.4})$$

$$\frac{d}{dt} L = -\frac{\partial}{\partial \theta} H_{\text{rot}}(\theta, L, P_A, P_B) = E \ell (\sin \theta Q_A + \sin(\theta + \beta) Q_B). \quad (\text{C.5})$$

The rotor is coupled to environmental degrees of freedom, and this leads to damping and fluctuations in the angular dynamics. There are many possible dissipation channels for our rotor, depending on the physical system that is used to realize it. Again, as in Sec. 3.2.2, we describe the dissipation via a Langevin equation (with the drift term

proportional to the angular momentum),

$$dL = (E\ell (\sin \theta Q_A + \sin (\theta + \beta) Q_B) - \tilde{\gamma}L) dt + \sqrt{2I\tilde{\gamma}k_B T} dw, \quad (\text{C.6})$$

$$\frac{d}{dt}\theta = \frac{L}{I}, \quad (\text{C.7})$$

where w denotes a Wiener process and $\tilde{\gamma}$ is a phenomenological angular-viscosity parameter.

In the following, we consider the limit $T \rightarrow 0$, the dimensionless time

$$\tau = \Gamma t, \quad (\text{C.8})$$

where Γ^{-1} gives the timescale of tunneling, and the dimensionless angular momentum

$$\Lambda = \frac{L}{I\Gamma}. \quad (\text{C.9})$$

This allows us to rewrite the Eqs. (C.6) and (C.7) as

$$\frac{d}{d\tau}\Lambda = \frac{E\ell}{\Gamma^2 I} (\sin \theta Q_A + \sin (\theta + \beta) Q_B) - \gamma\Lambda. \quad (\text{C.10})$$

Now we focus on the mean-field case. In the Appendix B we have defined the shifted, normalized electronic population on the islands

$$\tilde{P}_{A(B)} = - \left(\tilde{Q}_{A(B)} - \frac{C_L + C_g^{A(B)}}{C_{A(B)}} + \frac{V_g^{A(B)} C_g^{A(B)}}{\Delta V_{LR} C_{A(B)}} \right) \frac{C_{A(B)}}{C_{A(B)} + C_g^{A(B)}}, \quad (\text{C.11})$$

where $C_g^{A(B)}$ and $V_g^{A(B)}$ are respectively the gate capacitance and voltage, and $C_{A(B)}$ is the island's capacitance. Note that Eq. (C.11) generalizes the terms involving the gate ($C_{A(B)}$ also involves the gate capacitance) in Eq. (B.15) to be dependent on the island. The dimensionless charge on the island $\tilde{Q}_{A(B)}$ is defined as

$$\tilde{Q}_{A(B)} = \frac{Q_{A(B)}}{\Delta V_{LR} C_{A(B)}}. \quad (\text{C.12})$$

We can rewrite Eq. (C.10) with the populations defined in Eq. (C.11). Using the island-dependent driving strengths

$$\eta_{A(B)} = \frac{E\ell Q_{\text{var}}^{A(B)}}{\Gamma^2 I}, \quad (\text{C.13})$$

where $Q_{\text{var}}^{A(B)}$ is the absolute value of the maximal charge variation on the island,

$$Q_{\text{var}}^{A(B)} = \Delta V_{LR} (C_{A(B)} + C_g), \quad (\text{C.14})$$

we rewrite Eq. (C.10) as

$$\frac{d}{d\tau}\Lambda = -\eta_A \sin \theta (\tilde{P}_A - G_A) - \eta_B \sin (\theta + \beta) (\tilde{P}_B - G_B) - \gamma\Lambda, \quad (\text{C.15})$$

where

$$G_{A(B)} = \frac{C_L + C_g^{A(B)}}{C_{A(B)} + C_g^{A(B)}} - \frac{V_g^{A(B)} C_g^{A(B)}}{\Delta V_{LR} (C_{A(B)} + C_g^{A(B)})}. \quad (\text{C.16})$$

Note that each gate provides two parameters $C_g^{A(B)}$ and $V_g^{A(B)}$. In the case $\beta \neq \pi$ we can use one of these parameters (in each electrode) to make

$$G_{A(B)} = 0. \quad (\text{C.17})$$

If $\beta = \pi$ and if the gates for the different islands have the same voltage and capacitance, G_A and G_B cancel each other. In both cases we obtain

$$\frac{d}{d\tau} \Lambda = -\eta_A \sin \theta \tilde{P}_A - \eta_B \sin(\theta + \beta) \tilde{P}_B - \gamma \Lambda. \quad (\text{C.18})$$

References

- [1] D. V. Averin and K. K. Likharev; *Journal of Low Temperature Physics* **62** 345 (1986).
- [2] D. Averin and K. Likharev; *Zhurnal Eksperimentalnoi i Teoreticheskoi Fiziki* **90** 733 (1986).
- [3] J. Servantie and P. Gaspard; *Phys. Rev. Lett.* **97** 186106 (2006).
- [4] B. Bourlon, D. C. Glattli, C. Miko, L. Forró and A. Bachtold; *Nano Letters* **4** 709 (2004).
- [5] A. Fennimore, T. Yuzvinsky, W.-Q. Han, M. Fuhrer, J. Cumings and A. Zettl; *Nature* **424** 408 (2003).
- [6] D. Polli, P. Altoè, O. Weingart, K. M. Spillane, C. Manzoni, D. Brida, G. Tomasello, G. Orlandi, P. Kukura, R. A. Mathies *et al.*; *Nature* **467** 440 (2010).
- [7] S. Hahn and G. Stock; *The Journal of Physical Chemistry B* **104** 1146 (2000).
- [8] W. P. Bricker, P. M. Shenai, A. Ghosh, Z. Liu, M. G. M. Enriquez, P. H. Lambrev, H.-S. Tan, C. S. Lo, S. Tretiak, S. Fernandez-Alberti and Y. Zhao; *Scientific reports* **5** 13625 (2015).
- [9] M. Barbatti, A. J. A. Aquino, J. J. Szymczak, D. Nachtigallová, P. Hobza and H. Lischka; *Proceedings of the National Academy of Sciences* **107** 21453 (2010).
- [10] J. Léonard, I. Schapiro, J. Briand, S. Fusi, R. R. Paccani, M. Olivucci and S. Haacke; *Chemistry – A European Journal* **18** 15296 (2012).
- [11] E. M. Miandoab, A. Yousefi-Koma, H. N. Pishkenari and F. Tajaddodianfar; *Communications in Nonlinear Science and Numerical Simulation* **22** 611 (2015).
- [12] A. Gusso, M. G. E. da Luz and L. G. C. Rego; *Phys. Rev. B* **73** 035436 (2006).
- [13] D. V. Scheible, A. Erbe, R. H. Blick and G. Corso; *Applied Physics Letters* **81** 1884 (2002).
- [14] D. R. Koenig, E. M. Weig and J. P. Kotthaus; *Nature Nanotechnology* **3** 482 (2008).
- [15] N. Koumura, R. W. J. Zijlstra, R. A. van Delden, N. Harada and B. L. Feringa; *Nature* **401** 152 (1999).
- [16] T. R. Kelly, H. De Silva and R. A. Silva; *Nature* **401** 150 (1999).

- [17] D. A. Leigh, J. K. Y. Wong, F. Dehez and F. Zerbetto; *Nature* **424** 174 (2003).
- [18] A. M. Fennimore, T. D. Yuzvinsky, W.-Q. Han, M. S. Fuhrer, J. Cumings and A. Zettl; *Nature* **424** 408 (2003).
- [19] R. A. van Delden, M. K. J. ter Wiel, M. M. Pollard, J. Vicario, N. Koumura and B. L. Feringa; *Nature* **437** 1337 (2005).
- [20] U. G. E. Perera, F. Ample, H. Kersell, Y. Zhang, G. Vives, J. Echeverria, M. Grisolia, G. Rapenne, C. Joachim and S.-W. Hla; *Nat. Nanotechnol.* **8** 46 (2013).
- [21] G. S. Kottas, L. I. Clarke, D. Horinek and J. Michl; *Chem. Rev.* **105** 1281 (2005).
- [22] M. Guix, C. C. Mayorga-Martinez and A. Merkoçi; *Chem. Rev.* **114** 6285 (2014).
- [23] C. J. Murphy and E. C. H. Sykes; *Chem. Rec.* **14** 834 (2014).
- [24] P. Mishra, J. P. Hill, S. Vijayaraghavan, W. V. Rossom, S. Yoshizawa, M. Grisolia, J. Echeverria, T. Ono, K. Ariga, T. Nakayama, C. Joachim and T. Uchihashi; *Nano Lett.* **15** 4793 (2015).
- [25] M. Quick, A. L. Dobryakov, M. Gerecke, C. Richter, F. Berndt, I. N. Ioffe, A. A. Granovsky, R. Mahrwald, N. P. Ernsting and S. A. Kovalenko; *The Journal of Physical Chemistry B* **118** 8756 (2014).
- [26] C.-W. Jiang, R.-H. Xie, F.-L. Li and R. E. Allen; *The Journal of Physical Chemistry A* **115** 244 (2011).
- [27] S. Hahn and G. Stock; *Chemical Physics* **259** 297 (2000).
- [28] C. Schnedermann, M. Liebel and P. Kukura; *Journal of the American Chemical Society* **137** 2886 (2015).
- [29] L. Y. Gorelik, A. Isacson, M. V. Voinova, B. Kasemo, R. I. Shekhter and M. Jonson; *Phys. Rev. Lett.* **80** 4526 (1998).
- [30] A. Isacson, L. Gorelik, M. Voinova, B. Kasemo, R. Shekhter and M. Jonson; *Physica B: Condensed Matter* **255** 150 (1998).
- [31] A. Erbe, C. Weiss, W. Zwerger and R. H. Blick; *Phys. Rev. Lett.* **87** 096106 (2001).
- [32] H. Park, J. Park, A. K. Lim, E. H. Anderson, A. P. Alivisatos and P. L. McEuen; *Nature* **407** 57 (2000).
- [33] D. V. Scheible and R. H. Blick; *Applied Physics Letters* **84** 4632 (2004).
- [34] F. Pistolesi and R. Fazio; *Phys. Rev. Lett.* **94** 036806 (2005).
- [35] B. Wang, L. Vuković and P. Král; *Phys. Rev. Lett.* **101** 186808 (2008).

- [36] A. Y. Smirnov, S. Savel'ev, L. G. Mourokh and F. Nori; *Phys. Rev. E* **78** 031921 (2008).
- [37] A. Croy and A. Eisfeld; *EPL (Europhysics Lett.)* **98** 68004 (2012).
- [38] A. Smirnov, L. Murokh, S. Savel'ev and F. Nori; *Bio-mimicking rotary nanomotors*; volume 7364 (2009).
- [39] R. Visschers, M. Chang, F. Van Mourik, P. Parkes-Loach, B. Heller, P. Loach and R. Van Grondelle; *Biochemistry* **30** 5734 (1991).
- [40] W. Kühlbrandt, D. N. Wang and Y. Fujiyoshi; *Nature* **367** 614 (1994).
- [41] N. S. Ginsberg, Y.-C. Cheng and G. R. Fleming; *Accounts of Chemical Research* **42** 1352 (2009).
- [42] F. C. Spano and E. S. Manas; *The Journal of Chemical Physics* **103** 5939 (1995).
- [43] K. K. Niyogi, O. Björkman and A. R. Grossman; *Proceedings of the National Academy of Sciences* **94** 14162 (1997).
- [44] A. V. Ruban, A. J. Young and P. Horton; *Biochemistry* **35** 674 (1996).
- [45] C. T. Middleton, K. de La Harpe, C. Su, Y. K. Law, C. E. Crespo-Hernández and B. Kohler; *Annual Review of Physical Chemistry* **60** 217 (2009).
- [46] A. S. Chatterley, C. W. West, G. M. Roberts, V. G. Stavros and J. R. R. Verlet; *The Journal of Physical Chemistry Letters* **5** 843 (2014).
- [47] C. E. Crespo-Hernández, B. Cohen, P. M. Hare and B. Kohler; *Chemical Reviews* **104** 1977 (2004).
- [48] W. Li, Y. Pan, L. Yao, H. Liu, S. Zhang, C. Wang, F. Shen, P. Lu, B. Yang and Y. Ma; *Advanced Optical Materials* **2** 892 (2014).
- [49] A. Kazaryan, J. C. M. Kistemaker, L. V. Schäfer, W. R. Browne, B. L. Feringa and M. Filatov; *The Journal of Physical Chemistry A* **114** 5058 (2010).
- [50] M. Wewer and F. Stienkemeier; *Phys. Chem. Chem. Phys.* **7** 1171 (2005).
- [51] J. Roden, A. Eisfeld, M. Dvořák, O. Bünermann and F. Stienkemeier; *Journal of Chemical Physics* **134** 054907 (2011).
- [52] O. Birer and E. Yurtsever; *Journal of Molecular Structure* **1097** 29 (2015).
- [53] S. Kirstein and S. Daehne; *International Journal of Photoenergy* page 20363 (2006).
- [54] W. R. Browne and B. L. Feringa; *Nature nanotechnology* **1** 25 (2006).
- [55] N. Engheta; *Science* **317** 1698 (2007).

- [56] H. Chu, Z. Jin, Y. Zhang, W. Zhou, L. Ding and Y. Li; *The Journal of Physical Chemistry C* **112** 13437 (2008).
- [57] H. Chu, L. Wei, R. Cui, J. Wang and Y. Li; *Coordination Chemistry Reviews* **254** 1117 (2010).
- [58] B. Weber, S. Mahapatra, T. F. Watson and M. Y. Simmons; *Nano Letters* **12** 4001 (2012).
- [59] B. L. Altshuler, P. A. Lee and W. R. Webb; *Mesoscopic phenomena in solids*; volume 30; Elsevier (2012).
- [60] J. Simons; *Energetic Principles of Chemical Reactions*; Jones & Bartlett Pub. (1983).
- [61] E. S. Medvedev and V. I. Osherov; *Radiationless Transitions in Polyatomic Molecules*; volume 57 of *Springer Series in Chemical Physics*; Springer-Verlag (1995).
- [62] J. R. Lakowicz; *Principles of fluorescence spectroscopy*; Springer Science & Business Media (2013).
- [63] V. May and O. Kühn; *Charge and energy transfer dynamics in molecular systems*; John Wiley & Sons (2011).
- [64] T. Kobayashi; *J-aggregates*; volume 1; World Scientific (1996).
- [65] O. Kühn and S. Lochbrunner; *Semiconductors and Semimetals* **85** 47 (2011).
- [66] S. K. Saikin, A. Eisfeld, S. Valleau and A. Aspuru-Guzik; *Nanophotonics* **2** 21 (2013).
- [67] S. de Boer, K. J. Vink and D. A. Wiersma; *Chemical Physics Letters* **137** 99 (1987).
- [68] S. D. Boer and D. A. Wiersma; *Chemical Physics Letters* **165** 45 (1990).
- [69] F. C. Spano and S. Mukamel; *The Journal of Chemical Physics* **91** 683 (1989).
- [70] A. J. Musser, M. Liebel, C. Schnedermann, T. Wende, T. B. Kehoe, A. Rao and P. Kukura; *Nature Physics* **11** 352 (2015).
- [71] P. M. Zimmerman, Z. Zhang and C. B. Musgrave; *Nat Chem* **2** 648 (2010).
- [72] D. Fazzi, G. Grancini, M. Maiuri, D. Brida, G. Cerullo and G. Lanzani; *Phys. Chem. Chem. Phys.* **14** 6367 (2012).
- [73] L. Xiao, Z. Chen, B. Qu, J. Luo, S. Kong, Q. Gong and J. Kido; *Advanced Materials* **23** 926 (2011).
- [74] L. Duan, L. Hou, T.-W. Lee, J. Qiao, D. Zhang, G. Dong, L. Wang and Y. Qiu; *J. Mater. Chem.* **20** 6392 (2010).

- [75] A. Witkowski and W. Moffitt; *The Journal of Chemical Physics* **33** 872 (1960).
- [76] R. L. Fulton and M. Gouterman; *The Journal of Chemical Physics* **35** 1059 (1961).
- [77] R. E. Merrifield; *Radiation Research* **20** 154 (1963).
- [78] R. L. Fulton and M. Gouterman; *The Journal of Chemical Physics* **41** 2280 (1964).
- [79] M. Hayashi, Y. J. Shiu, C. H. Chang, K. K. Liang, R. Chang, T. S. Yang, R. Islampour, J. Yu and S. H. Lin; *Journal of the Chinese Chemical Society* **46** 381 (1999).
- [80] W. J. D. Beenken, M. Dahlbom, P. Kjellberg and T. Pullerits; *J. Chem. Phys.* **117** 5810 (2002).
- [81] A. L. Stadler, B. R. Renikuntla, D. Yaron, A. S. Fang and B. A. Armitage; *Langmuir* **27** 1472 (2011).
- [82] J. P. Hill, Y. Xie, M. Akada, Y. Wakayama, L. K. Shrestha, Q. Ji and K. Ariga; *Langmuir* **29** 7291 (2013).
- [83] M. Müller, A. Paulheim, A. Einfeld and M. Sokolowski; *The Journal of Chemical Physics* **139** 044302 (2013).
- [84] T. Sghaier, S. L. Liepvre, C. Fiorini, L. Douillard and F. Charra; *Beilstein Journal of Nanotechnology* **7** 862 (2016).
- [85] A. Celestino and A. Einfeld; *Tuning nonradiative lifetimes via molecular aggregation* (2016); [arXiv:1611.09115](https://arxiv.org/abs/1611.09115).
- [86] W. Domcke, D. R. Yarkony and H. Köppel, editors; *Conical intersections: electronic structure, dynamics & spectroscopy*; World Scientific, Singapore (2004).
- [87] T. A. A. Oliver and G. R. Fleming; *The Journal of Physical Chemistry B* **119** 11428 (2015).
- [88] N. Ismail, L. Blancafort, M. Olivucci, B. Kohler and M. A. Robb; *Journal of the American Chemical Society* **124** 6818 (2002).
- [89] J. Roden, W. T. Strunz, K. B. Whaley and A. Einfeld; *The Journal of Chemical Physics* **137** 204110 (2012).
- [90] S. Mukamel; *Principles of Nonlinear Optical Spectroscopy*; Oxford University Press (1995).
- [91] B. Wolfseder and W. Domcke; *Chemical Physics Letters* **235** 370 (1995).
- [92] D. Egorova, M. F. Gelin, M. Thoss, H. Wang and W. Domcke; *The Journal of Chemical Physics* **129** 214303 (2008).
- [93] A. Ishizaki, T. R. Calhoun, G. S. Schlau-Cohen and G. R. Fleming; *Phys. Chem. Chem. Phys.* **12** 7319 (2010).

- [94] U. Weiss; *Quantum Dissipative Systems*; World Scientific, Singapore (2008).
- [95] A. Eisfeld, L. Braun, W. T. Strunz, J. S. Briggs, J. Beck and V. Engel; *J. Chem. Phys.* **122** 134103 (2005).
- [96] P. Scherer and S. F. Fischer; *Chemical Physics* **86** 269 (1984).
- [97] P. B. Walczak, A. Eisfeld and J. S. Briggs; *J. Chem. Phys.* **128** 044505 (2008).
- [98] H. van Amerongen, L. Valkunas and R. van Grondelle; *Photosynthetic Excitons*; World Scientific, Singapore (2000).
- [99] V. F. Kamalov, I. A. Struganova and K. Yoshihara; *The Journal of Physical Chemistry* **100** 8640 (1996).
- [100] A. Eisfeld, G. Schulz and J. S. Briggs; *Journal of Luminescence* **131** 2555 (2011).
- [101] F. Meinardi, M. Cerminara, A. Sassella, R. Bonifacio and R. Tubino; *Phys. Rev. Lett.* **91** 247401 (2003).
- [102] M. Blencowe; *Physics Reports* **395** 159 (2004).
- [103] M. Poot and H. S. van der Zant; *Physics Reports* **511** 273 (2012).
- [104] M. Kumar and H. Bhaskaran; *Nano Letters* **15** 2562 (2015).
- [105] E. Sage, A. Brenac, T. Alava, R. Morel, C. Dupré, M. S. Hanay, M. L. Roukes, L. Duraffourg, C. Masselon and S. Hentz; *Nature communications* **6** (2015).
- [106] S. Olcum, N. Cermak, S. C. Wasserman, K. S. Christine, H. Atsumi, K. R. Payer, W. Shen, J. Lee, A. M. Belcher, S. N. Bhatia and S. R. Manalis; *Proceedings of the National Academy of Sciences* **111** 1310 (2014).
- [107] B. Lassagne, D. Garcia-Sanchez, A. Aguasca and A. Bachtold; *Nano Letters* **8** 3735 (2008).
- [108] J. Chaste, A. Eichler, J. Moser, G. Ceballos, R. Rurali and A. Bachtold; *Nature nanotechnology* **7** 301 (2012).
- [109] M. Li, H. X. Tang and M. L. Roukes; *Nature nanotechnology* **2** 114 (2007).
- [110] A. D. Smith, F. Niklaus, A. Paussa, S. Vaziri, A. C. Fischer, M. Sterner, F. Forstberg, A. Delin, D. Esseni, P. Palestri, M. Östling and M. C. Lemme; *Nano Letters* **13** 3237 (2013).
- [111] D. Rugar, R. Budakian, H. Mamin and B. Chui; *Nature* **430** 329 (2004).
- [112] T. Kenny; *IEEE Sensors Journal* **1** 148 (2001).
- [113] J. Moser, J. Güttinger, A. Eichler, M. J. Esplandiu, D. Liu, M. Dykman and A. Bachtold; *Nature nanotechnology* **8** 493 (2013).

-
- [114] T. Rocheleau, T. Ndukum, C. Macklin, J. Hertzberg, A. Clerk and K. Schwab; *Nature* **463** 72 (2010).
- [115] A. D. O'Connell, M. Hofheinz, M. Ansmann, R. C. Bialczak, M. Lenander, E. Lucero, M. Neeley, D. Sank, H. Wang, M. Weides *et al.*; *Nature* **464** 697 (2010).
- [116] V. Pott, H. Kam, R. Nathanael, J. Jeon, E. Alon and T. J. K. Liu; *Proceedings of the IEEE* **98** 2076 (2010).
- [117] R. H. Blick, H. Qin, H.-S. Kim and R. Marsland; *New Journal of Physics* **9** 241 (2007).
- [118] T. Nord, L. Y. Gorelik, R. I. Shekhter and M. Jonson; *Phys. Rev. B* **65** 165312 (2002).
- [119] T. Novotný, A. Donarini, C. Flindt and A.-P. Jauho; *Phys. Rev. Lett.* **92** 248302 (2004).
- [120] A. J. Lichtenberg and M. A. Leiberman; *Regular and Chaotic Dynamics*; volume 38 of *Applied Mathematical Sciences*; Springer New York, New York, NY (1992).
- [121] Y.-C. Lai and T. Tél; *Transient Chaos*; volume 173 of *Applied Mathematical Sciences*; Springer New York, New York, NY (2011).
- [122] C. W. Gardiner; *Handbook of stochastic methods*; Springer; 2 edition (1985).
- [123] J.-P. Colinge and C. A. Colinge; *Physics of Semiconductor Devices*; Springer; hardcover edition, 2002 edition (2005).
- [124] T. Dittrich, P. Hänggi, G.-L. Ingold, B. Kramer, G. Schön and W. Zwerger; *Quantum transport and dissipation*; volume 3; Wiley-Vch Weinheim (1998).
- [125] L. Marty, A.-M. Bonnot, A. Bonhomme, A. Iaia, C. Naud, E. André and V. Bouchiat; *Small* **2** 110 (2006).
- [126] M. Raghuvver, A. Kumar, M. Frederick, G. Louie, P. Ganesan and G. Ramanath; *Advanced Materials* **18** 547 (2006).
- [127] N. K. Mehra, V. Mishra and N. Jain; *Biomaterials* **35** 1267 (2014).
- [128] P. G. Collins, M. S. Arnold and P. Avouris; *Science* **292** 706 (2001).
- [129] P. G. Collins, M. Hersam, M. Arnold, R. Martel and P. Avouris; *Phys. Rev. Lett.* **86** 3128 (2001).
- [130] J. Cumings and A. Zettl; *Science* **289** 602 (2000).
- [131] M. S. Tomassone and A. Widom; *Phys. Rev. B* **56** 4938 (1997).
- [132] J. S. Seldenthuis, F. Prins, J. M. Thijssen and H. S. J. van der Zant; *ACS Nano* **4** 6681 (2010).

- [133] S. P. Fletcher, F. Dumur, M. M. Pollard and B. L. Feringa; *Science* **310** 80 (2005).
- [134] X. Zheng, M. E. Mulcahy, D. Horinek, F. Galeotti, T. F. Magnera and J. Michl; *Journal of the American Chemical Society* **126** 4540 (2004).
- [135] H. Zhang, G. Schmid and U. Hartmann; *Nano Letters* **3** 305 (2003).
- [136] U. Simon, G. Schön and G. Schmid; *Angewandte Chemie International Edition in English* **32** 250 (1993).
- [137] S. Chen, R. S. Ingram, M. J. Hostetler, J. J. Pietron, R. W. Murray, T. G. Schaaff, J. T. Houry, M. M. Alvarez and R. L. Whetten; *Science* **280** 2098 (1998).
- [138] J. Schäfer, C. Blumenstein, S. Meyer, M. Wisniewski and R. Claessen; *Phys. Rev. Lett.* **101** 236802 (2008).
- [139] S. Fullam, D. Cottell, H. Rensmo and D. Fitzmaurice; *Advanced Materials* **12** 1430 (2000).
- [140] J. D. Jackson; *American Journal of Physics* **68** 789 (2000).
- [141] C. J. Chen; *Introduction to scanning tunneling microscopy*; volume 4; Oxford University Press on Demand (1993).
- [142] J. Song, K. Mørch, K. Carneiro and A. Thölén; *Surface Science* **296** 299 (1993).
- [143] A. M. Saitta, F. Saija and P. V. Giaquinta; *Phys. Rev. Lett.* **108** 207801 (2012).
- [144] L.-P. Xu and S. Chen; *Chemical Physics Letters* **468** 222 (2009).
- [145] C. Laurent, E. Flahaut and A. Peigney; *Carbon* **48** 2994 (2010).
- [146] T. A. Fulton, P. L. Gammel, D. J. Bishop, L. N. Dunkleberger and G. J. Dolan; *Phys. Rev. Lett.* **63** 1307 (1989).
- [147] A. M. van den Brink, G. Schön and L. J. Geerligs; *Phys. Rev. Lett.* **67** 3030 (1991).
- [148] A. Andreev; *Sov. Phys. JETP* **20** 1490 (1965).
- [149] S. Rajauria, P. Gandit, T. Fournier, F. W. J. Hekking, B. Pannetier and H. Courtois; *Phys. Rev. Lett.* **100** 207002 (2008).
- [150] R. O. Jones, P. J. Jennings and O. Jepsen; *Phys. Rev. B* **29** 6474 (1984).
- [151] P. J. Jennings, R. O. Jones and M. Weinert; *Phys. Rev. B* **37** 6113 (1988).
- [152] D. Averin and A. Korotkov; *Zh. Eksp. Teor. Fiz* **97** 1661 (1990).
- [153] W. R. Browne and B. L. Feringa; *Nat. Nanotechnol.* **1** 25 (2006).
- [154] E. R. Kay, D. A. Leigh and F. Zerbetto; *Angew. Chemie Int. Ed.* **46** 72 (2007).
- [155] K. Kim, J. Guo, X. Xu and D. E. Fan; *ACS Nano* **9** 548 (2015).

- [156] J. Guo, K. Kim, K. W. Lei and D. L. Fan; *Nanoscale* **7** 11363 (2015).
- [157] C. Maggi, F. Saglimbeni, M. Dipalo, F. D. Angelis and R. D. Leonardo; *Nat. Commun.* **6** 1 (2015).
- [158] S. W. D. Bailey, I. Amanatidis and C. J. Lambert; *Phys. Rev. Lett.* **100** 256802 (2008).
- [159] R. Bustos-Marún, G. Refael and F. von Oppen; *Phys. Rev. Lett.* **111** 060802 (2013).
- [160] J.-F. Morin, Y. Shirai and J. M. Tour; *Org. Lett.* **8** 1713 (2006).
- [161] B. Wang, L. Vuković and P. Král; *Phys. Rev. Lett.* **101** 186808 (2008).
- [162] T. Kudernac, N. Ruangsapapichat, M. Parschau, B. Maciá, N. Katsonis, S. R. Harutyunyan, K.-H. Ernst and B. L. Feringa; *Nature* **479** 208 (2011).
- [163] R. Eelkema, M. M. Pollard, J. Vicario, N. Katsonis, B. S. Ramon, C. W. M. Bastiaansen, D. J. Broer and B. L. Feringa; *Nature* **440** 163 (2006).
- [164] J. Wang and B. L. Feringa; *Science* **331** 1429 (2011).
- [165] A. Celestino, A. Croy, M. W. Beims and A. Einfeld; *New Journal of Physics* **18** 063001 (2016).
- [166] Y. Hong, J. W. Y. Lam and B. Z. Tang; *Chem. Commun.* pages 4332–4353 (2009).
- [167] J. Mei, N. L. C. Leung, R. T. K. Kwok, J. W. Y. Lam and B. Z. Tang; *Chemical Reviews* **115** 11718 (2015).
- [168] D. A. Ryndyk, R. Gutiérrez, B. Song and G. Cuniberti; *Green Function Techniques in the Treatment of Quantum Transport at the Molecular Scale*; pages 213–335; Springer Berlin Heidelberg, Berlin, Heidelberg (2009); ISBN 978-3-642-02306-4; doi:10.1007/978-3-642-02306-4_9; URL http://dx.doi.org/10.1007/978-3-642-02306-4_9.

Acknowledgements - Danksagung - Agradecim(i)entos - Благодарственная речь

- Ich danke meinem Doktorvater Prof. Jan-Michael Rost.
- Mein bester Dank geht an A. Eisfeld... Naja, warum ist schon klar!
- Um grande agradecimento vai também a ti, Sr. Beims! Não só pela colaboração, mas também pelo apoio e pelas portas que me abriste.
- Ich danke auch A. Croy für eine gute Kollaboration, seine Hilfe und für das Korrekturlesen.
- Gracias por la colaboración Pablo!
- Danke David, für deine große Hilfe und deine Freundschaft!
- Thank you Chris for the kind revision of some of the material that composes this thesis.
- Danke old sport. Naja, für echt gute Freundschaft.
- Ich danke die Freunde Martin, Andreas, Karsten und die Lehrerin Sandy fürs Deutsch. Naja, sorry wie es geworden ist, ist aber auch eure Schuld!
- Thanks to the friends outside mpipks for the sweet distractions... And yes, I have time now!
- Мариша) Спасибо за лучшие часы вдали от диссертации!
- Meus queridos pais, obrigado! Essa é pra vocês!

Versicherung

Hiermit versichere ich, dass ich die vorliegende Arbeit ohne unzulässige Hilfe Dritter und ohne Benutzung anderer als der angegebenen Hilfsmittel angefertigt habe; die aus fremden Quellen direkt oder indirekt übernommenen Gedanken sind als solche kenntlich gemacht. Die Arbeit wurde bisher weder im Inland noch im Ausland in gleicher oder ähnlicher Form einer anderen Prüfungsbehörde vorgelegt.

Die Arbeit wurde am Max-Planck-Institut für Physik komplexer Systeme in der Abteilung Endliche Systeme angefertigt und von Prof. Dr. Jan-Michael Rost betreut.

Ich erkenne die Promotionsordnung der Fakultät Mathematik und Naturwissenschaften der Technischen Universität Dresden vom 23.02.2011 an.

Datum

Unterschrift